VILNIUS UNIVERSITY

CENTER FOR PHYSICAL SCIENCES AND TECHNOLOGY

Vidas Dobrovolskas

Effects of convection and non-equilibrium radiation transfer in stellar atmospheres

Doctoral Dissertation

Physical sciences, Physics (02 P)

Vilnius, 2013

Doctoral Dissertation was completed during 2008–2013 at Vilnius University.

Scientific supervisor:

dr. Arūnas Kučinskas (Vilnius University, Physical sciences, Physics – 02 P)

VILNIAUS UNIVERSITETAS

FIZINIŲ IR TECHNOLOGIJOS MOKSLŲ CENTRAS

Vidas Dobrovolskas

Konvekcijos ir nepusiausvirosios spinduliuotės pernašos efektai žvaigždžių atmosferose

Daktaro disertacija

Fiziniai mokslai, fizika (02 P)

Vilnius, 2013

Disertacija rengta 2008–2013 metais Vilniaus universitete.

Mokslinis vadovas:

dr. Arūnas Kučinskas (Vilniaus universitetas, fiziniai mokslai, fizika – 02 P)

Abstract

Stellar chemical composition can be deduced from the observed stellar spectra, with the help of theoretical stellar model atmospheres. Model atmospheres describe physical conditions in the stellar atmosphere, thus our knowledge about stellar abundances relies firmly on the accuracy and realism of the physical ingredients that are put into such models. Unfortunately, current commonly used model atmospheres make many simplifications to the real physical picture. For example, it is normally assumed that stellar atmospheres are one-dimensional (either plane-parallel or spherical) and hydrostatic. On the other hand, phenomena related with non-local thermodynamic equilibrium (NLTE) spectral line formation are equally important in real stellar atmospheres and therefore should be properly taken into account when studying abundances of chemical elements. Unfortunately, this is not always the case and thus simplifications are made in this context as well.

In this thesis we investigate the role of convection and non-local thermodynamic equilibrium in the formation of spectral lines taking place in stellar atmospheres. The influence of convection is assessed by analyzing differences in the elemental abundances obtained by using 3D hydrodynamical and classical 1D hydrostatic stellar model atmospheres, for a number of astrophysically important chemical elements and different types of stars. This is done by focusing both on the theoretical aspects of spectral line formation with the 3D hydrodynamical model atmospheres, and by evaluating the size of these effects in the atmospheres of real stars that belong to Galactic globular clusters 47 Tucanae (47 Tuc) and NGC 6752. In a similar fashion, the role of non-local thermodynamic equilibrium effects is investigated by focusing on differences in the elemental abundances derived assuming LTE and NLTE spectral line formation, by using classical 1D model atmospheres. The importance of NLTE effects is assessed by studying chemical composition of Galactic globular cluster stars, located both on the main sequence and red giant branch. Finally, we derive abundances of several important elements in the atmospheres of stars of Galactic globular clusters 47 Tucanae (47 Tuc) and NGC 6752, by taking into account

spectral line formation in 3D and NLTE.

The main results obtained in this work are: (1) the magnitude of the 3D–1D abundance correction (i.e., difference between the abundances inferred from the same spectral line of a given element using 3D hydrodynamical and classical 1D model atmospheres) depends on the excitation potential, and wavelength of a given spectral line, as well as on the metallicity of the model atmosphere. For the red giant stars at solar metallicity ([M/H]= 0.0), the 3D–1D abundance corrections in case of weak lines are in the range of +0.05 to −0.10 dex for neutral atoms and 0.0 to −0.15 dex for singly ionized atoms, whereas at [M/H] = −3 the 3D–1D abundance corrections reach −0.6 dex for neutral atoms and −0.15 dex for ions. For the metall-poor ([M/H] = −2) main sequence stars, the 3D–1D abundance corrections reach −1.1 dex for the spectral lines of neutral atoms. Obviously, such large differences at lower metallicities can not be neglected in the context of stellar abundance work. (2) In the atmospheres of red giant stars, large 3D–1D abundance corrections are caused mainly by the horizontal temperature inhomogeneities arising from the convective motions in stellar atmospheres. Differences in the temperature stratifications between the average 3D and 1D model atmospheres play an important, albeit typically smaller, role. The situation is different in main sequence stars, however: in this case it is the difference between the temperature profiles that provides the largest contribution towards the total 3D–1D abundance correction, especially at lowest metallicities. (3) NLTE effects are very important in the formation of spectral lines of sodium and oxygen in the atmospheres of main sequence turn-off (TO) stars in the Galactic globular cluster 47 Tuc. In this case, the differences between the abundances derived with NLTE and LTE approaches may reach $\Delta_{\mathrm{1D\,NLTE-1D\,LTE}} \approx -0.35$ dex for sodium infrared doublet lines located at 818.3 and 819.5 nm, and $\Delta_{\mathrm{1D\,NLTE-1D\,LTE}} \approx -0.20$ dex for the oxygen infrared triplet at 777 nm. The role of convection in the spectral line formation is significantly less important in the atmospheres of these stars: the differences in the abundances of sodium and oxygen inferred from the same spectral lines with the 3D hydrodynamical and 1D classical model atmospheres are $\Delta_{\mathrm{3D-1D}} \approx +0.02$ dex and $\Delta_{\mathrm{3D-1D}} \approx +0.05$ dex, respectively. (4) We determined abundances of lithium, oxygen, and sodium in

the atmospheres of 110 turn-off stars in the globular cluster 47 Tuc, taking into account both NLTE and 3D effects. The determined abundances span the following ranges (as indicated by the numbers after the plus-minus sign, which give the standard deviation of the respective abundance variation in the entire sample of studied stars): $\langle \log \epsilon(\mathrm{Li}) \rangle = 1.78 \pm 0.18$, $\langle [\mathrm{O/Fe}] \rangle = +0.28 \pm 0.16$, and $\langle [\mathrm{Na/Fe}] \rangle = +0.11 \pm 0.15$. We also determined abundances of lithium, sodium, and barium in the atmospheres of 8 red giant stars in the globular cluster NGC 6752, again taking into account both NLTE and 3D effects: $\langle \log \epsilon(\mathrm{Li}) \rangle = 0.74 \pm 0.23$, $\langle [\mathrm{Na/Fe}] \rangle = +0.03 \pm 0.28$, and $\langle [\mathrm{Ba/Fe}] \rangle = +0.10 \pm 0.06$.

Acknowledgments

I would like to express my gratitude to S. Andrievsky, P. Bonifacio, E. Caffau, S. Korotin, H.-G. Ludwig, T. Mishenina, F. Royer, M. Steffen, V. Tsymbal.

I appreciate numerous interactions and help from V. Vansevičius, J. Sūdžius, J. Sperauskas, S. Bartašiūtė, D. Narbutis, D. Semionov, A. Pučinskas, S. Raudeliūnas, R. Lazauskaitė, G. Valiauga, A. Černiauskas, A. Ivanauskas, J. Klevas, D. Prakapavičius among many people.

I would like to acknowledge Vilnius University and Lithuanian Research Council for financial support providing opportunities to participate in summer schools and conferences.

I am very grateful to my supervisor Arūnas Kučinskas for his help and encouragement.

My special thanks to Ernestas, Inga, and Sandra.

Most of all I am thankfull to my parents and family.

Contents

Introduction

Motivation

Knowledge of chemical composition of stars in different stellar populations provides us with the information about the chemical evolution of the Universe. Determination of stellar chemical composition relies on our interpretation of spectral lines and assumptions about the physical conditions in the models used to interpret the observed data. These assumptions – and amongst them, sets of equations relating different thermodynamical (temperature, pressure, density, etc.) and hydrodynamical (e.g., velocity) quantities and their distribution in space and time – is what defines the properties of a given model atmosphere. Obviously, the realism of physics taken into the account in stellar model atmospheres determines how reliable our knowledge of stellar abundances is.

The first stellar model atmospheres were built on a number of simplifications made to the real physical picture, mainly due to computational reasons: thermodynamic quantities were described as one-dimensional functions of radial distance in the stellar atmosphere (hence their name one-dimensional, or 1D, model atmospheres), neglecting any time dependencies and/or horizontal inhomogeneities. However, even a short glimpse at a sequence of high resolution solar photosphere photographs showing constantly changing patterns of granules and sunspots would provide a clear indication that outer layers of stellar atmospheres are far from being static and homogeneous. Convection being the crucial energy transport mode in the outer layers of solar type stars creates, for example, horizontal temperature inhomogeneities, shock waves, and is intrinsically variable in time.

One should also note that convection is a non-local process, in a sense that physical properties and velocity profile of the convective flow are determined not only by its immediate surroundings but also by the physical conditions in more remote (e.g., deeper) atmospheric layers. Nevertheless, one of the most widely used physical descriptions of convection in the classical 1D model atmospheres – the mixing-length theory – treats convection

as a strictly local process. It is not surprising then that already the earliest attempts to model convection with the 3D hydrodynamical model atmospheres produced average temperature stratifications that were very different from those predicted by the 1D models utilizing mixing-length theory (see, e.g., Nordlund 1982).

Any spectral line formed in convective stellar atmosphere is expected to be asymmetric and blue-shifted, due to larger contribution from the rising hot convective cells. High resolution spectral observations of the Sun and other stars show that spectral lines are indeed asymmetric and blue shifted (Gray 2005, 2012; Gray et al. 2008). While classic 1D stellar atmosphere models are unable to predict asymmetric spectral line profiles, hydrodynamic 3D model atmospheres naturally produce spectral line asymmetries, in accord with observations. For example, Ramírez et al. (2010) and Klevas et al. (2013) successfully reproduced spectral line bisectors in the observed spectrum of a bright metal-poor red giant HD 122563, with more such studies currently in progress.

One of very important observational tests to verify the predictions of stellar model atmospheres is their capability to correctly reproduce limb darkening observed in real stars. Limb darkening is a property common to any star: looking away from the center of a stellar disk (i.e., at higher inclination angles) the observer would see radiation from higher and cooler atmospheric stellar layers, which would result in a reduction of radiation intensity. In this way, stellar limb darkening is a sensitive probe of the temperature gradients in stellar atmospheres. The most comprehensive observations of the limb darkening law are currently available for the Sun but interferometers are already providing similar observations for other stars. For example, Asplund (2009) shows that 3D hydrodynamic models predict solar limb darkening in very good agreement with the observations. Hayek et al. (2012) investigated two late-type dwarfs and concluded that limb darkening law predicted by the 3D hydrodynamical model atmospheres provided much better fit to the observations compared to the predictions of classical 1D model atmospheres.

Very importantly, numerous recent studies point towards significant differences that must be expected between the stellar abundances derived us-

ing 3D hydrodynamical and classical 1D model atmospheres (Collet et al. (2007, 2009); González Hernández et al. (2009); Ramírez et al. (2009); Behara et al. (2010); Kučinskas et al. (2013); Dobrovolskas et al. (2013); see also Asplund (2005) for a review of earlier work). These differences become larger at lower metallicities and at their extremes may reach 1 dex (!).

A detailed early investigation of the interplay of convection and spectral line formation, as well as of the resulting implications on stellar abundance derivations, was performed by Collet et al. (2007) who showed that differences in the abundances predicted by the 3D and 1D model atmospheres of red giant stars may reach −1 dex, with the largest discrepancies seen at lowest metallicities ([M/H] [1] = −3.0). 3D hydrodynamical models predict lower temperatures in the outer layers of stellar atmospheres where lines of molecules and neutral atoms form, therefore these chemical species must be particularly sensitive to convection effects (Asplund 2005; Collet et al. 2007; Kučinskas et al. 2013; Dobrovolskas et al. 2013).

It is clear that the adoption of 3D stellar atmosphere models in the stellar abundance analysis work is crucial. This may be especially important for studies of stellar populations at lowest metallicities (i.e., the oldest populations) – such as Galactic halo stars and Galactic globular cluster (GGC) stars. For these objects, differences in the abundances predicted with the 3D hydrodynamical and classical 1D model atmospheres are largest, which may potentially have important implications to the understanding of early nucleosynthesis in our Galaxy and beyond.

3D hydrodynamical effects aside, many of the abundance studies so far have been made assuming local thermodynamic equilibrium (LTE) in the spectral line synthesis calculations. Non-equilibrium effects in the radiation transfer, however, may become especially important at low metallicity, owing to the lower opacities (e.g., overionization by the UV photons; see, e.g., Asplund 2005; Mashonkina et al. 2011, for more details). Deviations from the LTE also occur because of the lower electron number density in the stellar atmospheres at lower metallicities, which may make the electron collisions with atoms and ions less efficient and, in turn, may lead to further departures from LTE. Since the oldest Galactic populations have

[1] $[M/H] = \log[N(M)/N(H)]_{\star} - \log[N(M)/N(H)]_{\odot}$.

metallicities that are significantly lower than solar it is clearly desirable to use NLTE approach for the determination of elemental abundances in their atmospheres.

It would be thus timely to re-analyze in a systematical and homogeneous way the abundances of various chemical elements in the Galactic globular clusters, employing for this purpose state-of-the-art 3D hydrodynamical atmosphere models together with NLTE analysis techniques, and to assess the importance of convection and non-equilibrium radiation transfer on the spectral line formation and subsequent abundance determinations.

In this Thesis we performed a theoretical investigation of the impact of convection on the spectral line formation in LTE, by analyzing differences in the abundances of chemical elements predicted with the 3D hydrodynamical and classical 1D model atmospheres of the main sequence turn-off (TO) and red giant branch (RGB) stars. We also applied 3D hydrodynamical model atmospheres and 1D NLTE spectral line synthesis to study the abundances of light (lithium, oxygen, sodium) and heavy (barium) chemical elements in the atmospheres of stars that belong to two Galactic globular clusters: NGC 6752 (a representative halo globular cluster) and 47 Tuc (NGC 104, representative bulge globular cluster).

Novelty

Research done in this Thesis is new in several key aspects which are listed below:

1. Systematical theoretical investigation of the role of convection in the formation of spectral lines taking place in the atmospheres of stars from the main sequence turn-off point to the red giant branch tip was performed for the first time. In this context, we studied so far the largest sample of chemical elements and their (fictitious) spectral lines characterized by different excitation potentials and wavelengths, at different metallicities.

2. At lowest metallicities, the influence of convection on the spectral line formation in the atmospheres of red giant branch stars occurs mostly via horizontal temperature fluctuations, while in the main sequence

stars the difference between the temperature profiles in the average 3D and 1D model atmospheres may become an equally important (and sometimes even dominant) contributor.

3. We demonstrate that differences in the spectral line strengths predicted by the 3D hydrodynamical and classical 1D model atmospheres may depend strongly on the line excitation potential and wavelength. At the same time, we show that at any given metallicity the size of these differences may vary dramatically from one chemical element to another.

4. 3D+NLTE abundances of Li, O, Na, and Ba (i.e., 1D NLTE abundances corrected for the 3D hydrodynamical effects) were determined for the first time in the atmospheres of main sequence turn-off point and red giant branch stars belonging to the Galactic globular clusters 47 Tuc and NGC 6752. The number of investigated stars (110 in 47 Tuc, and 8 in NGC 6752) makes these stellar samples the largest to date investigated in the Galactic globular clusters with the aid of 3D hydrodynamical stellar model atmospheres.

5. We find that in case of O, Na, and Ba lines the differences in the line strengths predicted with the 3D hydrodynamical and 1D hydrostatic model atmospheres for the main sequence turn-off point and red giant branch stars in 47 Tuc and NGC 6752 are small and do not exceed ~ 0.1 dex. They are typically significantly smaller than the 1D NLTE–LTE abundance corrections which, for example, in the atmospheres of main sequence turn-off point stars in 47 Tuc may reach -0.20 dex and -0.35 dex in the case of O and Na, respectively.

Aim of the study

Investigate the nature of convection and non-local thermodynamic equilibrium effects in spectral line formation in the atmospheres of main sequence and red giant branch stars.

Main tasks

1. Study the influence of convection on the formation of spectral lines of different chemical elements in the atmospheres of different metallicity main sequence turn-off (TO) and red giant branch (RGB) stars, by using for this purpose 3D hydrodynamical model atmospheres.

2. Evaluate the importance of 3D and NLTE effects in the spectral line formation, and determine the abundances of key light and heavy chemical elements in the atmospheres of TO and RGB stars in Galactic globular clusters 47 Tuc and NGC 6752.

Results and statements to defend

1. The influence of convection on the formation of spectral lines of Si I, Ti I, Fe I, and Ni I in LTE is largest at lowest metallicities, both in the atmospheres of main sequence (TO) and red giant branch (RGB) stars: the 3D–1D LTE abundance corrections for the lowest-excitation lines (< 2 eV) of Fe I and Ni I reach -0.7 dex and -0.6 dex at [M/H] $= -3.0$ (RGB stars), respectively, and -1.1 dex for Fe I and Ti I at [M/H] $= -2.0$ (TO stars).

2. NLTE effects are significantly more important than those related to convection in the formation of 777 nm triplet lines of oxygen and 818 and 819 nm lines of sodium in the atmospheres of TO stars in 47 Tuc: the mean 1D NLTE–LTE abundance corrections reach to -0.35 dex and -0.20 dex for 818 nm and 819 nm lines of sodium and 777 nm triplet lines of oxygen, respectively, while the mean 3D–1D LTE abundance corrections are considerably smaller, $+0.02$ dex and $+0.05$ dex, respectively.

3. The 3D + NLTE abundances (i.e., 3D-corrected 1D NLTE abundances) of light elements were determined in the atmospheres of TO stars belonging to the Galactic globular cluster 47 Tuc. The obtained average abundances are: $\langle \log \epsilon(\mathrm{Li}) \rangle = 1.78 \pm 0.18$ (94 objects), $\langle [\mathrm{O/Fe}] \rangle = +0.28 \pm 0.16$, and $\langle [\mathrm{Na/Fe}] \rangle = +0.11 \pm 0.15$ (110 objects in the latter two cases), where numbers following the plus-minus sign give the range of the respective abundance variation in the entire studied stellar sample, as measured by its dispersion.

4. The 3D + NLTE abundances of lithium, sodium, and barium were determined in the atmospheres of 8 RGB stars belonging to the Galactic globular cluster NGC 6752. The obtained average abundances are: $\langle \log \epsilon(\mathrm{Li}) \rangle = 0.74 \pm 0.23$, $\langle [\mathrm{Na/Fe}] \rangle = +0.03 \pm 0.28$, and $\langle [\mathrm{Ba/Fe}] \rangle = +0.10 \pm 0.06$.

Personal contribution

The author performed 1D LTE, 1D NLTE, and 3D LTE spectral synthesis calculations and computed 3D–1D abundance corrections for the following neutral and ionized atomic species: C I, N I, O I, Si I, Si II, Ti I, Ti II, Fe I, Fe II, Ni I, Ni II, Ba II, and Eu II; he contributed to the analysis of spectral line formation properties of these elements in the presence of convection in stellar atmospheres (Chapter 2). The author did the abundance analysis of lithium, oxygen, and sodium based on the GIRAFFE/VLT spectra of 110 TO stars in Galactic globular cluster 47 Tuc, did the 1D LTE, 1D NLTE, and 3D LTE spectral synthesis computations, computed the 3D–1D abundance corrections, studied the role of 3D hydrodynamical and NLTE effects in the formation of spectral lines of Li, O, and Na taking place in the atmospheres of these stars (Chapter 3). The author did the spectroscopic abundance analysis of lithium and sodium in the atmospheres of 20 RGB stars in Galactic globular cluster NGC 6752, made 1D LTE and 3D LTE spectral synthesis computations, computed the 3D–1D abundance corrections, studied the role of 3D hydrodynamical and NLTE effects on the lithium, sodium, and barium spectral line formation taking place in the atmospheres of these stars (Chapter 3).

Publications on the thesis topic in the refereed journals

1. **Dobrovolskas, V.**, Kučinskas, A., Bonifacio, P., Korotin, S. A., Sbordone, L., Caffau, E., Prakapavičius, D., Steffen, M., Ludwig, H.-G., Royer, F. 2013, *Abundances of lithium, oxygen, and sodium in the turn-off stars of Galactic globular cluster 47 Tuc* // Astronomy and Astrophysics, submitted, arXiv:1311.1072.
2. **Dobrovolskas, V.**, Kučinskas, A., Klevas, J., Caffau, E., Ludwig, H.-G., Steffen, M. 2013, *Three-dimensional hydrodynamical CO5BOLD model atmospheres of red giant stars III. Line formation in the atmospheres of giants located close to the base of RGB* // Astronomy and Astrophysics, in press, DOI:10.1051/0004-6361/201321036.
3. Kučinskas, A., Steffen, M., Ludwig, H.-G., **Dobrovolskas, V.**, Ivanauskas, A., Klevas, J., Prakapavičius, D., Caffau, E., Bonifacio, P. 2013, *Three-dimensional hydrodynamical CO5BOLD model atmospheres of red giant stars. II. Spectral line formation in the atmosphere of a giant located near the RGB tip* // Astronomy and Astrophysics, 549, A14.
4. **Dobrovolskas, V.**, Kučinskas, A., Andrievsky, S. M., Korotin, S. A., Mishenina, T. V., Bonifacio, P., Ludwig, H.-G., Caffau, E. 2012, *Barium abundance in red giants of NGC 6752. Non-local thermodynamic equilibrium and three-dimensional effects* // Astronomy and Astrophysics, 540, A128.
5. Mishenina, T. V., Kučinskas, A., Andrievsky, S. M., Korotin, S. A., **Dobrovolskas, V.**, Ivanauskas, A., Caffau, E., Ludwig, H.-G., Steffen, M., Sperauskas, J., Klochkova, V. G., Panchuk, V. E. 2009, *NLTE Abundances of Sodium, Magnesium and Barium in the Globular Clusters M10 and M71* // Baltic Astronomy, 18, 193–203.

Other publications in the refereed journals

1. Kučinskas, A., **Dobrovolskas, V.**, Lazauskaitė, R., Tanabé, T. 2009, *Properties of Red Giant Branches of Star Clusters in the Magellanic Clouds and Their Relation with Cluster Metallicity. II. Mean Photometric Colors of Cluster RGBs* // Baltic Astronomy, 18, 225–232.
2. Kučinskas, A., **Dobrovolskas, V.**, Černiauskas, A., Tanabé, T. 2008, *Properties of Red Giant Branches of Star Clusters in the Magellanic Clouds and Their Relation with Cluster Metallicity* // Baltic Astronomy, 17, 363–372.
3. Kučinskas, A., **Dobrovolskas, V.**, Lazauskaitė, R., Lindegren, L., Tanabé, T. 2008, *Magnitude and Color Transformations Between Sirius and 2MASS Photometric Systems* // Baltic Astronomy, 17, 283–292.

Presentations at the conferences

1. **Dobrovolskas, V.**, Kučinskas, A., Bonifacio, P., Korotin, S. A., Sbordone, L., Caffau, E., Prakapavičius, D., *Abundances of lithium, oxygen and sodium in the turn-off stars of Galactic globular cluster 47 Tuc* // "40th Lithuanian National Physics Conference", Programa ir pranešimų tezės, Vilniaus universitetas, 244 p. Vilnius, 10–12 June, 2013 (poster presentation).
2. Černiauskas, A., Kučinskas, A., Bonifacio, P., Andrievsky, S., Korotin, S., **Dobrovolskas, V.**, *Chemical evolution of light elements in the Galactic globular cluster 47 Tuc* // "40th Lithuanian National Physics Conference", Programa ir pranešimų tezės, Vilniaus universitetas, 226 p. Vilnius, 10–12 June, 2013 (poster presentation).
3. **Dobrovolskas, V.**, Kučinskas, A., Ludwig, H. G., Caffau, E., Klevas, J., Prakapavičius, D., *Chemical abundances in metal-poor giants: limitations imposed by the use of classical 1D stellar atmosphere models* // "11th Symposium on Nuclei in the Cosmos", Proc. of the 11th Symposium on Nuclei in the Cosmos, Published online at `http://pos.sissa.it/cgi-bin/reader/conf.cgi?confid=100`, id.288. (eds. K. Blaum, N. Christlieb, G. Martinez-Pinedo). Heidelberg (Germany), 19–23 July, 2010 (poster presentation).
4. Kučinskas, A., **Dobrovolskas, V.**, Černiauskas, A., Lazauskaitė, R., Tanabé, T., *Metallicities of intermediate-age and old star clusters in the Large Magellanic Cloud* // "Star clusters: basic galactic building blocks throughout time and space", Proc. of the International Astronomical Union, IAU Symposium, 266, 446–446, (eds. R. de Grijs and J. Lepine). Rio de Janeiro (Brasil), 10–14 August, 2009 (poster presentation).
5. Kučinskas, A., **Dobrovolskas, V.**, Ivanauskas, A., Ludwig, H.-G., Caffau, E., Blaževičius, K., Klevas, J., Prakapavičius, D., *Can we trust elemental abundances derived in late-type giants with the classical 1D stellar atmosphere models?* // "Chemical Abundances in the Universe: Connecting First Stars to Planets", Proc. of the International Astronomical Union, IAU Symposium, 265, 209–210, (eds. K. Cunha, M. Spite and B. Barbuy). Rio de Janeiro (Brasil), 10–14 August, 2009 (poster presentation).

Thesis outline

The dissertation consists of **Introduction**, three **Chapters**, **Conclusions**, and **References**.

In **Chapter 1** we describe stellar model atmospheres and spectral line synthesis codes used in this work. We also outline the concept of 3D–1D abundance corrections that are used in the forthcoming chapters to assess the influence of convection on the spectral line formation.

In **Chapter 2** we summarize the results obtained in the investigation of the role of convection in the spectral line formation, and related implications on the abundance determinations in TO and RGB stars. Results on red giant stars presented in this Chapter were published in Dobrovolskas et al. (2013) and Kučinskas et al. (2013) (the second and third papers in the publication list presented in Section "Publications on the thesis topic in the refereed journals" above).

In **Chapter 3** we provide results of the application of 3D hydrodynamical model atmospheres and 1D NLTE spectral line synthesis for the determination of 3D NLTE and/or 3D + NLTE abundances of selected key chemical elements in stars of Galactic globular clusters 47 Tuc and NGC 6752. Results of barium abundance determination in NGC 6752 were published in Dobrovolskas et al. (2012) (the fourth paper in the list of refereed publications). Results on the light element abundances in 47 Tuc are summarized in a paper that is submitted to publication in "Astronomy & Astrophysics". (the first paper in the list of refereed papers).

Chapter 1

Stellar model atmospheres and spectral line synthesis

Inevitably, we have to rely on theoretical models of stellar atmospheres in order to derive chemical composition of real stars from their observed spectra. The accuracy to which the chemical composition of stellar atmospheres can be known is therefore determined by the accuracy of physics that is built into the current stellar model atmospheres.

The most widely used stellar model atmospheres today – classical hydrostatic 1D models – and most sophisticated state-of-the-art model atmospheres available today – 3D hydrodynamical models – differ in this sense significantly. Different assumptions made with the 1D and 3D stellar model atmospheres may lead to very different results when these model atmospheres are used to interpret the observational data. Sometimes, these discrepancies may reveal the importance of various physical assumptions that are built into the models in defining the observable properties of the given model atmosphere. In our study of the influence of convection on the spectral line formation we thus used two types of model atmospheres, 3D hydrodynamical CO^{5}BOLD (Freytag et al. 2012) and classical 1D hydrostatic ATLAS9 (Kurucz 1993) and LHD (Caffau & Ludwig 2007).

After the model atmospheres are computed, radiation transfer problem can be solved to compute a synthetic spectrum corresponding to the given model atmosphere. Such spectrum can be further used to analyze the observed spectrum of a real star, e.g., in order to derive its chemical composition. To do spectral synthesis calculations, in our study we used two spectral synthesis codes: MULTI, which allows to synthesize spectral line profiles of a given chemical element under the assumption of NLTE and by using classical 1D model atmospheres (Carlsson 1986; Korotin et al. 1999); and Linfor3D[1], which solves the radiation transfer problem in 3D under

[1] http://www.aip.de/~mst/linfor3D_main.html

the assumption of LTE.

In this Chapter we describe stellar model atmosphere and spectral line synthesis codes used in this work. We also outline the concept of 3D–1D abundance correction which is used to quantify the impact of convection on the spectral line formation.

1.1 Model atmospheres

In this section we describe stellar model atmospheres used in this work, and outline the assumptions built into these models to account for the effects of convection in stellar atmospheres.

1.1.1 `ATLAS9` model atmosphere code

`ATLAS9`, developed by R. Kurucz (Kurucz 1970), is one of the most widely used classical one-dimensional hydrostatic stellar model atmosphere codes. It assumes plane parallel atmospheric geometry, horizontal homogeneity of all thermodynamic parameters, atmosphere in a static state, and a constant chemical composition throughout the simulated atmosphere. The `ATLAS9` model atmosphere is specified by three parameters – *stellar atmospheric parameters*: effective temperature, $T_{\rm eff}$, logarithm of gravitational acceleration, $\log g$, and iron abundance scaling factor, [Fe/H] (simply called *metallicity*) , which is applied to all chemical species.

The `ATLAS9` stellar model atmosphere is divided into 72 layers in which the mean Rosseland opacity, $\tau_{\rm Ross}$, changes from $\log \tau_{\rm Ross} = -6.875$ at the top to $\log \tau_{\rm Ross} = +2.00$ at the bottom, in steps of $\Delta \log \tau_{\rm Ross} = 0.125$. To compute a new model atmosphere, `ATLAS9` needs to be provided with a trial temperature profile (which can be taken, for example, from the existing model atmosphere grid). Then, temperature in each layer is adjusted iteratively until the total flux, F, which includes radiative and convective components, becomes equal to the flux set by $F = \sigma_0 T_{\rm eff}^4$, where $T_{\rm eff}$ is stellar effective temperature and $\sigma_0 = 5.67 \times 10^{-8}\,{\rm Wm^{-2}K^{-4}}$ is Stefan-Boltzmann constant. Throughout all our computations we assumed that the model has converged when the flux error was $< 1\%$ and the flux derivative was $< 10\%$ in all atmospheric layers.

Convection in `ATLAS9` is described using *mixing-length theory* (MLT;

Böhm-Vitense (1958)) which assumes that convective cell moves a distance l in the atmosphere before releasing its energy budget into and merging with its surroundings. Distance l is specified in the units of pressure scale height, $H_{\rm p}$, via the relation $l = \alpha_{\rm MLT} H_{\rm p}$, where $\alpha_{\rm MLT}$ is a mixing-length parameter. Mixing-length parameter is a free parameter that is calibrated against observations of real stars, by, for example, adjusting it to reproduce the current radius of the Sun. Generally, $\alpha_{\rm MLT}$ lies in the range of $\alpha_{\rm MLT} = 1 \ldots 2$, with higher numbers meaning less efficient convective mixing and shallower temperature profile in the stellar atmosphere. We used $\alpha_{\rm MLT} = 1.25$ in the computations of all `ATLAS9` model atmospheres used in this work. Convectively unstable layers are located rather deep in the stellar atmosphere, typically, at $\log \tau_{\rm Ross} > 1.0$, while the spectral lines usually form in the outer atmosphere ($\log \tau_{\rm Ross} < 0.5$), so the choice of the mixing length parameter normally does not have a noticeable influence on the derived chemical abundances.

In reality, however, convective motions do not abruptly stop at the classical outer Schwarzschild convective boundary and, due to inertia, stellar matter moves into the convectively stable layers resulting in convective overshoot. Convective overshoot in the `ATLAS9` model atmosphere is defined with a free parameter ranging from 0.0 (overshooting OFF) to 1.0 (overshooting ON), and it defines the distance in the units of convective cell radius by which the cell penetrates into convectively stable layers before merging with the surroundings. Although switching this parameter on helps to better reproduce the temperature stratification and limb darkening in the Sun, slightly better results are obtained with convective overshoot switched off in other types of stars, as it was discussed in Castelli et al. (1997). In this work we therefore calculated all `ATLAS9` model atmospheres with convective overshoot switched-off.

Stellar model atmospheres may be computed with the `ATLAS9` code using solar scaled and α-element enhanced chemical composition, with the constant enhancement factor of $+0.4$ dex for all α-elements in the latter case. Unless stated otherwise, in our study we used α-element enhanced composition for all `ATLAS9` model atmospheres at [Fe/H] < -1 (see also Chapter 3).

Opacity in the ATLAS9 models is computed using opacity distribution functions (ODFs), which sample line opacity at 337 wavelength points extending from 8.977 nm to 100 000 nm. In our work we used ODFNEW opacity distribution tables from Castelli & Kurucz (2003).

1.1.2 LHD model atmosphere code

LHD is a classical 1D hydrostatic stellar model atmosphere code which uses plane parallel geometry (Caffau & Ludwig 2007). Similarly to ATLAS9, LHD model atmosphere is defined by its effective temperature, surface gravity, and chemical composition. Mixing length theory in the formulation of Mihalas (1978) is used with the LHD models to calculate convective flux, thus the mixing-length parameter, $\alpha_{\rm MLT}$, is one of the input parameters that needs to be specified beforehand in order to compute any given model atmosphere with the LHD code. The LHD models used in this work were computed with $\alpha_{\rm MLT} = 1$ and $\alpha_{\rm MLT} = 2$. It is important to note that LHD uses the same equation of state and opacity tables as utilized with the CO^{5}BOLD code (see Section 1.1.3). This allows, for example, to make a differential comparison of synthetic spectral lines computed with the CO^{5}BOLD and LHD model atmospheres, and therefore to assess the influence of convection on the spectral line formation (see Chapter 2). We did not make differential comparisons using the ATLAS9 model atmospheres because ATLAS9 models use different opacities and equation of state compared to those utilized with either LHD or CO^{5}BOLD.

1.1.3 3D hydrodynamical model atmosphere code CO^{5}BOLD

Convection is a non-local and multidimensional process which may have a significant impact on the outgoing radiation field and spectral line formation by producing vertical and horizontal inhomogeneities of various thermodynamical and dynamical quantities. Obviously, classical hydrostatic 1D model atmospheres are not able to properly account for such complex 3D hydrodynamical structures. In order to have a better understanding of the interplay between convection and spectral line formation it is necessary to simulate convection explicitly, that is, to solve equations of hydrodynamics and radiation transfer in three-dimensional space and time. This is done in 3D hydrodynamic stellar atmosphere models. The 3D hydro-

dynamical model atmosphere code CO^{5}BOLD (COnservative COde for the COmputation of COmpressible COnvection in a BOx of L Dimensions, L = 2, 3) used in this work solves coupled non-linear equations of compressible hydrodynamics in an external gravity field together with radiation transfer equation. Hydrodynamic part contains equations of mass conservation, energy conservation, and momentum conservation, as follows

$$\frac{\partial \rho}{\partial t} + \frac{\partial}{\partial x}(\rho v_{\mathrm{x}}) + \frac{\partial}{\partial y}(\rho v_{\mathrm{y}}) + \frac{\partial}{\partial z}(\rho v_{\mathrm{z}}) = 0 \tag{1.1}$$

$$\begin{aligned} \frac{\partial(\rho E)}{\partial t} + \frac{\partial}{\partial x}(\rho E + p)v_{\mathrm{x}} + \frac{\partial}{\partial y}(\rho E + p)v_{\mathrm{y}} + \frac{\partial}{\partial z}(\rho E + p)v_{\mathrm{z}} = \\ = \rho(g_{\mathrm{x}}v_{\mathrm{x}} + g_{\mathrm{y}}v_{\mathrm{y}} + g_{\mathrm{z}}v_{\mathrm{z}}) - div\vec{F}_{\mathrm{rad}} \end{aligned} \tag{1.2}$$

$$\begin{cases} \frac{\partial}{\partial t}(\rho v_{\mathrm{x}}) + \frac{\partial}{\partial x}(\rho v_{\mathrm{x}}^2 + p) + \frac{\partial}{\partial y}(\rho v_{\mathrm{x}}v_{\mathrm{y}}) + \frac{\partial}{\partial z}(\rho v_{\mathrm{x}}v_{\mathrm{z}}) = \rho g_{\mathrm{x}} \\ \frac{\partial}{\partial t}(\rho v_{\mathrm{y}}) + \frac{\partial}{\partial x}(\rho v_{\mathrm{y}}v_{\mathrm{x}}) + \frac{\partial}{\partial y}(\rho v_{\mathrm{y}}^2 + p) + \frac{\partial}{\partial z}(\rho v_{\mathrm{y}}v_{\mathrm{z}}) = \rho g_{\mathrm{y}} \\ \frac{\partial}{\partial t}(\rho v_{\mathrm{z}}) + \frac{\partial}{\partial x}(\rho v_{\mathrm{z}}v_{\mathrm{x}}) + \frac{\partial}{\partial y}(\rho v_{\mathrm{z}}v_{\mathrm{y}}) + \frac{\partial}{\partial z}(\rho v_{\mathrm{z}}^2 + p) = \rho g_{\mathrm{z}} \end{cases} \tag{1.3}$$

Magnetic field and stellar rotation were not considered in the simulations done in this work although, in principle, CO^{5}BOLD has an option to include magnetic field in stellar atmosphere modeling. Atmospheric models were computed using "box-in-a-star" setup in which the portion of modeled stellar atmosphere is small compared to the size of a star itself, so that Cartesian geometry could be used. The simulation box had open boundaries (matter was allowed to enter and leave simulation box) in the vertical direction, and periodic boundaries (matter leaving the box is entering from the opposite side) in the horizontal direction. Radiative opacities in our CO^{5}BOLD simulations were computed using opacity binning technique which is described in detail in Nordlund (1982); Ludwig (1992); Ludwig et al. (1994); Vögler et al. (2004). Scattering was treated as true absorption throughout all CO^{5}BOLD simulations.

3D atmospheric structure (i.e., spatial distribution of thermodynamic and hydrodynamic quantities) calculated for a given single instant in time is called a *snapshot*. Generally, full CO^{5}BOLD simulation run of a particular

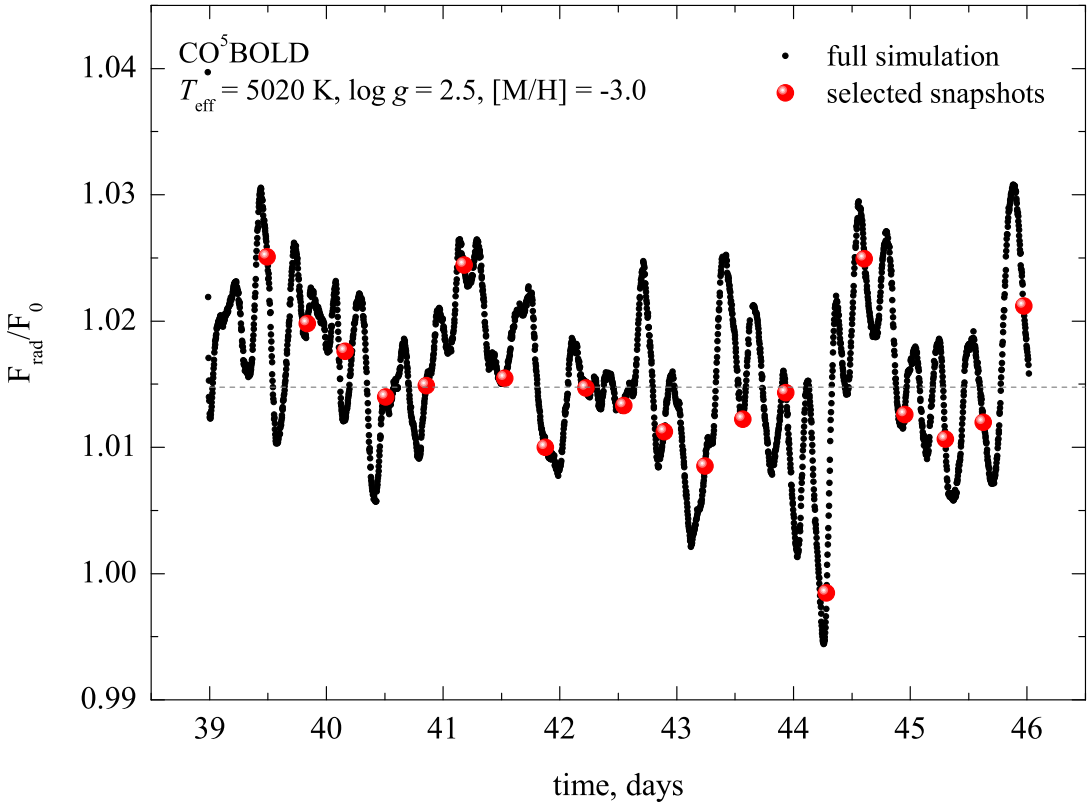

Fig. 1.1. CO5BOLD snapshot selection. Small black solid circles show full temporal sequence of a typical CO5BOLD simulation run and highlight the temporal variation of the radiative flux, $F_{\rm rad}$, normalized to the nominal flux, $F_0 = \sigma T_{\rm eff}^4$. Large full red circles mark the snapshot subsample selected from the full simulation run for the spectral line synthesis computations. Atmospheric parameters of this particular model atmosphere are given in the upper left corner of the figure.

model atmosphere consists of several hundred snapshots. Spectral line synthesis utilizing the 3D hydrodynamical model atmospheres (see sect 1.2.2) is a very time consuming task and thus, to reduce the computational load, usually only a small subsample of snapshots is used in the spectral line synthesis calculations (Fig. 1.1). The selection of snapshots in our work was made by requiring that the average properties (average $T_{\rm eff}$, $T_{\rm eff}$ root-mean-square distribution, velocity field) of this smaller subsample should match as closely as possible those of the full simulation run.

1.2 Spectral synthesis

1.2.1 1D NLTE spectral synthesis code MULTI

In order to solve the radiation transfer problem and compute the spectral line profiles of interest, it is necessary to know the population numbers of atomic levels involved in the given transition. In LTE, population numbers can be computed in a straightforward way by using the Boltzmann-Saha equation. Since in real stellar atmospheres physical conditions in the line forming layers may deviate from the LTE significantly, it is necessary to solve statistical equilibrium equations in order to obtain population numbers for each atomic level throughout the entire line formation region in the stellar atmosphere, i.e., whenever deviations from LTE can be expected. Assuming that the population of atomic levels does not change in time, the condition of statistical equilibrium for a multi-level atom can be written as

$$n_{\mathrm{i}} \sum_{j \neq i}^{n_l} P_{\mathrm{ij}} - \sum_{j \neq i}^{n_l} n_{\mathrm{j}} P_{\mathrm{ji}} = 0 \tag{1.4}$$

here n_{i} and n_{j} are the number density of atoms in the energy levels i and j, respectively, n_{l} is the total number of energy states taken into account, and P_{ij} is the total rate of the atom transition from level i to j. Rate P_{ij} consists of radiative transition rate, R_{ij}, and collisional transition rate, C_{ij}:

$$P_{\mathrm{ij}} = R_{\mathrm{ij}} + C_{\mathrm{ij}} \tag{1.5}$$

Obviously, the total particle number has to be conserved, thus

$$\sum_{j=1}^{n_{\mathrm{l}}} n_{\mathrm{j}} = n_{\mathrm{tot}} \tag{1.6}$$

here n_{tot} is the total number density of atoms under consideration.

The MULTI code, originally developed by Carlsson (1986), performs the spectral line synthesis by solving statistical equilibrium equation together with the radiation transfer equation. Oscillator strengths and ionization cross-sections for a given atom should be provided in the input files of the MULTI code. In this work we have used the version of MULTI modified by

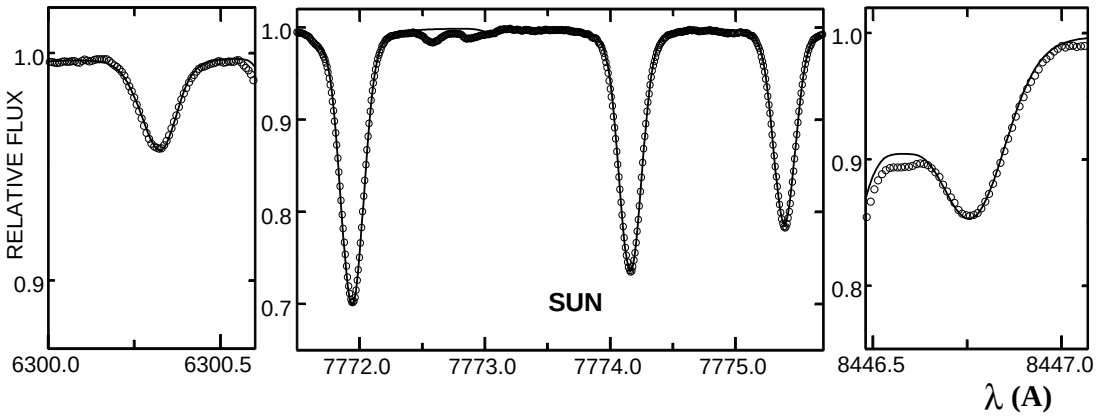

Fig. 1.2. Synthetic spectral lines of oxygen (solid lines) computed with the `MULTI` code and compared with the observed solar spectrum (dots). **Left**: forbidden line at 630.0 nm, **Center**: infrared triplet at 777 nm, **Right**: infrared line at 845 nm. All synthetic spectral line profiles were computed using solar oxygen abundance of $A(\mathrm{O}) = 8.71$.

Korotin et al. (1999) which provides spectral line profiles in the output in addition to the computed line equivalent widths (note that the original version of the `MULTI` code produces only equivalent widths).

1.2.1.1 Model atom of oxygen

The model atom of oxygen used in the NLTE spectral synthesis calculations (Chapter 3) was taken from Dobrovolskas et al. (2013). The model atom of oxygen used in this work consists of 23 energy levels of O I and the ground level of O II Mishenina et al. (2000). Additional 48 energy levels of O I and 15 energy levels of the higher ionization stages were included to account for the particle number conservation. All 46 bound-bound transitions with the wavelengths shorter than 10 000 nm were used in the calculation of atomic level population numbers. Ionization cross-sections were taken from the TOPBASE (Cunto et al. 1993). Rate coefficients for the electronic collisional transitions obtained using detailed quantum mechanical calculations by Barklem (2007) were used for the lowest seven energy levels of O I. Rate coefficients for other allowed transitions were approximated by the classical formula of van Regemorter (1962), while for the forbidden transitions the formula of Allen (1973) was used, with $\Omega = 1$.

Oscillator strengths of the oxygen lines at 630.0 and 636.3 nm were taken from Storey & Zeippen (2000), while for the rest of lines we used data from

NIST. We utilized van der Waals line broadening constants obtained using quantum mechanical calculations (Anstee & O'Mara 1995; Barklem & O'Mara 1997). One should note that at higher metallicities Ni I line located at 630.0 nm becomes an important contributor to the strength of forbidden oxygen line at 630.0 nm. To account for the nickel blend, we used $\log gf = -2.11$ (Johansson et al. 2003) for the Ni I 630.0 nm line and the nickel abundance of $A(\mathrm{Ni}) = 6.17$ (Scott et al. 2009) in the spectral synthesis calculations. Isotopic splitting into two components with $\lambda(^{58}\mathrm{Ni}) = 630.0335$ nm and $\lambda(^{60}\mathrm{Ni}) = 630.0355$ nm (Bensby et al. 2004) was taken into account as well.

Since collisions with the hydrogen atoms play an important role in the atmospheres of cool stars, this effect was taken into account by using the classical formula of Drawin (1969), in the form suggested by Steenbock & Holweger (1984) and with a correction factor $S_{\mathrm{H}} = 1/3$. The numerical value of this coefficient was chosen by comparing predicted and observed oxygen line profiles in the solar spectrum. In particular, by setting $S_{\mathrm{H}} = 0.0$ it was not possible to reconcile the observed strengths of the IR triplet lines at 777.1-5 nm and the line at 844.6 nm, as this line and those belonging to the triplet system would imply different solar oxygen abundance. On the other hand, when the coefficient was set to 1.0 then the IR triplet was too weak and did not produce the same abundance estimate as that obtained from the forbidden oxygen line at 630.0 nm.

To test the model atom, we compared synthetic spectral line profiles with those observed in the spectrum of the Sun. We used Solar model atmosphere from Castelli & Kurucz (2003), together with the chromosphere model VAL-C and the corresponding depth-dependent microturbulence velocity profile from Vernazza et al. (1981). In addition to testing the realism of the model atom, this also allowed us to investigate the possible influence of the chromosphere on the NLTE line formation. Test calculations showed, however, that the latter effect was very small: the difference in the equivalent widths of IR oxygen triplet lines computed using the model atmospheres with and without the chromosphere was less than 1.5%. To compare theoretical lines profiles with those observed in the spectrum of the Sun, re-reduced (Kurucz 2006) Kitt Peak Solar Flux Atlas (Kurucz

et al. 1984) was used (R = 523 000, signal-to-noise ratio S/N = 4000 at the wavelength of infrared sodium lines). In addition, we compared the synthetic line profiles computed for the center of the solar disk with the observed ones taken from the atlas of Delbouille et al. (1973). Synthetic lines were convolved with the Gaussian profile, to obtain spectral resolution of the Kitt Peak Solar Flux Atlas, and broadened by 1.8 $\mathrm{km\,s^{-1}}$ rotational velocity. We assumed $\xi_{\mathrm{micro}} = 1.0$ $\mathrm{km\,s^{-1}}$ microturbulence velocity and $\zeta_{\mathrm{macro}} = 2.0$ $\mathrm{km\,s^{-1}}$ macroturbulence velocity. Solar oxygen abundance derived from the IR triplet lines was $A(\mathrm{O})^2 = 8.71$, which agrees well with $A(\mathrm{O}) = 8.71$ obtained by Scott et al. (2009) and $A(\mathrm{O}) = 8.69$ recommended by Asplund (2009). Comparison of the calculated oxygen line profiles with those observed in the solar spectrum is shown in Fig. 1.2.

1.2.1.2 Model atom of sodium

The model atom of sodium used in the NLTE spectral synthesis calculations (Chapter 3) was taken from Dobrovolskas et al. (2013). The sodium model atom consists of 20 energy levels of Na I and the ground level of Na II (Korotin & Mishenina 1999; Mishenina et al. 2004). Fine splitting has been taken into account only for the 3p level, in order to ensure reliable calculations of the sodium doublet transitions at 589 nm. In total, 46 radiative transitions were taken into account for the level population number calculations. Fixed radiative transition rates were used for other weak transitions. Photoionization rates were taken from the TOPBASE (Cunto et al. 1993).

The sodium model atom accommodates new rate coefficients of collisional excitation and ionization by the hydrogen atoms for the lower 9 levels of Na I, which were obtained by Barklem et al. (2010) using quantum mechanical computations. For other levels, the classical formula of Drawin has been used in the form suggested by Steenbock & Holweger (1984), with the correction factor $S_{\mathrm{H}} = 1/3$.

Electron collision cross-sections from Igenbergs et al. (2008) were used for transitions between the lowest eight energy levels of sodium atom, for a

[2]Abundance A of element X, $A(\mathrm{X},)$ is defined as $A(\mathrm{X}) = \log \epsilon(\mathrm{X}) = \log(N_{\mathrm{X}}/N_{\mathrm{H}}) + 12$, where N_{X} and N_{H} are number densities of element X and hydrogen, respectively.

wide range of impacting electron energies. Electron ionization cross-sections were also taken from Igenbergs et al. (2008). For the rest of the allowed transitions we used the relation of van Regemorter (1962), while for the forbidden transitions the formula of Allen (1973) was utilized.

To test the model atom, we carried out calculations of the spectral line profiles for the Sun. For the Sun, we used re-reduced Kitt Peak Solar Flux Atlas (Kurucz 2006). In case of the Sun, synthetic sodium lines were convolved with the Gaussian profile to obtain the spectral resolution of the Kitt Peak Solar Atlas, and were further rotationally broadened by 1.8 $\mathrm{km\,s^{-1}}$. Microturbulence and macroturbulence velocities were set to $\xi_{\mathrm{micro}} = 1.0\ \mathrm{km\,s^{-1}}$ and $\zeta_{\mathrm{macro}} = 2.0\ \mathrm{km\,s^{-1}}$, respectively. The average solar sodium abundance determined from the nine sodium lines (located at 514.88, 568.26, 568.82, 588.99, 589.59, 615.42, 616.08, 818.33, and 819.48 nm) and using `ATLAS9` model atmosphere was $A(\mathrm{Na})(= \log \epsilon(\mathrm{Na}))$ $= 6.25 \pm 0.08$ dex which agrees well both with the solar photospheric abundance of $A(\mathrm{Na}) = 6.24 \pm 0.04$ dex obtained by Asplund (2009) and with currently recommended solar abundance of $A(\mathrm{Na}) = 6.29 \pm 0.04$ dex from Lodders et al. (2009).

If the model atom is constructed correctly it must describe adequately the spectral lines belonging to different multiplets, yielding identical abundance of a given chemical element irrespective to which line of the multiplet is used. To perform such test, we have chosen lines with different sensitivities to NLTE effects. For example, sodium lines at 818.3 and 819.4 nm are known to be very sensitive to NLTE effects while the widely-used lines at 615.4 and 616.0 nm are not subjected to strong deviations from the LTE. In Fig. 1.3 we show the observed spectrum of the Sun, together with the synthetic spectral line profiles computed under the assumption of NLTE. Clearly, synthetic line profiles fit well the observed lines belonging to different multiplets. For comparison, we also show the LTE line profile of the line located at 818.3 nm which is amongst the most sensitive to NLTE effects. In the case of metal-poor stars, sodium lines at 615.4 and 616.0 nm are too weak to be measured reliably, thus sodium abundance has to be determined using stronger lines.

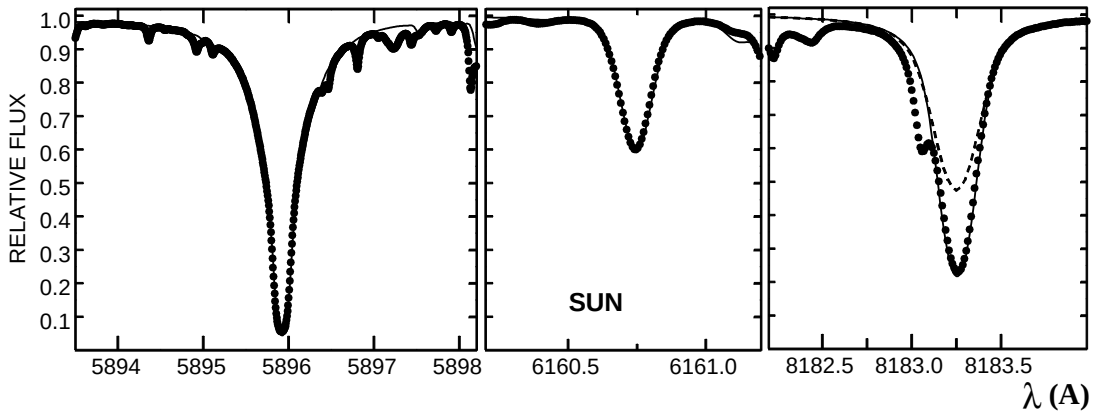

Fig. 1.3. Synthetic 1D NLTE spectral lines of sodium (solid lines) compared with the observed solar spectrum (dots). In case of 818 nm line, which experiences strongest deviations from the LTE, we also show the LTE line profile (dashed line). All synthetic spectral lines were computed using solar sodium abundance of $A(\mathrm{Na}) = 6.25$.

1.2.1.3 Model atom of barium

The model atom of barium used in the NLTE spectral synthesis calculations (Chapter 3) was taken from Andrievsky et al. (2009). It consisted of 31 levels of Ba I, 101 levels of Ba II ($n < 50$), and the ground level of Ba III. In total, 91 bound-bound transitions between the first 28 levels of Ba II were taken into account ($n < 12$, $l < 5$). Fine structure splitting was taken into account for the levels $5\mathrm{d}^2\mathrm{D}$ and $6\mathrm{p}^2\mathrm{P}^0$, according to the prescription given in Andrievsky et al. (2009). We also accounted for the hyperfine splitting of the barium 649.6910 nm line. Isotopic splitting of the barium lines was ignored. Owing to the low ionization potential of neutral barium (~ 5.2 eV), Ba II is the dominant ionization stage in the line-forming regions of investigated stars, with $n(\mathrm{Ba\ I})/n(\mathrm{Ba\ II}) \lesssim 10^{-4}$ throughout the entire atmosphere of the studied RGB stars (see Chapter 3). We therefore assumed that none of the Ba I transitions may noticeably change the level populations of Ba II (cf. Mashonkina et al. 1999). Further details about the barium model atom, assumptions used, and implications involved can be found in Andrievsky et al. (2009) and Korotin et al. (2011).

1.2.2 3D LTE spectral synthesis code Linfor3D

Linfor3D[3] is a spectrum synthesis code which utilizes 3D hydrodynamical model atmosphere (e.g., computed with the CO5BOLD code, see Section 1.1.3), and solves the radiation transfer equation assuming Cartesian geometry and LTE. Radiation transfer equation should be solved over the range of geometrical and optical depths where a non-negligible contribution to the spectral line formation can be expected. Our spectral synthesis computations were therefore performed in the optical depth range extending from $\log \tau_{\rm Ross} = 2.0$ at the inner boundary to $\log \tau_{\rm Ross} = -6.0$ at the outer boundary, with a step of $\Delta \log \tau_{\rm Ross} = 0.08$. Radiation transfer equation was solved along one vertical and two inclined directions, in each case at four azimuthal angles.

For each selected CO5BOLD snapshot, Linfor3D also computes an average 3D model structure, $\langle 3D \rangle$, by averaging thermodynamic quantities (such as temperature, pressure, internal energy, etc.) on surfaces of equal optical depth. Then, spectral line synthesis calculations are performed using the average $\langle 3D \rangle$ model. Since the average $\langle 3D \rangle$ model is a 1D model atmosphere, it may be used to assess the impact of horizontal inhomogeneities of thermodynamical and dynamical properties on the spectral line formation, by comparing the predictions of 3D hydrodynamical and $\langle 3D \rangle$ model atmospheres (see Chapter 2). Linfor3D also reads in a reference 1D model atmosphere structure (in our case computed with the LHD code) for which the spectral line synthesis is done as well, providing a possibility to differentially compare the predictions of full 3D, average $\langle 3D \rangle$, and 1D model atmospheres.

1.3 Assessment of the influence of convection on the spectral line formation: the framework

The influence of convection on the formation of spectral lines in stellar atmospheres was investigated by using curves-of-growth calculated for a given chemical element of interest and further used to compute 3D–1D abundance correction, $\Delta_{\rm 3D-1D}$. The abundance correction is defined as a difference in

[3] http://www.aip.de/~mst/linfor3D_main.html

the abundance obtained from the given spectral line using the 3D hydrodynamical and 1D hydrostatic model atmospheres (see, e.g., Caffau et al. 2011). In reality, theoretical $\Delta_{\rm 3D-1D}$ abundance correction is obtained by measuring the difference between the curves-of-growth calculated with the 3D and 1D model atmospheres, with the measurement made at the equivalent width that corresponds to that of particular spectral line of interest (see Fig. 1.4).

The equivalent width, EW, is defined as:

$$EW = \int_{\lambda_1}^{\lambda_2} \left(\frac{F_{\rm c} - F_\lambda}{F_{\rm c}} \right) d\lambda \tag{1.7}$$

where $F_{\rm c}$ is the continuum flux and F_λ is the flux in the spectral line, with the integration made over the entire width of the line profile. Equivalent width varies slightly from snapshot to snapshot in the 3D hydrodynamical simulation because the overall atmospheric structure varies in time due to convective motions. Therefore, the time-averaged equivalent width is required to compare it with the EW predicted by, e.g., 1D hydrostatic model atmosphere. `Linfor3D` computes the equivalent width for every given snapshot, and the weighted average equivalent width of the snapshot ensemble is then obtained as:

$$\langle EW \rangle = \frac{\frac{1}{N} \sum_i EW_{\rm i} F_{\rm ci}}{\frac{1}{N} \sum_i F_{\rm ci}} \tag{1.8}$$

where N is the number of snapshots, $EW_{\rm i}$ is the equivalent width of i-th snapshot, and $F_{\rm ci}$ is the continuum flux of i-th snapshot in the vicinity of a given spectral line.

The $\Delta_{\rm 3D-1D}$ abundance correction accounts both for the horizontal temperature fluctuations in the 3D hydrodynamical models, *and* different temperature stratifications in the 3D hydrodynamical and classical 1D model atmospheres. One may investigate the impact of these two effects separately, by invoking two additional abundance corrections: $\Delta_{\rm 3D-\langle 3D \rangle} = A({\rm X})_{\rm 3D} - A({\rm X})_{\langle \rm 3D \rangle}$ which would allow to estimate the input to the total abundance correction from the horizontal fluctuations, and $\Delta_{\langle \rm 3D \rangle - 1D} = A({\rm X})_{\langle \rm 3D \rangle} - A({\rm X})_{\rm 1D}$ that would measure the impact from the differences in the

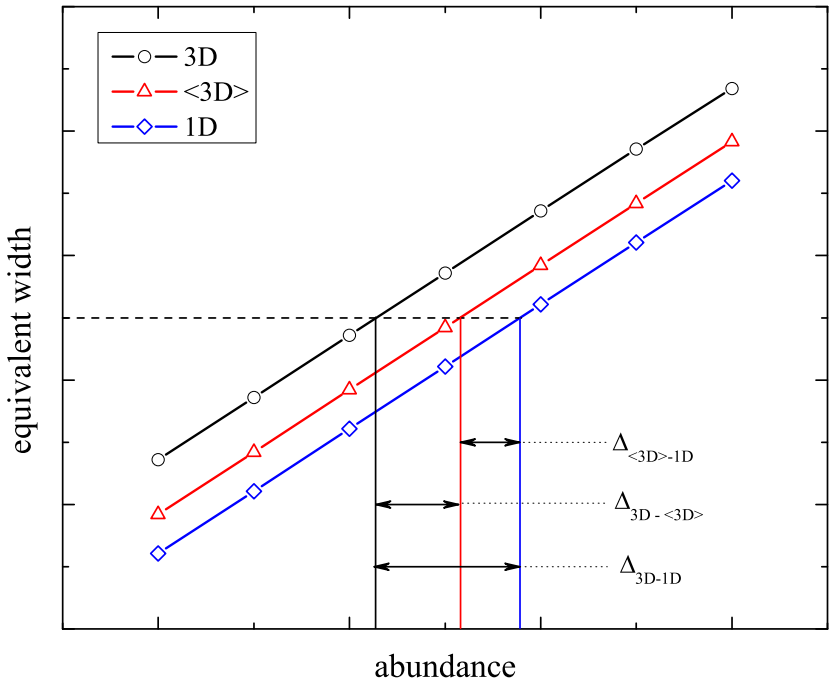

Fig. 1.4. Definitions of the 3D–1D abundance corrections used in this study. Solid lines with open symbols mark the linear part of the curve-of-growth corresponding to the 3D (black circles), average 3D ($\langle$3D$\rangle$, red triangles), and 1D (blue diamonds) model atmospheres, respectively. Abundance corrections are defined as abundance differences between the curves-of-growth corresponding to different model atmospheres and measured at a fixed equivalent width.

temperature stratifications of the average $\langle$3D$\rangle$ and 1D model atmospheres. Full abundance correction could be obviously then the sum of the two corrections, i.e., $\Delta_{\rm 3D-1D} = \Delta_{\rm 3D-\langle 3D\rangle} + \Delta_{\rm \langle 3D\rangle-1D}$ (see Caffau et al. 2011 for more details on various definitions and meanings of abundance corrections).

For computing the abundance corrections, in some cases we used fictitious spectral lines, i.e., lines of a given chemical element or molecule for which the line wavelength, $\lambda_{\rm c}$, excitation potential of the lower level, χ, and equivalent width, EW, were selected arbitrarily (see, e.g., Chapter 2). Such approach allows to investigate the trends of line formation properties over a wide range of spectral line parameters $\lambda_{\rm c}$ and χ, something that is normally impossible when using real spectral lines.

Chapter 2

The influence of convection on the spectral line formation in stellar atmospheres: theoretical aspects

One of the first studies in which 3D hydrodynamical model atmospheres were used to investigate the influence of convection on the spectral line formation was carried out by Collet et al. (2007). The authors studied the interplay between convection and spectral line formation in the atmospheres of red giant stars located close to the bottom of the RGB. While this investigation has revealed that convection may play a very important role in the spectral line formation, subsequent further studies of this type have been nevertheless very scarce so far, despite the many important questions about the interplay of convection and spectral line formation still remaining unanswered.

We therefore attempted to make a more systematic approach to study the role of convection in the spectral line formation taking place in the atmospheres of different types of stars, including those on the main sequence and the red giant branch. This was done by focusing on the abundance corrections, i.e., differences in the abundances inferred from the same spectral line of a given chemical element with the 3D hydrodynamical and classical 1D model atmospheres. For this purpose, we utilized fictitious spectral lines (see Section 1.3) of a number of astrophysically important chemical elements: Li, C, O, Na, Mg, Al, Si, K, Ca, Ti, Fe, Ni, Ba, and Eu. The results obtained in the course of this study are presented in the forthcoming sections of this Chapter; some of them were already published in Kučinskas et al. (2013) and Dobrovolskas et al. (2013).

2.1 Convection and spectral line formation at the tip of the Red Giant Branch

2.1.1 Model atmospheres and spectral line synthesis

To investigate the interplay between convection and spectral line formation, we started by studying the impact of convection on the formation of spectral lines in the atmosphere of cool red giant star, characterized by the following atmospheric parameters: $T_{\rm eff} = 3660\,{\rm K}$, $\log g = 1.0$, and [M/H] = 0.0. This set of atmospheric parameters characterizes a star located near the tip of the Red Giant Branch. Such objects are common in, e.g., stellar populations of the most metall-rich globular clusters (e.g., Pal 10, [Fe/H] = −0.1; BH 176, [Fe/H] = 0.0 Harris 1996). Our goal was to make a differential study, by comparing the predictions of 3D hydrodynamical and classical 1D model atmospheres.

The 3D hydrodynamical model atmosphere used in this investigation was calculated using the CO^{5}BOLD model atmosphere code (Freytag et al. 2012, see also Section 1.1.3). Additionally, we also used classical 1D hydrostatic model atmosphere which was computed using the LHD code (see Section 1.1.2). Both CO^{5}BOLD and LHD model atmospheres were calculated using the same chemical composition, opacities, and equation of state. The same input data used with the 3D and 1D model atmospheres allowed us to make a strictly differential comparison of the spectral line formation, and to avoid any systematics due to differences in the opacities and/or equation of state used with the two model atmospheres. In both cases, we used opacities from the MARCS stellar model atmosphere package (Gustafsson et al. 2008) which were grouped into five opacity bins (see Section 1.1.3). Solar abundances from Grevesse & Sauval (1998) were used in the model atmosphere and spectral synthesis computations, except for carbon, nitrogen, and oxygen, for which the values from Asplund et al. (2005) were used: A(C)=8.41, A(N)=7.8, and A(O)=8.67. All model calculations were made under the assumption of LTE, with scattering treated as true absorption.

Physical dimensions of the red giant model atmosphere simulated with the CO^{5}BOLD code were $15.6 \times 15.6 \times 8.6\,{\rm Gm}^3$ in x, y and z direction respec-

tively, with the numerical resolution of $150 \times 150 \times 151$ grid points. Horizontal span of the model was large enough to cover ~ 10 granules horizontally, which was necessary to ensure good statistical representation of the overall granulation pattern.

After the model has reached a relaxed state, it was run for $\approx$70 days in stellar time corresponding to approximately 7 convective turnover times in the stellar model atmosphere. The full model run consisted of about 3600 snapshots (i.e., individual 3D model structures at different instants in time, see Section 1.1.3), thus carrying out spectral synthesis simulations for the entire model run would have been too computationally demanding. Therefore, for the spectral line synthesis we selected a smaller subsample consisting of 14 snapshots which were spaced by approximately 6 days in stellar time. Snapshot selection was made to ensure that the distribution of statistical properties of the smaller subsample (average effective temperature, its RMS, mean velocity and its RMS, etc.) would match those of the full model run.

In this study we also used average $\langle$3D$\rangle$ models. These model atmospheres were computed by horizontally averaging each 3D atmospheric structure in the subset of fourteen 3D model snapshots selected for the line synthesis calculations. During this procedure, the fourth power of temperature was averaged on surfaces of equal Rosseland optical depth. The fourth power of temperature was chosen over the first because in the former case one may expect to retain better representation of the radiative flux throughout the model atmosphere (note that radiative flux is proportional to T^4 but *not* to T). On the other hand, we found that differences in the elemental abundances obtained using the $\langle$3D$\rangle$ models computed by averaging the fourth and first powers of temperature were always small (for example, in case of Fe I and Fe II lines with $\chi = 0 - 6\,\mathrm{eV}$ these differences were typically much smaller than 0.05 dex). Every $\langle$3D$\rangle$ model is a 1D structure, hence the average $\langle$3D$\rangle$ models do not contain information about the horizontal fluctuations of thermodynamic quantities and velocity fields. Therefore, they can be used to estimate the role of horizontal fluctuations on, e.g., the spectral line formation, which can be done by comparing the predictions of the 3D and $\langle$3D$\rangle$ models.

Synthetic spectral line profiles were computed using the `Linfor3D` spectral synthesis code (see Section 1.2.2), for the following species: N I, O I, Si I, Si II, Ti I, Ti II, Cr I, Cr II, Fe I, Fe II, Ni I, and Ni II. These elements form during different nucleosynthetic cycles and are amongst the most important in stellar abundance work. For example, N and O represent CNO elements, Si and Ti are typical α-elements, while Cr, Fe, and Ni are representatives of the iron group elements. As it was already mentioned in the introduction to this Chapter, in our analysis we used fictitious spectral lines, i.e., lines for which the central wavelength, $\lambda_{\rm c}$, and excitation potential of the lower level, χ, were chosen arbitrarily (see Section 1.3). This method was originally introduced by Steffen & Holweger (2002) and was subsequently used in many studies, including that of Collet et al. (2007). The wavelength range of fictitious spectral lines was chosen to cover that of modern ground-based spectrographs, while the excitation potentials were selected so that they would sample the entire range of χ values typical to real spectral lines. Fictitious spectral lines were therefore computed at $\lambda = 400\,\mathrm{nm}$, $850\,\mathrm{nm}$, and $1600\,\mathrm{nm}$, with the excitation potentials ranging from $\chi = 0$ to $6\,\mathrm{eV}$ for neutral atoms and $\chi = 0$ to $10\,\mathrm{eV}$ for ionized atoms, with a step of $2\,\mathrm{eV}$. The only exceptions were made in the case of oxygen and nitrogen, the real spectral lines of which are characterized by very high excitation potentials and therefore in case of these elements χ covered the range of 0 to $10\,\mathrm{eV}$, just as in the case of ions[1]. The abundance corrections were computed for the weakest lines ($EW < 0.5\,\mathrm{pm}$, normalized to the equivalent width of a given line at $\lambda = 400\,\mathrm{nm}$), in order to minimize the influence of microturbulence velocity on the comparison 1D line profiles.

2.1.2 The influence of convection on the atmospheric structures

One of important consequences of convective motions in stellar atmospheres is the emergence of large horizontal inhomogeneities (fluctuations) of dy-

[1]We note that 850 and 1600 nm also mark the wavelengths of the maximum and minimum bound-free absorption of H^- ion, which is the most important contributor to the continuum opacity in red giant atmospheres at the optical to near-infrared wavelengths. On the other hand, the continuum opacity at 400 nm is dominated by the contribution from metals. The choice of the three wavelengths therefore allows to study the interplay between the different sources of continuum opacity and line formation.

namical and thermodynamic quantities (Fig. 2.1). Since temperature is one of the most important parameters controlling spectral line formation, differences in the temperature stratifications should lead to different strengths of the same line in the predictions of 3D, average ⟨3D⟩, and 1D model atmospheres. In the cool red giant studied here, however, differences between the temperature profiles of the average ⟨3D⟩ and 1D models are small ($\Delta T < 200$ K) in the line forming layers ($\log \tau_{\rm Ross} < 1.0$) which leads to only minor differences in the line strengths (and thus, the elemental abundances) predicted by the ⟨3D⟩ and 1D models.

However, the influence of horizontal temperature inhomogeneities may have a significant impact on the spectral line formation. The amplitude of temperature deviation from the average ⟨3D⟩ profile may be defined as

$$\Delta T_{\rm RMS} = \sqrt{\langle (T - T_0)^2 \rangle_{x,y,t}} \tag{2.1}$$

where $\langle \ldots \rangle_{x,y,t}$ denotes temporal and horizontal averaging on surfaces of equal optical depth, and $T_0 = \langle T \rangle_{x,y,t}$, is depth-dependent average temperature.

As it may be seen from Fig. 2.1, $\Delta T_{\rm RMS}$ gradually decreases from 500 K at $\log \tau_{\rm Ross} = 1.0$ (inner boundary of the highest excitation spectral line formation) to 50 K at $\log \tau_{\rm Ross} = -5.0$ (outer boundary of the lowest excitation spectral line formation). Therefore, the largest differences in the line strength should be expected for lines that form in the deeper atmospheric layers (i.e., lines characterized with the highest χ).

It is also important to note that there are significant differences in the number densities of different chemical species predicted by the 3D, average ⟨3D⟩, and 1D model atmospheres (Fig. 2.2). This behavior is defined essentially by differences in the ionization potentials of different atoms, with species characterized by the lowest ionization potential showing largest sensitivity of their number densities to the temperature fluctuations.

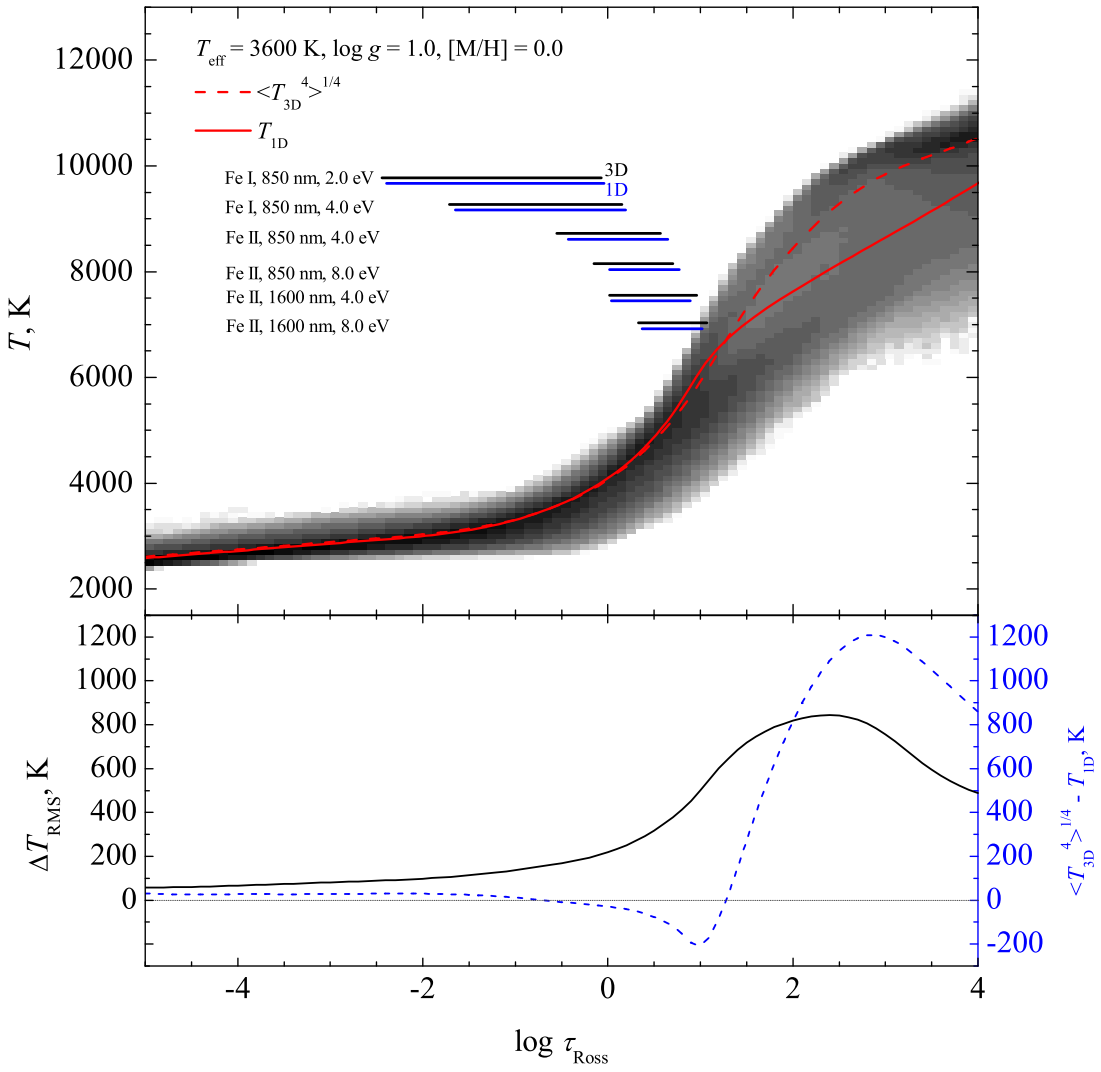

Fig. 2.1. Top panel: temperature profiles in three model atmospheres of cool red giant: 3D hydrodynamical (density plot), average ⟨3D⟩ (red solid line, average over the 14-snapshot ensemble), and 1D LHD ($\alpha_{\rm MLT}$=1.0; red dashed line). Horizontal bars indicate approximate formation regions of Fe I and Fe II lines in the 3D and 1D models, at different wavelengths and line excitation potentials (bars mark the regions where 90% of line equivalent width is acquired, i.e., between 5% and 95% of the total EW). **Bottom panel:** RMS horizontal temperature fluctuations at constant $\tau_{\rm Ross}$ in the 3D model (black solid line, 14-snapshot ensemble); and the difference between the temperature profiles corresponding to the average ⟨3D⟩ (14-snapshot ensemble average) and the 1D model atmospheres (blue dashed line).

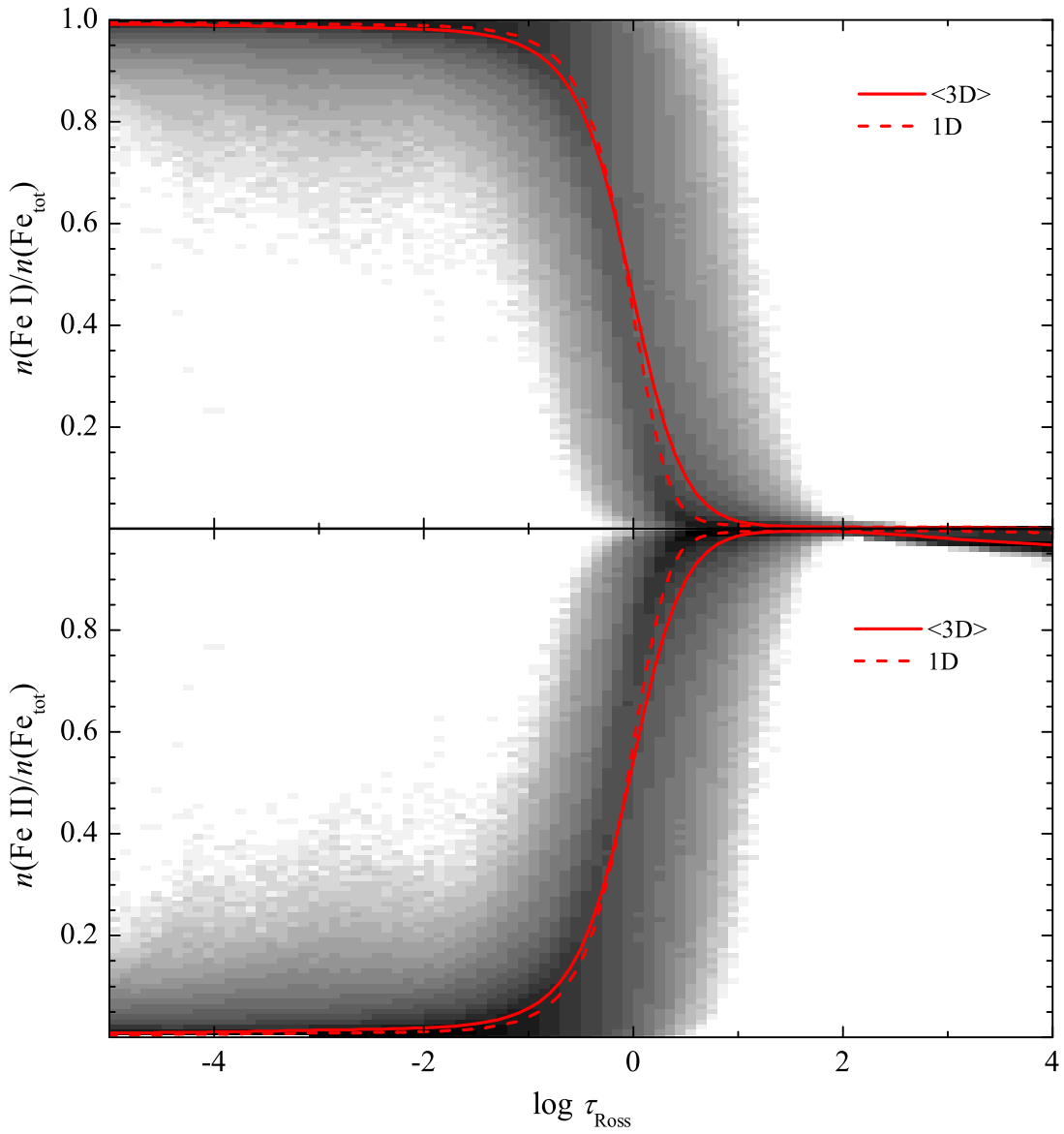

Fig. 2.2. Number densities of Fe I and Fe II (top-down), plotted versus $\tau_{\rm Ross}$for three model atmospheres of cool red giant: 3D hydrodynamical (density plot), average $\langle$3D$\rangle$ (solid line, 14-snapshot ensemble average), and 1D LHD ($\alpha_{\rm MLT}$=1.0; dashed line). The number densities of Fe I and Fe II are provided as fractions of the total iron number density, $n(\mathrm{Fe_{tot}})$.

2.1.3 The influence of convection on the spectral line formation: abundance corrections for lines of neutral atoms

The abundance corrections for neutral atoms are shown in Fig. 2.3, where they are plotted versus the difference between their ionization and excitation potentials, $E_{\rm ion} - \chi$. In such rendering, it is the difference $E_{\rm ion} - \chi$ that

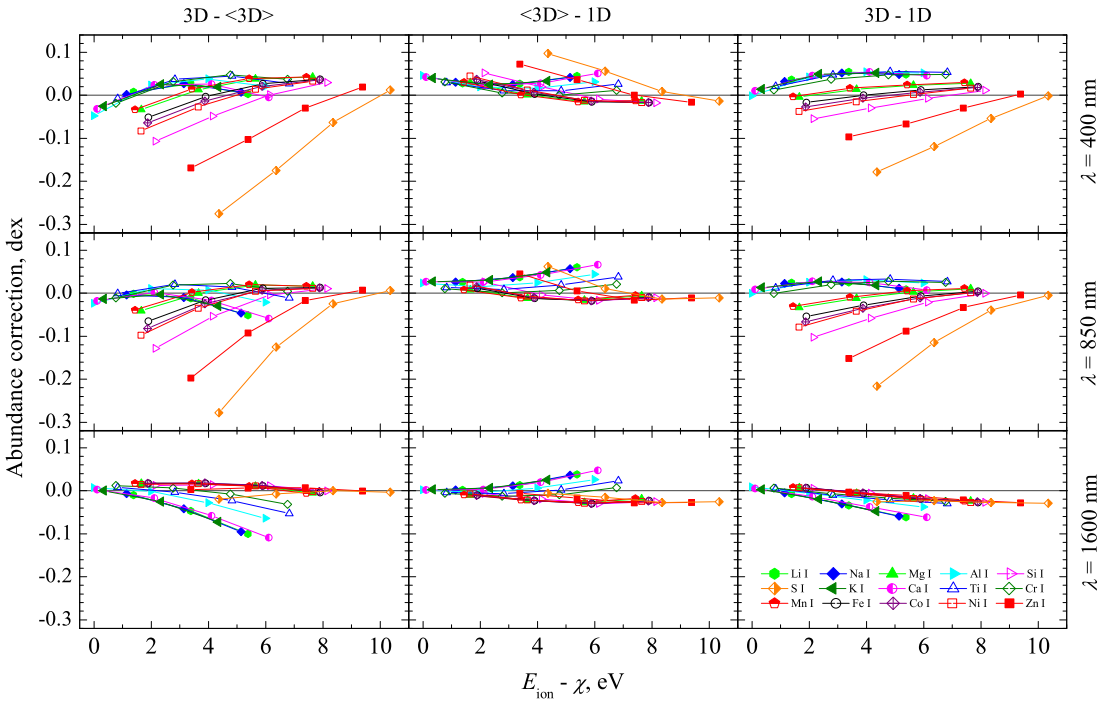

Fig. 2.3. Abundance corrections for spectral lines of neutral atoms, plotted versus the difference between their ionization energy and line excitation potential, $E_{\rm ion}-\chi$. The abundance corrections shown are $\Delta_{\rm 3D-\langle 3D\rangle}$ (left column), $\Delta_{\rm \langle 3D\rangle-1D}$ (middle column), and $\Delta_{\rm 3D-1D}$ (right column). Abundance corrections were computed at three different wavelengths: 400 nm (top row), 850 nm (middle row), and 1600 nm (bottom row). The ionization potentials of neutral atoms used in plotting this Figure are provided in Table 2.1.

defines the number density of the neutral atoms per unit mass of chemical elements which are almost completely ionized in the line forming layers. The abundance corrections shown in Fig. 2.3 must fall on top of each other for neutral atoms with the lowest ionization potentials. In the atmosphere of cool red giant studied here, such neutral elements as Li I, Na I, and K I are in their minority ionization stage throughout the entire atmosphere of this particular giant. For these elements, the abundance corrections $\Delta_{\rm 3D-1D}$, $\Delta_{\rm 3D-\langle 3D\rangle}$, and $\Delta_{\rm \langle 3D\rangle-1D}$ are in the range of $-0.1\ldots+0.05$ dex, with comparable contributions from $\Delta_{\rm 3D-\langle 3D\rangle}$ and $\Delta_{\rm \langle 3D\rangle-1D}$. All corrections are slightly more negative at $\lambda = 1600$ nm than they are at $\lambda = 850$ nm.

On the other hand, atoms with higher ionization potentials are predominantly neutral and for them the abundance correction curves in Fig. 2.3 begin to separate. Such behavior is a consequence of the combined action of excitation and ionization. Namely, ionization factor dominates over the excitation factor in defining the line opacity, $\kappa_\ell \sim \exp\{+(E_{\rm ion}-\chi)/kT\}$, as long

Table 2.1. Ionization potentials $E_{\rm ion}$ of selected neutral atoms.

Element	$E_{\rm ion}$, eV[a]	Element	$E_{\rm ion}$, eV[a]	Element	$E_{\rm ion}$, eV[a]
Li I	5.39	S I	10.36	Mn I	7.43
Na I	5.14	K I	4.34	Fe I	7.90
Mg I	7.65	Ca I	6.11	Co I	7.88
Al I	5.99	Ti I	6.83	Ni I	7.64
Si I	8.15	Cr I	6.77	Zn I	9.39

[a] NIST database, `https://www.nist.gov`

as neutral atoms are minority species. Thus, the line opacity decreases with increasing temperature and low-excitation lines are then most temperature sensitive. Opposite is true for neutral majority species. Here, excitation factor dominates over the ionization factor and the line opacity increases with increasing temperature. In this situation high-excitation lines are the most sensitive to temperature.

2.1.4 The influence of convection on the spectral line formation: abundance corrections for lines of ionized elements

Figure 2.4 displays the abundance corrections for selected ionized atoms (plus N I and O I) plotted versus the excitation potential χ. For ions representing majority ionization stage their line opacity depends on temperature as $\kappa_\ell \sim \exp\{-\chi/kT\}$. The majority neutral atoms N I and O I show exactly the same temperature sensitivity and hence their 3D–1D abundance corrections coincide with those of the majority ions. The corrections are vanishingly small for lines originating from the ground state and increase steadily with the excitation potential: for a number of chemical elements at $\chi = 10\,\mathrm{eV}$, $\Delta_{\mathrm{3D}-\langle\mathrm{3D}\rangle}$ correction amounts to $\approx -0.6\,\mathrm{dex}$ while $\Delta_{\langle\mathrm{3D}\rangle-\mathrm{1D}}$ reaches $\approx +0.2\,\mathrm{dex}$, thus leading to the total abundance correction of $\Delta_{\mathrm{3D}-\mathrm{1D}} \approx -0.4\,\mathrm{dex}$. For ions that are not pure majority species, the abundance corrections depend weakly on the ionization potential as well, thus systematically increasing in absolute size with $E_{\rm ion}$.

Basically, the curves shown in Fig. 2.4 reflect the temperature sensitivity of the line opacity. All abundance corrections are close to zero for $\chi = 0$

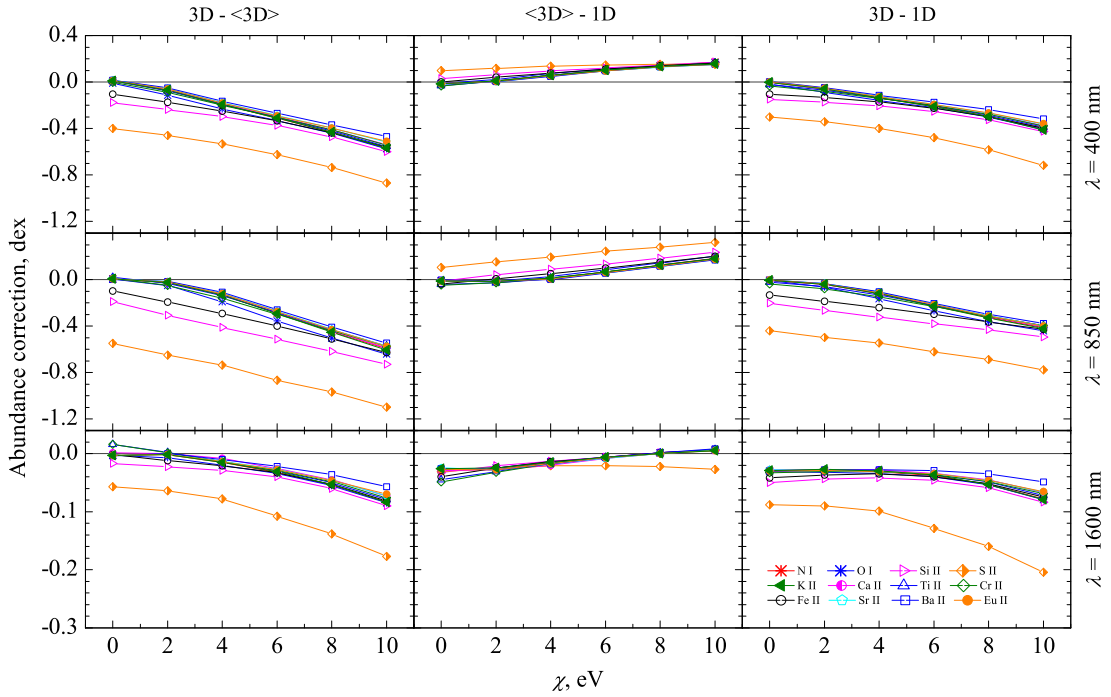

Fig. 2.4. Abundance corrections for spectral lines of ionized atoms (plus N I and O I), plotted versus the line excitation potential, χ (other notations as in Fig. 2.3).

eV, and increase systematically with χ. Since the $\langle$3D$\rangle$ model is cooler in the line forming regions than the 1D model, the same line is weaker in $\langle$3D$\rangle$ model than in the 1D model, such that $\Delta_{\langle 3D\rangle-1D}$ is positive. On the other hand, $\Delta_{3D-\langle 3D\rangle}$ is negative because the horizontally averaged line opacity in the 3D model exceeds the line opacity obtained from the horizontally averaged temperature, $\langle\kappa_\ell\rangle > \kappa_\ell(\langle T\rangle) \approx \kappa_\ell(T_{\langle 3D\rangle})$, essentially due to nonlinear temperature dependence of κ_ℓ ($\partial^2\kappa_\ell/\partial T^2 > 0$).

In this simple picture, the abundance corrections should be similar for all wavelengths, since the temperature sensitivity of the line opacity is wavelength independent (apart from a weak dependence through the stimulated emission factor). Obviously, this is not the case: the abundance corrections are much larger in the red at $\lambda\,850$ nm than in the near-IR at $\lambda\,1600$ nm, even though the near-IR lines form at deeper photospheric layers where the amplitude of the temperature fluctuations is larger (Fig. 2.1, lower panel). However, it is not the line opacity alone that determines the strength of a spectral line, but rather the ratio of line to continuum opacity. It turns out that in this particular model atmosphere of cool red giant the continuum opacity at $\lambda = 850\,$nm (due to H^- bound-free absorption) is al-

most independent of temperature, such that the strong T-dependence of the line opacity dominates the abundance corrections. At $\lambda = 1600\,\mathrm{nm}$, however, the continuum opacity (due to H^- free-free absorption) is strongly T-dependent, leading to a substantial reduction of the temperature sensitivity of the *ratio* κ_ℓ/κ_c, and hence, to much smaller abundance corrections than at $\lambda = 850\,\mathrm{nm}$.

2.2 Convection and spectral line formation at the base of the Red Giant Branch

Results obtained in Section 2.1 have shown that convection may indeed play an important role in the spectral line formation taking place in the atmosphere of cool red giant star located close to the tip of RGB (atmospheric parameters $T_{\rm eff} = 3660$ K, $\log g = 1.0$, and [M/H] = 0.0). It is therefore important to understand whether such conclusion can be extended to red giant stars characterized with different atmospheric parameters. On the other hand, it would be especially interesting to investigate the role of convection at different metallicities. In their pioneering study, Collet et al. (2007) have found that differences in the abundances predicted with the 3D hydrodynamical and classical 1D model atmospheres of red giant stars strongly depended on the metallicity, and for certain elements could reach to −1.0 dex at [M/H] = −3.0.

Hence, it would be important to verify these conclusions using a different set of model atmospheres, and to extend the analysis of Collet et al. (2007) by focusing on a larger number of chemical elements and wider range of spectral line parameters. Results obtained during this investigation are provided in Sections 2.2.1–2.2.6 below.

2.2.1 Model atmospheres

The 3D hydrodynamical models used in this part of our study were taken from the CIFIST model atmosphere grid which cover stars on the main sequence, subgiant, and red giant branches (Ludwig et al. 2009). The model atmospheres were computed using the 3D hydrodynamical CO^{5}BOLD model atmosphere code in the "box-in-a-star" setup, where part of the stellar atmosphere modeled is small compared to the size of a star itself (Freytag

et al. 2012). The simulations were performed on a Cartesian grid of $160 \times 160 \times 200$ grid points in x, y, z direction, respectively. Other properties of the model calculations were very similar to those used to compute the model of cool red giant studied in Section 2.1. Namely, the model box had open upper and lower boundaries (matter was allowed to enter and leave the simulation box freely), and periodic boundaries in the horizontal direction (matter leaving the box on one side was entering it again from the opposite side). We used monochromatic opacities from the `MARCS` stellar atmosphere package (Gustafsson et al. 2008) which were grouped into a smaller number of opacity bins using the opacity binning technique (Nordlund 1982; Ludwig et al. 1994; Vögler et al. 2004), with five opacity bins for the [M/H] = 0.0 model and six bins for the [M/H] = −1.0, −2.0, and −3.0 models. Solar-scaled elemental abundances used were those from Asplund et al. (2005). It is important to stress that we also applied a constant enhancement in the alpha-element abundances of $[\alpha/\mathrm{Fe}] = +0.4$ for the models at metallicities $[\mathrm{M/H}] \leq -1.0$. All model simulations were performed under the assumption of local thermodynamic equilibrium, LTE. Scattering was treated as true absorption and magnetic fields were neglected.

Parameters of the individual 3D model atmospheres used in this work are provided in Table 2.2. One may notice that each model is characterized by slightly different average effective temperature, $\langle T_{\mathrm{eff}} \rangle$. This is because effective temperature is not the input parameter for calculating 3D model atmosphere with the `CO`^{5}`BOLD` code. Instead, one sets the value of entropy of inflowing gas at the bottom of the model atmosphere. Eventually, this determines radiative flux at the outer boundary and thus - the effective temperature of a given model. Another important aspect is that radiative flux leaving the model atmosphere is subject to random spatial and temporal fluctuations, due to stochastic nature of convection, which causes the effective temperature to fluctuate, too. Therefore, the effective temperature of the 3D hydrodynamical model atmosphere can not be set in advance and should be fine-tuned by adjusting the entropy flux at the lower boundary of the model atmosphere. Note, however, that differences between the average T_{eff} of individual 3D model atmospheres are small ($< 30\,\mathrm{K}$), while the effective temperatures of all models are very close to the target value of

$T_{\rm eff} = 5000\,{\rm K}$ (Table 2.2).

In our further analysis we have used 3D models which were computed after ≈40 days in stellar time, counting from the start of the calculation run. This was done to ensure that the 3D hydrodynamical models used in the analysis have reached full relaxation. This part of the simulation run spanned ≈8.4 days of stellar time at solar metallicity and ≈7 days at [M/H] = −3.0, with a time step of ≈3 minutes in stellar time.

The average ⟨3D⟩ models used in this part of our study were computed by horizontally averaging each 3D model structure in the subset of twenty 3D model snapshots selected for the spectral line synthesis calculations (see Section 2.2.2 below). As in the case of cool red giant model studied in Section 2.1, the fourth power of temperature was averaged on surfaces of equal optical depth.

The comparison 1D model atmospheres were calculated using the `LHD` code (Sect. 1.1.2). It should be noted that both 3D and 1D models used in this work shared identical atmospheric parameters (Table 2.2), chemical composition, equation of state, and opacities, allowing to make a strictly differential comparison of their predictions. Solar scaled chemical composition with alpha-element enhancement of +0.4 dex for metallicities [M/H] ≤ −1 was assumed, i.e., as it was done in the case of 3D hydrodynamical models.

Temperature stratification of the full 3D, average ⟨3D⟩, and 1D model atmospheres at [M/H] = 0.0 and −3.0 are shown in Fig 2.5 and Fig 2.6, respectively. One may notice immediately that the temperature profile of the full 3D hydrodynamical model differs significantly from that of the cool red giant studied in Section 2.1: in the present case, horizontal temperature fluctuations reach the minimum value close to the optical surface and then increase again towards the outer atmospheric layers. While this effect is mild at solar metallicity, it becomes strongly pronounced at [M/H] = −3.0. In such situation, one may thus anticipate larger influence of convection on the spectral line formation in the atmospheres of red giants at lowest metallicities.

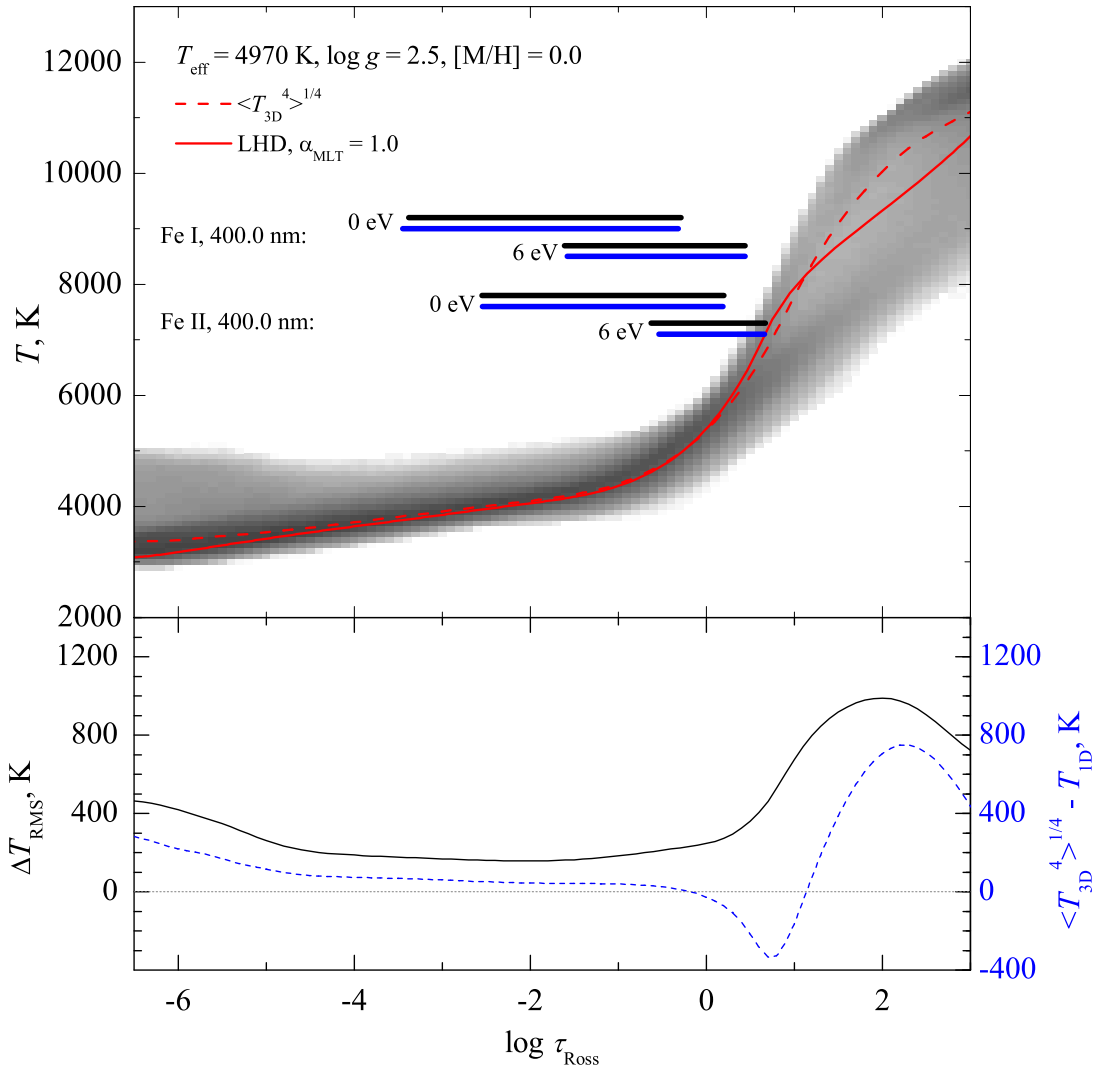

Fig. 2.5. Top panel: temperature profiles in the red giant model with $T_{\rm eff}/\log g/$ [M/H] = 4970/2.5/0.0, plotted versus the Rosseland optical depth, $\tau_{\rm Ross}$, and shown for the following model atmospheres: 3D (density plot), $\langle$3D$\rangle$ (dashed line), and 1D (solid line). Horizontal bars mark the approximate location of the Fe I and Fe II line formation regions in the 3D (black) and 1D (blue) atmosphere models, at λ = 400 nm and χ = 0 and 6 eV (bars mark the regions where the equivalent width, EW, of a given spectral line grows from 5% to 95% of its final value). **Bottom panel:** RMS horizontal temperature fluctuations in the 3D model (solid line), and difference between the temperature profiles of the $\langle$3D$\rangle$ and 1D models (dashed line), shown as functions of the Rosseland optical depth. In both panels, all quantities related to the 3D and $\langle$3D$\rangle$ models were obtained using the subset of twenty 3D model snapshots utilized in the 3D spectral line synthesis calculations (see Sect. 2.2.2).

Table 2.2. Atmospheric parameters of the CO5BOLD models located close to the bottom of RGB.

$T_{\rm eff}$, K	$\log g$	[M/H]	Grid dimension, Mm	resolution
4970	2.5	0	573×573×243	160×160×200
4990	2.5	−1	573×573×245	160×160×200
5020	2.5	−2	584×584×245	160×160×200
5020	2.5	−3	573×573×245	160×160×200

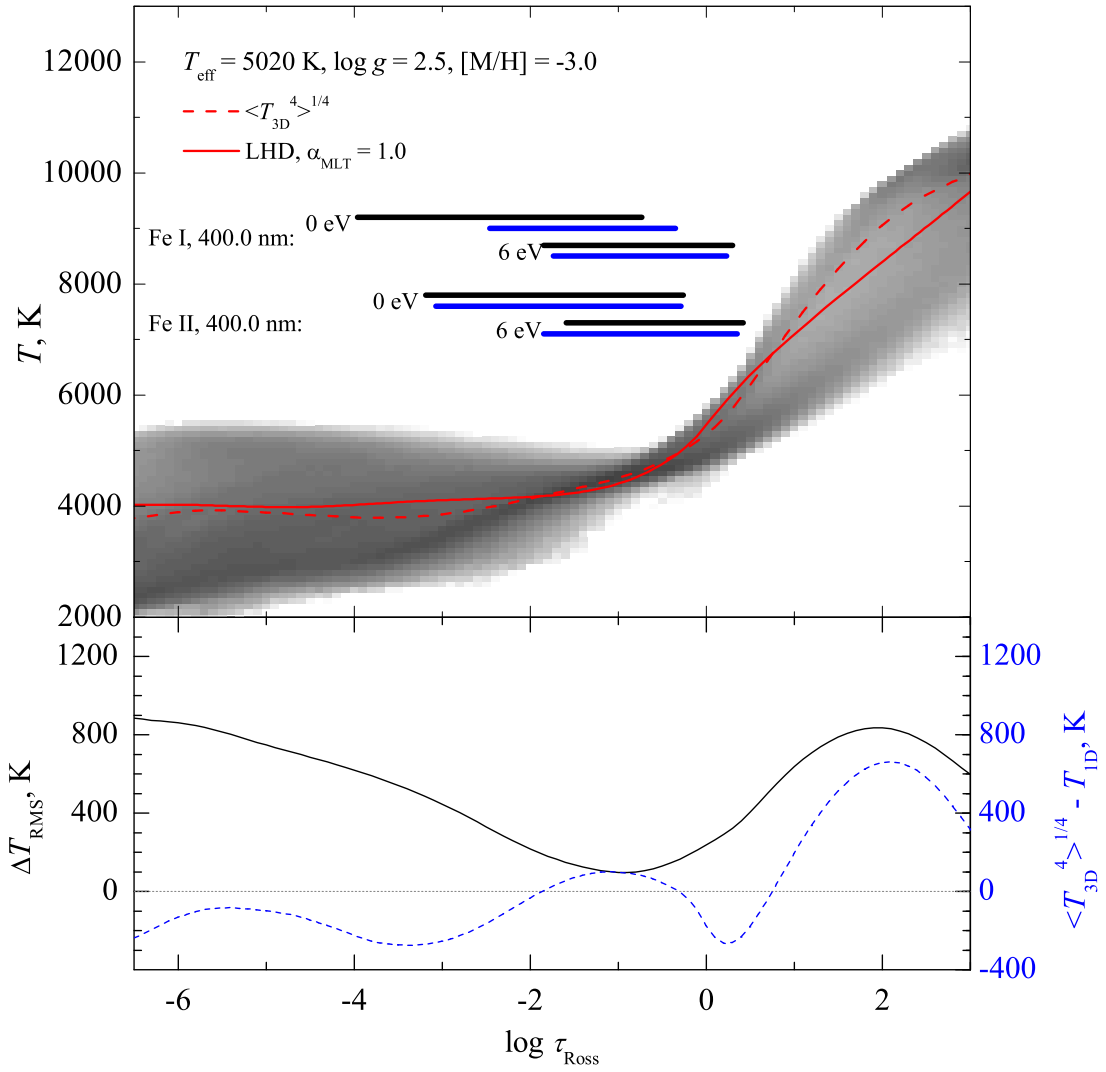

Fig. 2.6. Same as in Fig. 2.5 but for the red giant model with $T_{\rm eff}$/ log g/ [M/H] = 5020/2.5/ − 3.0.

2.2.2 Spectral line synthesis

To carry out spectral line synthesis for a full 3D simulation sequence (≈3600 snapshots) is computationally too demanding. We have therefore selected twenty 3D snapshots spaced at regular time intervals (≈8 hours) to speed up spectral line synthesis calculations, following the considerations outlined

in Section 1.2.2.

Spectral line synthesis was done with the `Linfor3D` code (Sect. 1.2.2) which solves the equation of radiation transfer under the assumption of LTE. Radiative transfer in the 3D model was solved for 3 vertical and 4 azimuthal directions. Line synthesis calculations were made in the range of Rosseland optical depths of $\log \tau_{\rm Ross} = 2.0$ to $\log \tau_{\rm Ross} = -6.0$, with a step of $\Delta \log \tau_{\rm Ross} = 0.08$. Line profiles were calculated at a high spectral resolution, thus typically, spectral line profiles was sampled with 130–150 wavelength points.

3D–1D abundance corrections were calculated for a number of astrophysically important neutral and singly ionized elements: Li I, C I, O I, Na I, Mg I, Mg II, Al I, Si I, Si II, Ca I, Ca II, Ti I, Ti II, Fe I, Fe II, Ni I, Ni II, Ba II, and Eu II. These elements form during different nucleosynthesis processes and are important tracers of various nucleosynthetic cycles. Besides the elements that were already included into similar investigation in Section 2.1, we added several new elements as well: Li, which is produced during the Big-Bang nucleosynthesis and by several other processes afterwards, including cosmic ray spallation in the interstellar medium and several stellar processes; Na and Al, which are important proton-capture elements; Mg and Ca, which represent α-elements; and Ba and Eu, which are important tracers of the s- and r-processes, respectively. We did not include nitrogen, because its lines become undetectably weak in stars with [M/H] < 0.

We have calculated 3D–1D abundance corrections for fictitious lines with the central wavelengths of $\lambda = 400$, 850, and 1600 nm, conceptually following our study presented in Section 2.1 to investigate the dependence of 3D–1D abundance correction on wavelength. In order to remind, the two bluest wavelengths were chosen to bracket the typical blue and red limits of modern optical spectrographs, such as UVES/GIRAFFE@VLT, HIRES@Keck, HDS@SUBARU, while the longer approximately coincides with the *H*-band of near-infrared spectrographs, such as CRIRES@VLT, NIRSPEC@Keck. On the other hand, the two reddest wavelengths coincide with the maximum and minimum of the bound-free absorption coefficient of the H^- ion at ~ 850 and ~ 1600 nm, while the bluest marks the spectral region where H^-

absorption becomes progressively smaller and opacities from various metals become increasingly more important.

Line excitation potentials were chosen to vary in steps of 2 eV from 0 to 6 eV. The 3D–1D abundance corrections were calculated for the weakest lines ($EW < 0.5$ pm, normalized to the equivalent width of a given line at $\lambda = 400$ nm), in order to avoid the influence of microturbulence velocity on the line equivalent width in 1D models. A microturbulence velocity of $\xi_{\rm mic} = 1.0\,{\rm km\,s^{-1}}$ was used in all $\langle$3D$\rangle$ and 1D spectral synthesis calculations, although, because of the very small line equivalent widths, the choice of $\xi_{\rm mic}$ had a negligible influence on the computed line strengths.

2.2.3 The influence of convection on the spectral line formation: abundance corrections for neutral atoms

The 3D–1D abundance corrections for neutral atoms that were computed using the model atmospheres of red giants located close to the bottom of RGB are plotted in Fig. 2.7, 2.8, and 2.9, for $\lambda = 400$, 850, and 1600 nm, respectively. Each figure shows three abundance corrections, $\Delta_{\rm 3D-\langle 3D\rangle}$, $\Delta_{\rm \langle 3D\rangle-1D}$, and $\Delta_{\rm 3D-1D}$, plotted versus metallicity at four different line excitation potentials, $\chi = 0$, 2, 4, and 6 eV.

For some elements, one may notice a strong dependence of the abundance corrections on metallicity: corrections are small at [M/H] = 0.0 and −1.0 but they grow quickly with decreasing metallicity and for certain elements may reach to −0.8 dex at [M/H] = −3.0 (Fig. 2.7–2.9). Abundance corrections are largest at the lowest excitation potentials, $\chi = 0, 2$ eV, but they quickly decrease with increasing χ: corrections then become both small (less than ±0.1 dex) and essentially independent of metallicity. Such behavior is defined by the atomic properties of chemical elements and the location of line formation regions associated with particular spectral lines. At all metallicities, lines with lower excitation potentials form in the outer atmospheric layers, but their formation regions shift deeper into the atmosphere with increasing χ (Fig. 2.5-2.6). At solar metallicity, differences between the temperature profiles of the $\langle$3D$\rangle$ and 1D model atmospheres are small and change very little throughout the entire model atmosphere. Similarly, horizontal temperature fluctuations, as measured by their RMS value

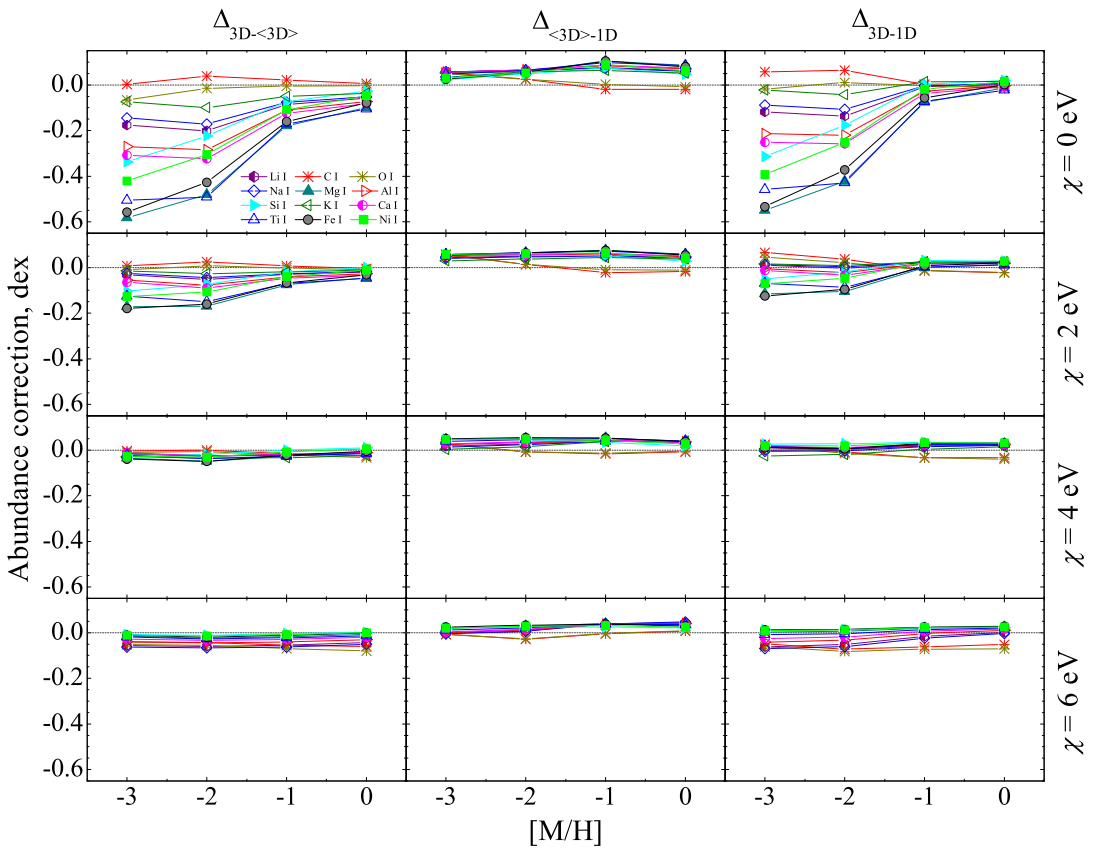

Fig. 2.7. Abundance corrections for spectral lines of neutral atoms plotted versus metallicity at $\lambda = 400\,\mathrm{nm}$: $\Delta_{\mathrm{3D-\langle 3D\rangle}}$ (left column), $\Delta_{\mathrm{\langle 3D\rangle-1D}}$ (middle column), and $\Delta_{\mathrm{3D-1D}}$ (right column). Corrections in each row were calculated at different excitation potentials, as indicated on the right side of each row.

($\Delta T_{\mathrm{RMS}} = \sqrt{\langle (T - T_0)^2 \rangle_{x,y,t}}$, here the angle brackets denote temporal and horizontal averaging on surfaces of equal optical depth, and $T_0 = \langle T \rangle_{x,y,t}$, is the depth-dependent average temperature) are not large either (i.e., if compared with their extent at lower metallicities) and change little with optical depth (Fig. 2.5). Therefore, at solar metallicity all three abundance corrections, $\Delta_{\mathrm{3D-\langle 3D\rangle}}$, $\Delta_{\mathrm{\langle 3D\rangle-1D}}$, and $\Delta_{\mathrm{3D-1D}}$, are small and nearly independent of the line excitation potential. On the other hand, differences in the temperature profiles of the $\langle$3D$\rangle$ and 1D models are larger in the outer atmosphere of low metallicity models (Fig. 2.6). Horizontal temperature fluctuations are also largest in the outer atmosphere, besides, they increase rapidly with decreasing metallicity. Consequently, at [M/H] < -1.0 the abundance corrections for most elements are largest for low-excitation lines, i.e., those that form farthest in the atmosphere. For such lines, $\Delta_{\mathrm{3D-\langle 3D\rangle}}$ correction is significantly larger than $\Delta_{\mathrm{\langle 3D\rangle-1D}}$, especially at lowest metallicities. Also,

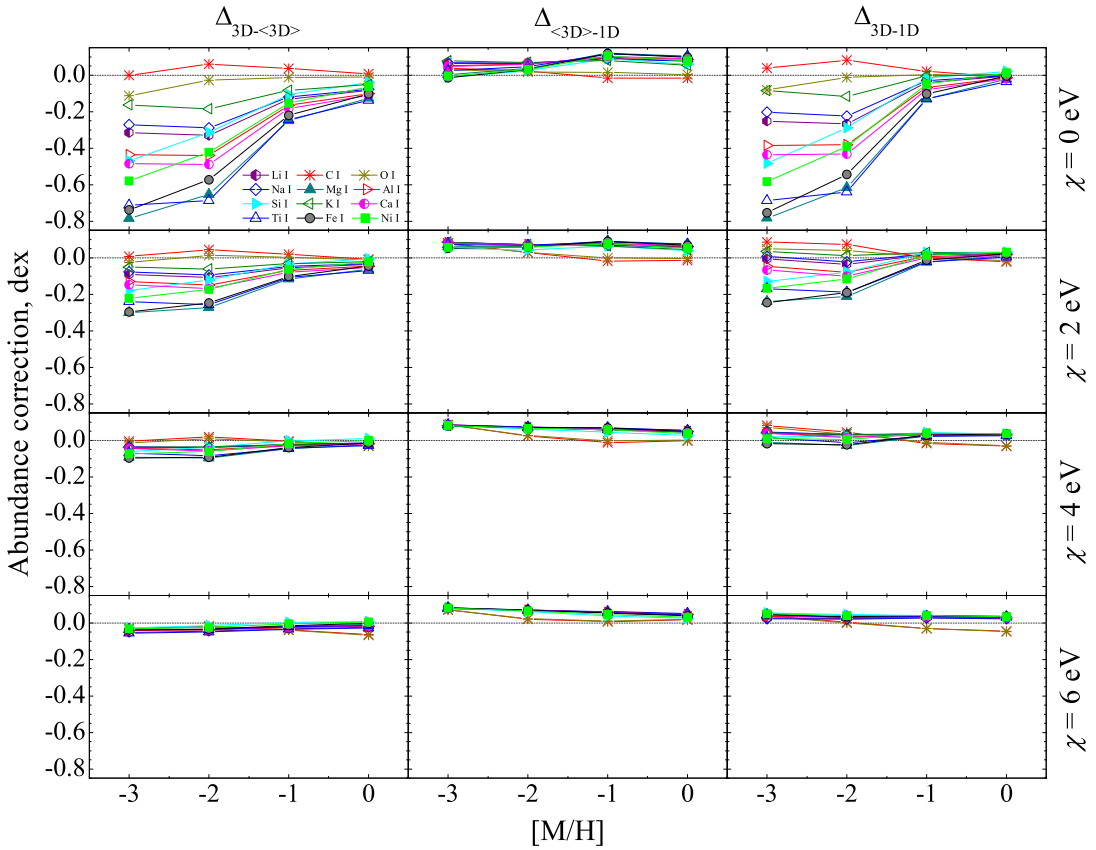

Fig. 2.8. The same as in Fig. 2.7 but at $\lambda = 850$ nm.

the two abundance corrections are nearly always of opposite sign, thus the absolute value of the total correction, $|\Delta_{\rm 3D-1D}|$, is smaller than the sum $|\Delta_{\rm 3D-\langle 3D\rangle}| + |\Delta_{\langle 3D\rangle-1D}|$.

One may notice however, that the size of $\Delta_{\rm 3D-1D}$ corrections at a given low metallicity may be very different for different elements, ranging roughly from -0.8 dex to $+0.1$ dex at [M/H] $= -3.0$ (Fig. 2.7–2.9). Such differences are caused by the interplay of ionization and excitation. Elements with the low ionization potential (such as Li I, Na I, K I) are nearly completely ionized throughout the entire atmosphere, at all metallicities. Therefore, neutral atoms of such elements are in their minority ionization stage. In all such cases the line opacity, κ_ℓ, can be roughly approximated as $\kappa_\ell \sim 10^{\theta\,(E_{\rm ion}-\chi)}$, where $\theta = 5040/T$ and $E_{\rm ion}$ is the ionization energy of a given element (see Kučinskas et al. 2013, Appendix A, eq. A5). In such cases, the line opacity becomes a very sensitive function of temperature at low χ. Consequently, for lines with low χ large temperature fluctuations in the outer atmospheric layers at low metallicities cause large variations in the

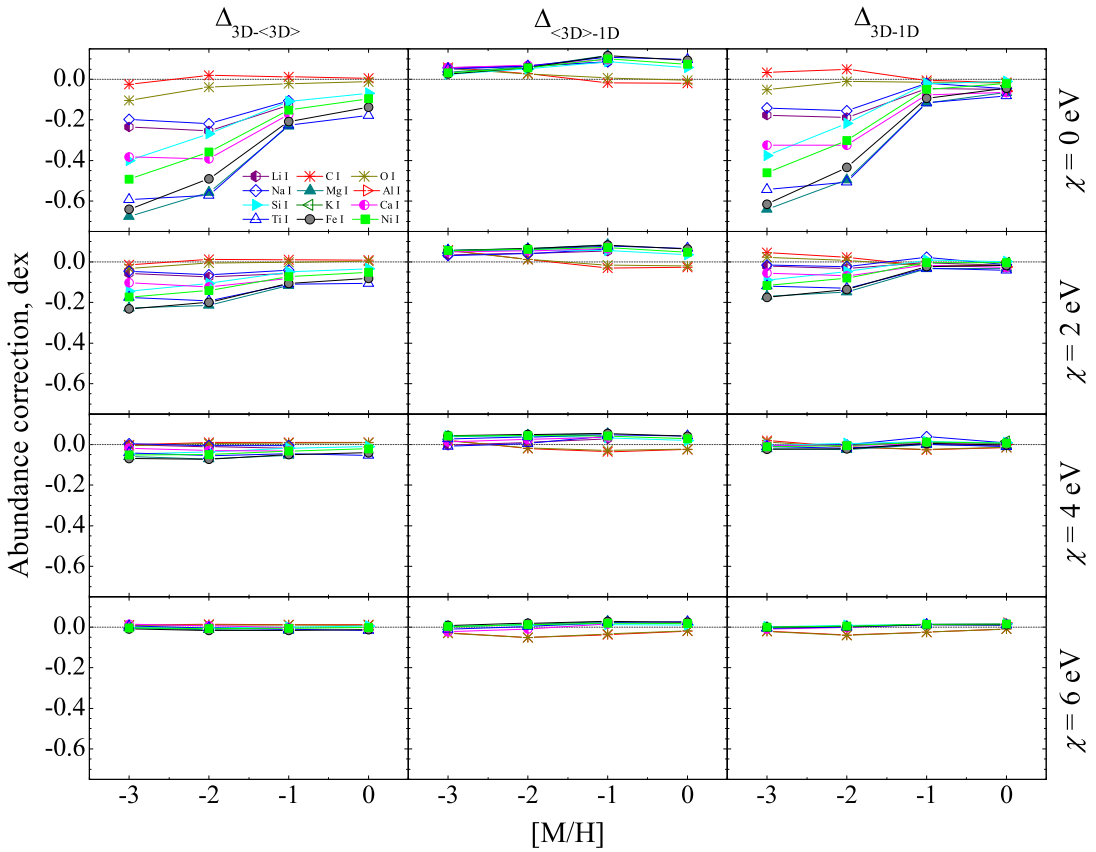

Fig. 2.9. The same as in Fig. 2.7 but at $\lambda = 1600$ nm.

line strength, which translate into large abundance corrections $\Delta_{\mathrm{3D-\langle 3D\rangle}}$, and thus $\Delta_{\mathrm{3D-1D}}$. On the other hand, neutral elements with high E_{ion}, such as C I, O I, are in their majority ionization stage. In such case, the excitation potential dominates over the ionization energy and thus the high-excitation lines become most sensitive to the temperature variations. In fact, the dependence of all abundance corrections for C I and O I on both [M/H] and χ is very similar to those of ionized elements.

Abundance corrections in the infrared wavelength range are very similar to those obtained either at $\lambda = 400$ or 850 nm, and for certain elements may reach to $\Delta_{\mathrm{3D-1D}} = -0.7$ dex. This is in contrast to the results obtained in case of significantly cooler red giant in Section 2.1, for which the abundance corrections at 1600 nm were significantly smaller than those in the optical wavelength range (see also Kučinskas et al. 2013). Obviously, this is not the case with red giants located close to the base of RGB since their abundance corrections are large at all wavelengths. These results therefore suggest that 3D–1D abundance corrections may not be inferred based on some simple

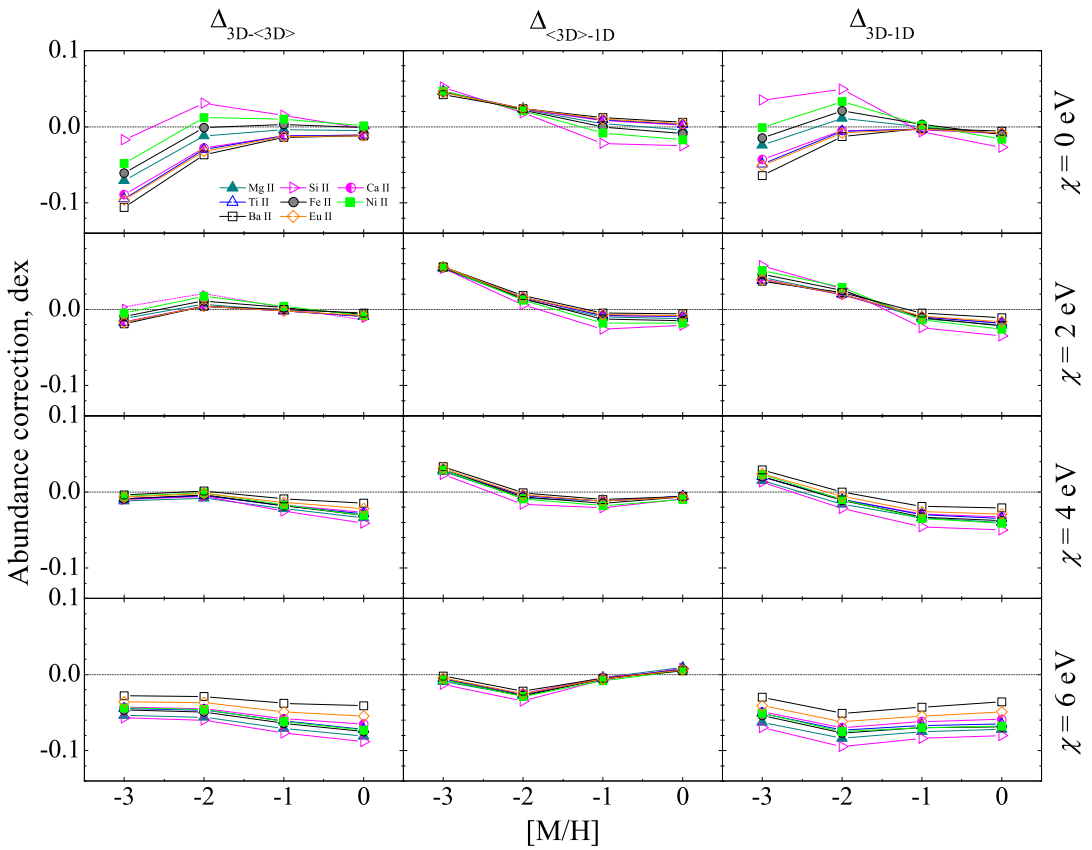

Fig. 2.10. Abundance corrections for lines ionized atoms plotted versus metallicity at $\lambda = 400$ nm: $\Delta_{\rm 3D-\langle 3D\rangle}$ (left column), $\Delta_{\rm \langle 3D\rangle-1D}$ (middle column), and $\Delta_{\rm 3D-1D}$ (right column). Corrections in each row were calculated at different excitation potentials, as indicated on the right side of each row.

considerations, and so their size becomes apparent only when the full 3D spectral line synthesis calculations are done.

2.2.4 The influence of convection on the spectral line formation: abundance corrections for ions

The 3D–1D abundance corrections for ionized atoms are shown in Fig. 2.10, 2.11, and 2.12, at $\lambda = 400$, 850, and 1600 nm, respectively. As in the case with neutral atoms, we provide three abundance corrections, $\Delta_{\rm 3D-\langle 3D\rangle}$, $\Delta_{\rm \langle 3D\rangle-1D}$, and $\Delta_{\rm 3D-1D}$, plotted versus metallicity at four different line excitation potentials, $\chi = 0$, 2, 4, and 6 eV.

At all [M/H] and χ studied here, the abundance corrections for lines of ionized atoms are confined to the range of $\sim \pm 0.1$ dex and show little sensitivity to changes in both metallicity and excitation potential (i.e., if compared to trends seen with lines of neutral atoms). Lines of ionized

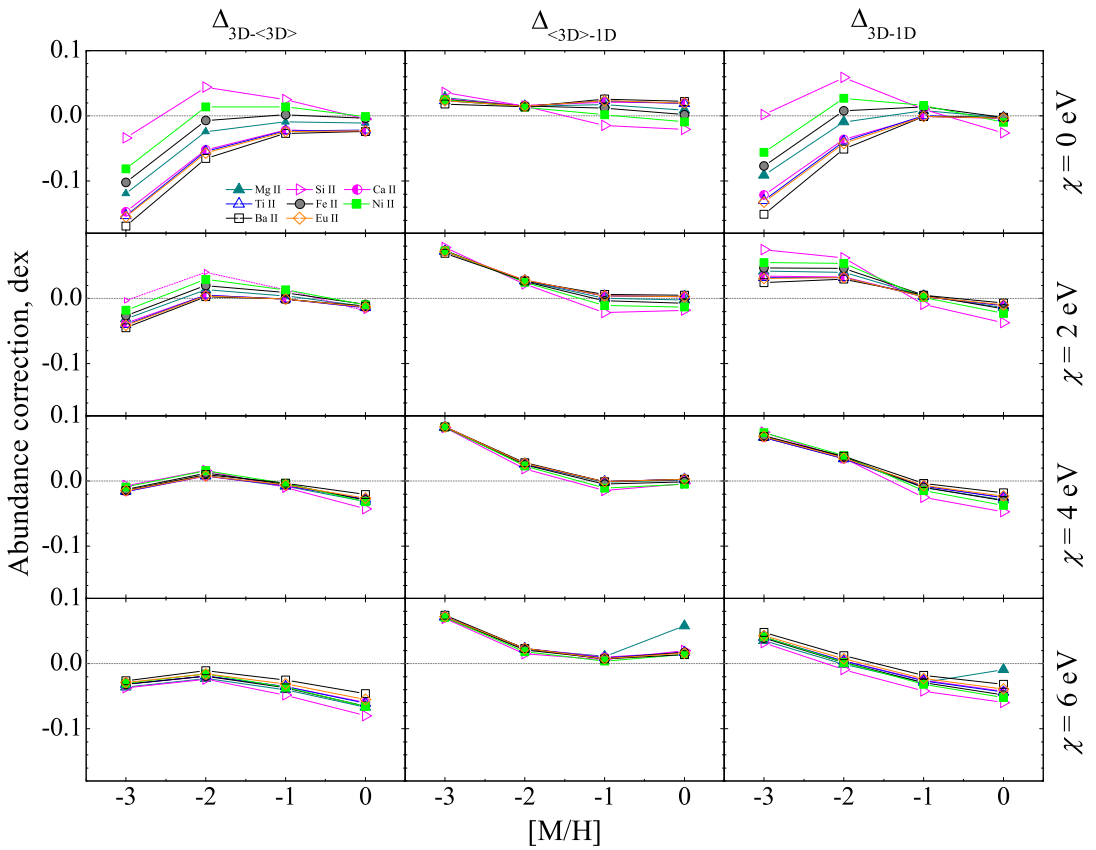

Fig. 2.11. The same as in Fig. 2.10 but at $\lambda = 850\,\mathrm{nm}$.

atoms form significantly deeper in the atmosphere where both the horizontal temperature fluctuations (which determine the size of $\Delta_{\mathrm{3D}-\langle\mathrm{3D}\rangle}$ correction) *and* the differences between temperature profiles of the $\langle$3D$\rangle$ and 1D models (which influence the size of $\Delta_{\langle\mathrm{3D}\rangle-\mathrm{1D}}$ correction) are smallest at all metallicities and change little with [M/H]. This leads to small abundance corrections that are insensitive to changes in [M/H] and χ. On the other hand, elements with lower ionization energies ($E_{\mathrm{ion}} < 6\,\mathrm{eV}$) are nearly completely ionized throughout the entire atmosphere of red giants studied here. For lines of such ionized elements it is the excitation potential that determines the line opacity, κ_ℓ, and thus the strengths of high-excitation lines are most sensitive to temperature fluctuations (see Kučinskas et al. 2013, Appendix B). Since temperature fluctuations are in fact smallest at the depths where such lines form, and because this holds at all metallicities, this too leads to $\Delta_{\mathrm{3D}-\mathrm{1D}}$ corrections that are small and show little variation with either metallicity or excitation potential (though, as expected, they increase slightly with χ).

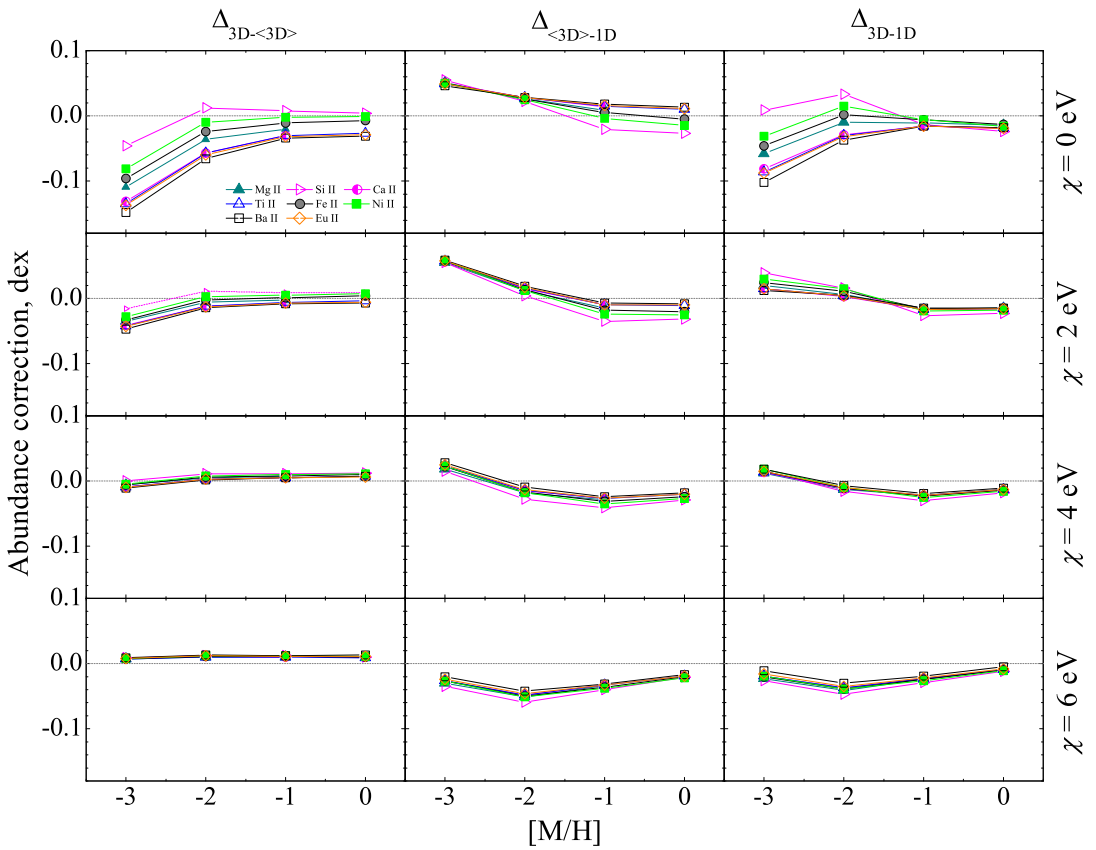

Fig. 2.12. The same as in Fig. 2.10 but at $\lambda = 1600$ nm.

It is worthwhile noting that $\Delta_{\mathrm{3D}-\langle\mathrm{3D}\rangle}$ and $\Delta_{\langle\mathrm{3D}\rangle-\mathrm{1D}}$ corrections are often of opposite sign, especially at the lowest metallicities, thus their sum leads to somewhat smaller total abundance corrections, $\Delta_{\mathrm{3D}-\mathrm{1D}}$. Since κ_ℓ is a highly nonlinear function of temperature, horizontal temperature fluctuations produce larger line opacities leading to stronger lines and thus, negative $\Delta_{\mathrm{3D}-\langle\mathrm{3D}\rangle}$ corrections. On the other hand, since the temperature of the $\langle$3D$\rangle$ model is generally lower than that of the 1D model in the line forming regions, lines of ionized species are weaker in $\langle$3D$\rangle$ than in 1D. This leads to positive $\Delta_{\langle\mathrm{3D}\rangle-\mathrm{1D}}$ corrections. As in the case of neutral atoms, abundance corrections at $\lambda = 1600$ nm are comparable to those obtained at 400 and 850 nm and may reach to -0.1 dex at [M/H] $= -3.0$.

As in the case with neutral atoms, abundance corrections at $\lambda = 1600$ nm are similar to those obtained at 400 and 850 nm and may reach to -0.6 dex at [M/H] $= -3.0$. Again, these results suggest that the use of 3D models may be essential when doing abundance work with red giants at low metallicities.

Qualitatively, the dependence of abundance corrections on metallicity

and excitation potential seen in Figs. 2.7–2.12 for neutral and ionized atoms is similar to the trends found by Collet et al. (2007), who computed abundance corrections for red giants with the atmospheric parameters nearly identical to those studied in this Section. One obvious difference between the results obtained in the two studies is that our abundance corrections are somewhat smaller. It is possible, however, that this discrepancy may be traced back to differences between the underlying 3D model atmospheres, i.e., the `STAGGER` code used by Collet et al. (2007), and the `CO5BOLD` code utilized in our study. Indeed, the two codes use different opacities and opacity binning techniques, different equations of state, and so forth. One should also note a major difference in the 1D model atmospheres used as reference: while opacities, microphysics, and numerical schemes used by the `CO5BOLD` and `LHD` codes are identical, opacities and EOS used with the 1D `MARCS` model atmospheres employed by Collet et al. (2007) were different from those utilized with their 3D hydrodynamical `STAGGER` model atmospheres.

2.2.5 Influence of the mixing-length parameter, $\alpha_{\rm MLT}$, on the abundance corrections

According to the Schwarzschild criterion for the onset of convection, `LHD` models predict that at Solar metallicity convective flux should be zero at around and above the optical depth unity (Fig. 2.13, top panel). The situation is slightly different at [M/H] $= -3.0$ where, because of the lower opacity, convection in the `LHD` models reaches into layers above the optical surface, with slightly different extension for different choices of the mixing-length parameter, $\alpha_{\rm MLT}$ (Fig. 2.13, bottom panel). The majority of spectral lines used in the abundance analysis have $\chi \leq 4\,{\rm eV}$ and typically form in the atmospheric layers above $\log \tau_{\rm Ross} = 0.0$. Such lines should therefore be insensitive to the choice of $\alpha_{\rm MLT}$, especially at solar metallicity. However, certain exceptions may occur in case of lines characterized by very high excitation potential that form at $\log \tau_{\rm Ross} \sim 0.0$ or slightly below.

To check the influence of the choice of $\alpha_{\rm MLT}$ used with the classical 1D models on the abundance corrections, we therefore made several test calculations using `LHD` model atmospheres computed with several mixing-length parameters, $\alpha_{\rm MLT} = 1.0, 1.5, 2.0$. Abundance corrections were computed for

several weak ($W < 0.5$ pm) fictitious lines of Fe I ($\chi = 0$ and 6 eV) and Fe II ($\chi = 6$ eV), at [M/H] = 0.0 and −3.0. The results obtained show that in the case of Fe I lines the dependence on $\alpha_{\rm MLT}$ at solar metallicity is indeed negligible, with the difference in the abundance corrections for $\alpha_{\rm MLT}$=1.0 and 2.0 of less than 0.01 dex ($\sim$ 0.04 dex for Fe II $\chi = 6$ eV line, Fig. 2.14). These differences are somewhat larger at [M/H] = −3.0 but in any case they are below $\sim$ 0.04 and $\sim$ 0.07 dex for Fe I lines with $\chi = 0$ and 6 eV, respectively. The differences are very similar for Fe II lines, too.

The variations in the abundance corrections with $\alpha_{\rm MLT}$ occur because the temperature profiles of the 1D models at different $\alpha_{\rm MLT}$ are slightly different at the optical depths where these spectral lines form. For example, temperature in the LHD model with $\alpha_{\rm MLT} = 1.0$ is slightly higher than in the model with $\alpha_{\rm MLT} = 2.0$ at the optical depths where the Fe II lines form. This leads to stronger Fe II lines in the model with $\alpha_{\rm MLT} = 1.0$. Since the lines computed with the 3D models are generally stronger than those obtained in 1D, stronger 1D lines at $\alpha_{\rm MLT} = 1.0$ lead to slightly less negative abundance corrections with respect to those obtained at $\alpha_{\rm MLT} = 2.0$.

These test results indicate that the choice of the mixing-length parameter used with the comparison 1D model atmospheres may be important in case of weak, higher-excitation spectral lines, which has also been discussed for the Sun by Caffau et al. (2009). One may expect that in case of stronger lines this dependence may become less pronounced, because such lines tend to form over a wider range of optical depths and typically extend into outer atmospheric layers which are insensitive to the choice of $\alpha_{\rm MLT}$ used in the 1D models. The results obtained here nevertheless indicate that this issue should be properly taken into account when computing abundance corrections for the higher-excitation spectral lines, especially at lower metallicities.

2.2.6 Scattering and spectral line formation

In the current generation of CO^{5}BOLD models scattering is treated as true absorption, which may be seen as rather crude approximation. Indeed, as it was discussed recently by Collet et al. (2011), the treatment of scattering may have a significant impact on the thermal structure of 3D model

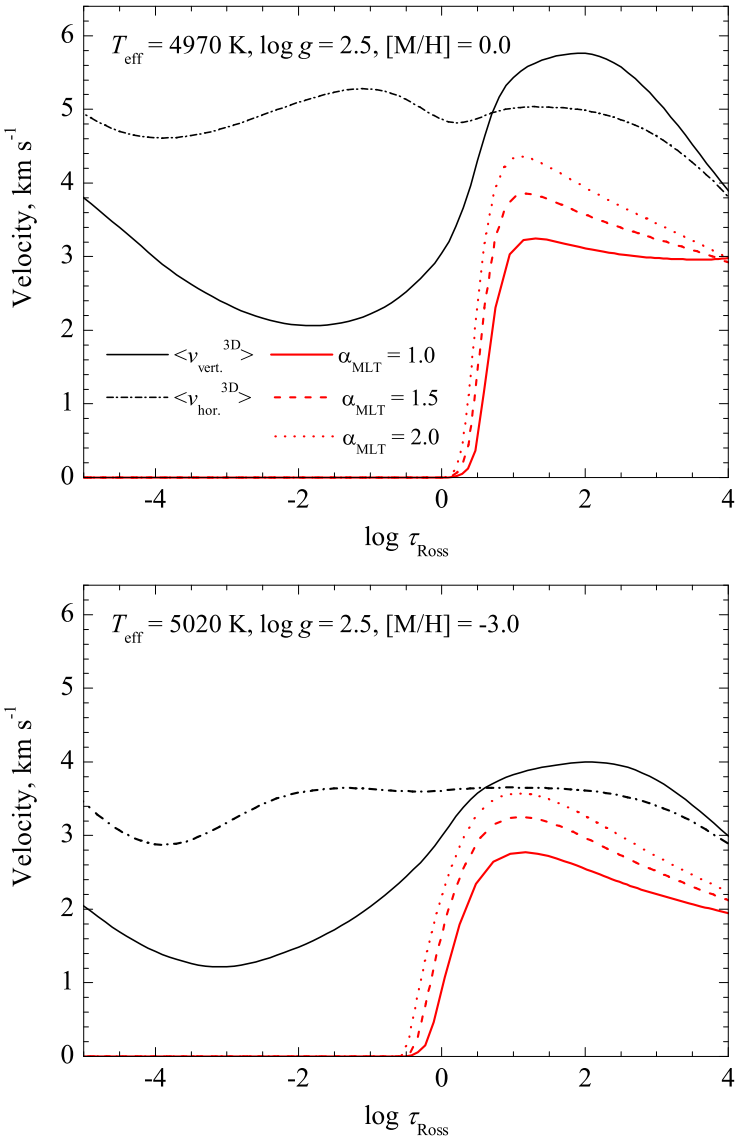

Fig. 2.13. Velocity profiles of the LHD models (red lines) at [M/H] = 0.0 (top panel) and [M/H] = −3.0 (bottom panel) computed using three different mixing-length parameters, $\alpha_{\rm MLT} = 1, 1.5, 2.0$. Vertical and horizontal velocity profiles of the average ⟨3D⟩ model (computed on the $\log \tau_{\rm Ross}$ iso-surfaces are shown as solid and dot-dashed black lines, respectively.

atmospheres. In their study, coherent isotropic scattering was implemented in the model atmosphere code and the obtained model structures were compared with those where continuum scattering was treated either as true absorption or scattering opacity was neglected in the optically thin regions. These tests have shown that in the former case the resulting temperature profiles were significantly warmer with respect to those calculated with coherent isotropic scattering. It has been thus argued by Collet et al.

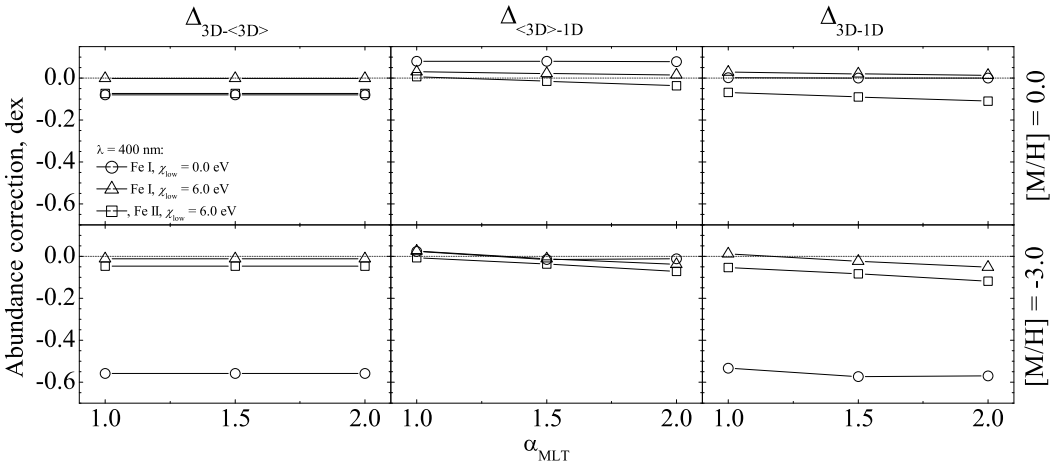

Fig. 2.14. Abundance corrections for two fictitious lines of neutral iron ($\chi = 0$ and 6 eV) and one of ionized iron ($\chi = 6$ eV) at 400 nm, plotted versus the mixing-length parameter $\alpha_{\rm MLT}$ used with the 1D LHD model atmospheres, at [M/H] = 0.0 (top row) and [M/H] = −3.0 (bottom row). Three types of abundance corrections are shown: $\Delta_{\rm 3D-\langle 3D\rangle}$ (left column), $\Delta_{\rm \langle 3D\rangle-1D}$ (middle column), and $\Delta_{\rm 3D-1D}$ (right column). Note that $\Delta_{\rm 3D-\langle 3D\rangle}$ abundance correction is not influenced by the choice of $\alpha_{\rm MLT}$ (there is no comparison 1D model atmosphere involved); we nevertheless show all three abundance corrections to provide an indication of the absolute size of abundance corrections involved and the range of their variations with $\alpha_{\rm MLT}$.

(2011) that the different thermal structures obtained with the STAGGER and CO^{5}BOLD codes may be due to the different treatment of scattering. Interestingly, the authors also found that in case when scattering opacity was neglected in the optically thin regions the resulting temperature profile was very similar to that obtained when scattering was properly included into the radiative transfer calculations.

The role of scattering in the CO^{5}BOLD model atmospheres has been recently studied by Ludwig & Steffen (2012) who compared thermal structures of the standard CO^{5}BOLD models (i.e., those calculated with continuum scattering treated as true absorption) and the CO^{5}BOLD models computed with continuum scattering opacity left out in the optically thin regions. Surprisingly, temperature profiles in the two models were different by only ∼ 120 K at $\tau_{\rm Ross} = -4.0$, in contrast to ∼ 600 K obtained by Collet et al. (2011) with the STAGGER models. While the exact cause of this difference is still unclear, Ludwig & Steffen (2012) have suggested that they may be due to different procedures used to compute binned opacities utilized with the CO^{5}BOLD and STAGGER model atmospheres.

Obviously, it is important to understand the consequences that the dif-

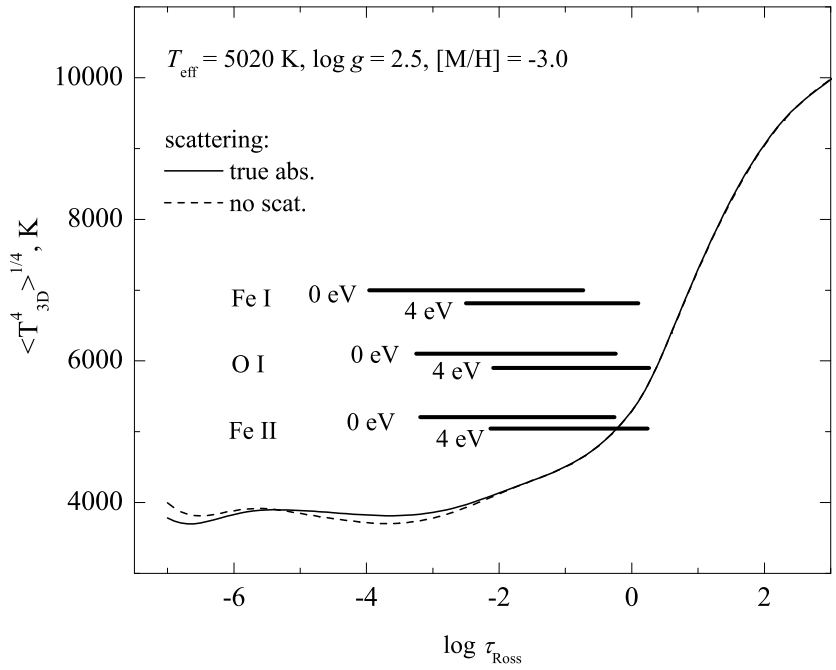

Fig. 2.15. Temperature profiles of the average ⟨3D⟩ model ($T_{\rm eff} = 5020\,{\rm K}$, $\log g = 2.5$, and $[{\rm M/H}] = -3.0$) calculated with scattering treated as true absorption (solid line) and with scattering opacity neglected in the optically thin regions (dashed line). Horizontal bars indicate the approximate location where lines of several trace elements form, at $\lambda = 400\,{\rm nm}$ and $\chi = 0$ and $4\,{\rm eV}$ (bars mark the regions where the equivalent width, EW, of a given spectral line grows from 5% to 95% of its final value).

ferences in the treatment of scattering may have on the temperature stratification in the model atmosphere which, in turn, may influence the spectral line formation. We therefore calculated a number of fictitious lines of several chemical elements (Li I, O I, Na I, Fe I, Fe II, Ni I, and Ba II), by utilizing the CO^{5}BOLD model in which scattering opacity was neglected in the optically thin regions (taken from Ludwig & Steffen 2012). According to the reasoning provided in Collet et al. (2011), the thermal structure of such models should be very similar to that in the models calculated with an exact treatment of scattering. Therefore, the comparison of line formation properties in these and standard models (i.e., those in which scattering is treated as true absorption) may allow to assess the importance of indirect effects of scattering on the spectral line formation, via its influence on the temperature profiles. Since scattering becomes increasingly more important at low [M/H] where both line and continuum opacities are significantly reduced, the lowest metallicity CO^{5}BOLD model was used for these

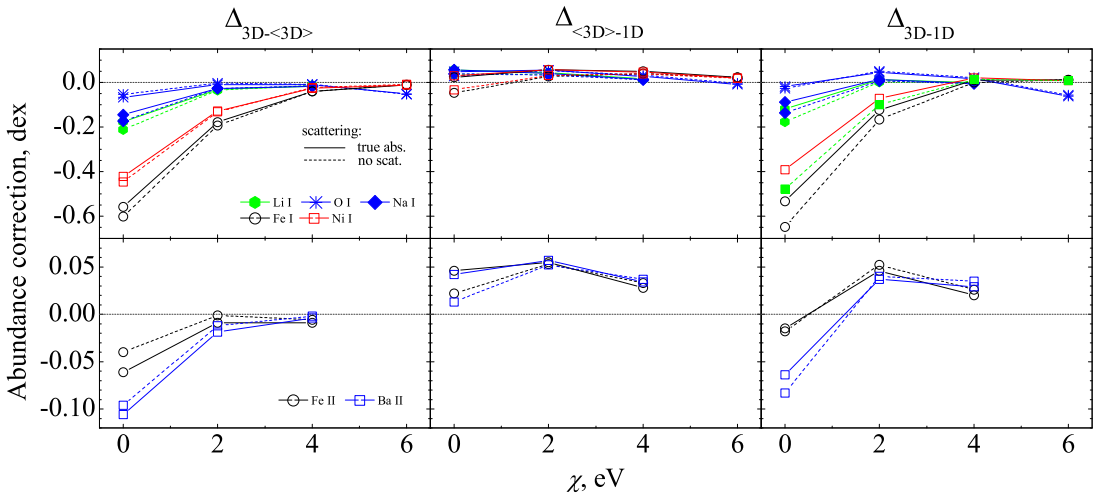

Fig. 2.16. Abundance corrections obtained for selected elements with the model atmospheres computed using different schemes for the treatment of scattering (plotted versus the excitation potential χ, for lines at $\lambda = 400\,\mathrm{nm}$). For each element, two cases are shown: (a) with scattering treated as true absorption (solid lines), and (b) with scattering opacity neglected in the optically thin regions (dashed lines). Atmospheric parameters of the model atmospheres are $T_{\rm eff} = 5020$, $\log g = 2.5$, and [M/H] $= -3.0$. Three types of abundance corrections are shown: $\Delta_{\rm 3D-\langle 3D\rangle}$ (left column), $\Delta_{\langle 3D\rangle-\rm 1D}$ (middle column), and $\Delta_{\rm 3D-1D}$ (right column). Top and bottom rows show abundance corrections for the neutral and ionized species, respectively.

tests ($T_{\rm eff} = 5020\,\mathrm{K}$, $\log g = 2.5$, and [M/H] $= -3.0$). Spectral line synthesis was performed using 20 fully relaxed 3D snapshots of this test model, using the procedure identical to that utilized with the standard CO5BOLD models (see Sect. 2.2.2). The abundance corrections obtained with this and the standard model are shown in Fig. 2.16.

The obtained results suggest that differences in the treatment of scattering within the CO5BOLD setup have only minor influence on the spectral line strengths. The abundance corrections obtained for the standard CO5BOLD model and the one in which scattering opacity was neglected in the optically thin regions differ by less than 0.1 dex, both for neutral atoms and ions (see Fig. 2.16). For models with scattering opacity neglected, slightly lower temperature in the outer atmospheric layers (Fig. 2.15) leads to somewhat larger abundance corrections for the low-excitation spectral lines of neutral atoms (∼0.1 dex). Since higher excitation lines form deeper in the atmosphere where differences in the thermal profiles are smaller, the influence of differences in the treatment of scattering becomes negligible for such lines,

with changes in the abundance corrections of less than 0.01 dex at $\chi > 4$ eV. Lines of ionized elements form deep in the atmosphere too, thus, irrespective of their excitation potential, differences in the treatment of scattering do not affect their line strengths.

Our results therefore suggest that the treatment of scattering may be important in case of the low-excitation lines with $\chi \leq 2$ eV. For elements such as sodium, where frequently only resonance or low-excitation lines are available for the abundance diagnostics, different recipes in the treatment of scattering may lead to systematic abundance differences of up to 0.1 dex at [M/H] = −3.0. On the other hand, strengths of high-excitation spectral lines, as well as lines of ionized elements, seem to be little affected by the choice of scattering prescription.

2.3 Convection and spectral line formation in the atmospheres of main sequence stars

Results obtained in Sections 2.1 and 2.2 have shown that convection indeed plays a significant role in the spectral line formation taking place in the atmospheres of red giant stars. As a consequence, differences in the abundances of chemical elements predicted with the 3D hydrodynamical and classical 1D model atmospheres may for certain elements reach to (or even exceed) −0.8 dex. Moreover, these differences depended strongly on the parameters of the underlying model atmosphere (such as metallicity), and atomic parameters of the spectral line used in the abundance determination. Clearly, such effects can not be ignored in stellar abundance work where typical errors in the abundance derivations are of the order of 0.1 dex or even smaller.

On the other hand, it is equally important to understand the role of such effects in the atmospheres of other types of stars, such as those located on the subgiant branch and the main sequence. In fact, atmospheric parameters of the red giants studied in Section 2.2 are not very different from those that are typical to subgiant stars. We would therefore expect that convection should play an equally important role in subgiants as it does in red giants, with the trends in abundance corrections qualitatively (and

Table 2.3. Atmospheric parameters of the CO5BOLD models of main sequence turn-off (TO) stars.

$T_{\rm eff}$, K	$\log g$	[M/H]	Grid dimension, Mm	resolution
5930	4.0	0	25.8×25.8×12.5	140×140×150
5850	4.0	−1	25.8×25.8×12.5	140×140×150
5860	4.0	−2	25.8×25.8×12.5	140×140×150

perhaps even quantitatively) very similar to those in the red giants studied in Section 2.2 (although, obviously, this should be rigorously checked in the future studies).

However, there has been no systematic study so far focusing on the interplay between convection and spectral line formation in the atmospheres of main sequence stars. Despite a few pioneering studies where the main sequence stars were studied with the aid of 3D hydrodynamical model atmospheres (González Hernández et al. 2009; Ramírez et al. 2009; Behara et al. 2010), the importance of convection in the spectral line formation in the atmospheres of main sequence stars still remains largely unknown.

In this Section we therefore present the results of our investigation of convection-related effects in the atmospheres of main sequence turn-off point (TO) stars. Similarly to the analysis presented in Sections 2.1 and 2.2, we investigate the differences in the abundances predicted with the 3D hydrodynamical and classical 1D model atmospheres, and physical reasons behind them.

2.3.1 Model atmospheres and spectral line synthesis

In this part of our study we used 3D hydrodynamical model atmospheres calculated with the CO5BOLD model atmosphere code (Freytag et al. 2012, see also Section 1.1.3), which, as in the case of red giant models, were taken from the CIFIST model atmosphere grid (Ludwig et al. 2009). Atmospheric parameters of the model atmospheres, as well as their physical and numerical extent are listed in Table 2.3. Such atmospheric parameters are roughly similar to those of the main sequence turn-off point (TO) stars in, e.g., mildly metal-poor ([Fe/H] ≈ -1) Galactic globular clusters, such as 47 Tuc ([Fe/H] $= -0.7$).

As in the analysis made in Sections 2.1 and 2.2, the model atmospheres were computed in the "box-in-a-star" setup, using a Cartesian grid of

$140 \times 140 \times 150$ grid points in x, y, z direction, respectively. Monochromatic opacities from the `MARCS` stellar atmosphere package (Gustafsson et al. 2008) were used in the model calculations, and were grouped into five opacity bins for the [M/H] $= 0.0$ model and six bins for the [M/H] $= -1.0$, and -2.0 models (for more on opacity binning see, e.g., Nordlund 1982; Ludwig et al. 1994; Vögler et al. 2004). Solar-scaled abundances were taken from Asplund et al. (2005), with a constant enhancement in the alpha-element abundances of $[\alpha/\mathrm{Fe}] = +0.4$ applied for the models at [M/H] ≤ -1.0. All model simulations were done under the assumption of LTE, with scattering treated as true absorption and magnetic fields neglected.

We further selected twenty 3D model snapshots for the spectral line synthesis computations. This snapshot subsample covers ≈6 days in stellar time and corresponds to ≈ 5 convective turnover times in the model atmosphere. As in the case of red giants, the snapshot selection was made to ensure that statistical properties of the smaller subsample would match as close as possible those of the full model run (see Section 1.1.3).

As in the previous Sections, spectral line synthesis was done with the `Linfor3D` code (Sect. 1.2.2), by covering a range of Rosseland optical depths spanning from $\log \tau_{\mathrm{Ross}} = 2.0$ to $\log \tau_{\mathrm{Ross}} = -6.0$, with a step of $\Delta \log \tau_{\mathrm{Ross}} = 0.08$ and typical resolution of $120 - 150$ wavelength points per line profile. The 3D–1D abundance corrections were calculated for the following chemical elements: C I, O I, Si I, Si II, Ti I, Ti II, Fe I, Fe II, Ba II, and Eu II. For this, fictitious spectral lines with the central wavelengths located at $\lambda = 400$, 850, and 1600 nm, and excitation potentials from 0 to 6 eV (with a step of 2 eV) were used. The 3D–1D abundance corrections were calculated for the weakest spectral lines, $EW < 0.5$ pm, to eliminate the influence of microturbulence velocity on the spectral line strength.

The average ⟨3D⟩ models were computed by horizontally averaging each 3D model structure in the subset of twenty 3D model snapshots. As in the case with red giant models, the fourth power of temperature was averaged on surfaces of equal optical depth (cf. Sections 2.1 and 2.2). The 1D model atmospheres were calculated with the `LHD` code (Sect. 1.1.2), by using atmospheric parameters (Table 2.3), chemical composition, equation of state, and opacities identical to those employed to compute 3D hydrody-

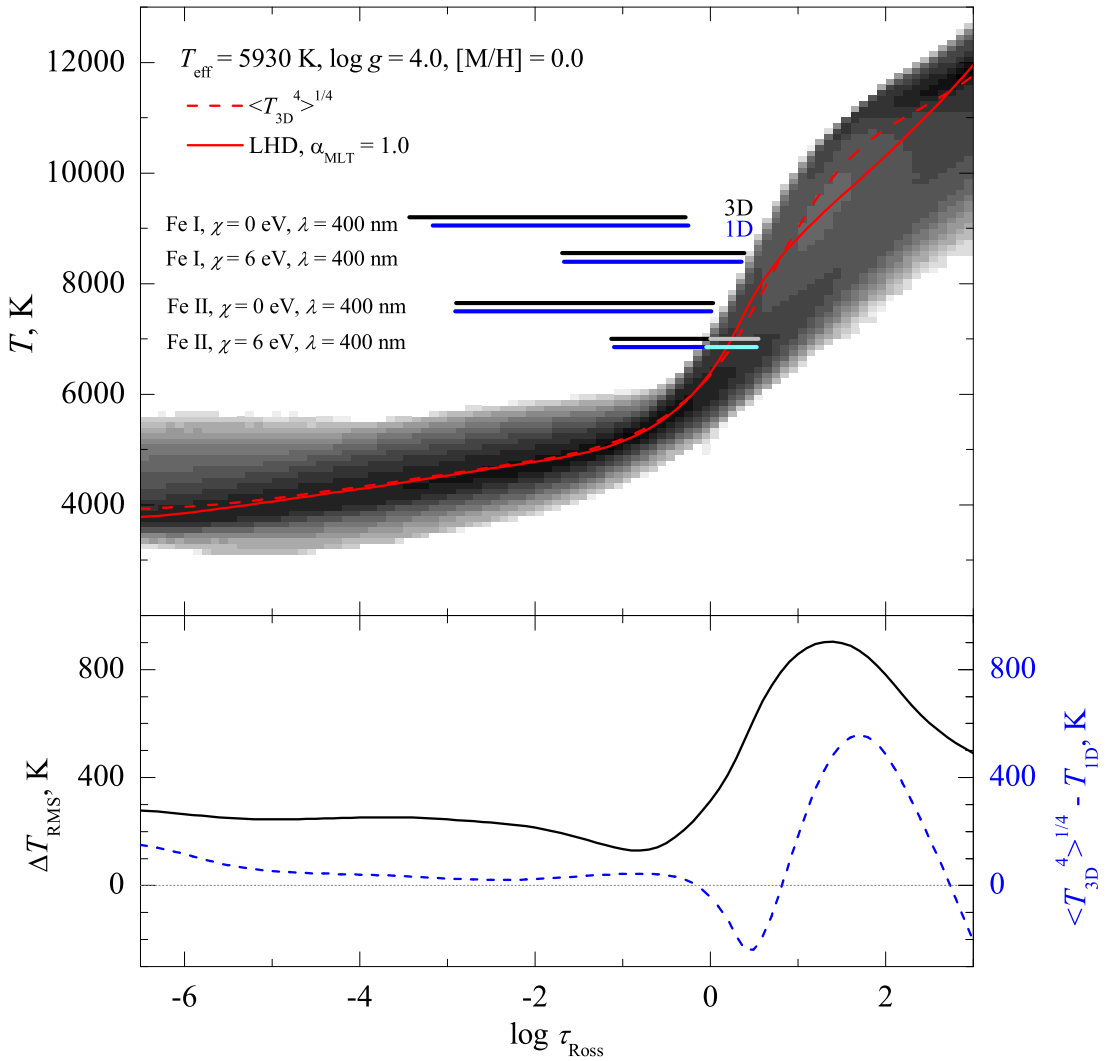

Fig. 2.17. Top panel: temperature profiles in the model atmosphere of TO star with $T_{\rm eff}$/ log g/ [M/H] = 5930/4.0/0.0, plotted versus the Rosseland optical depth, $\tau_{\rm Ross}$, and shown for the following model atmospheres: 3D (density plot), average ⟨3D⟩ (dashed line), and 1D (solid line). Horizontal bars mark the approximate location of the Fe I and Fe II line formation regions in the 3D (black) and 1D (blue) atmosphere models, at λ = 400 nm and χ = 0 and 6 eV (bars mark the regions where the equivalent width, EW, of a given spectral line grows from 5% to 95% of its final value). **Bottom panel:** RMS horizontal temperature fluctuations in the 3D model (solid line), and difference between the temperature profiles of the ⟨3D⟩ and 1D models (dashed line), shown as functions of the Rosseland optical depth.).

namical model atmospheres. A single value of the microturbulence velocity, $\xi_{\rm mic}$ = 1.0 km s^{-1}, was used in all ⟨3D⟩ and 1D spectral synthesis calculations.

Temperature stratification of the 3D hydrodynamical and classical 1D model atmospheres of TO stars are shown in Fig 2.17 and Fig 2.18 for the

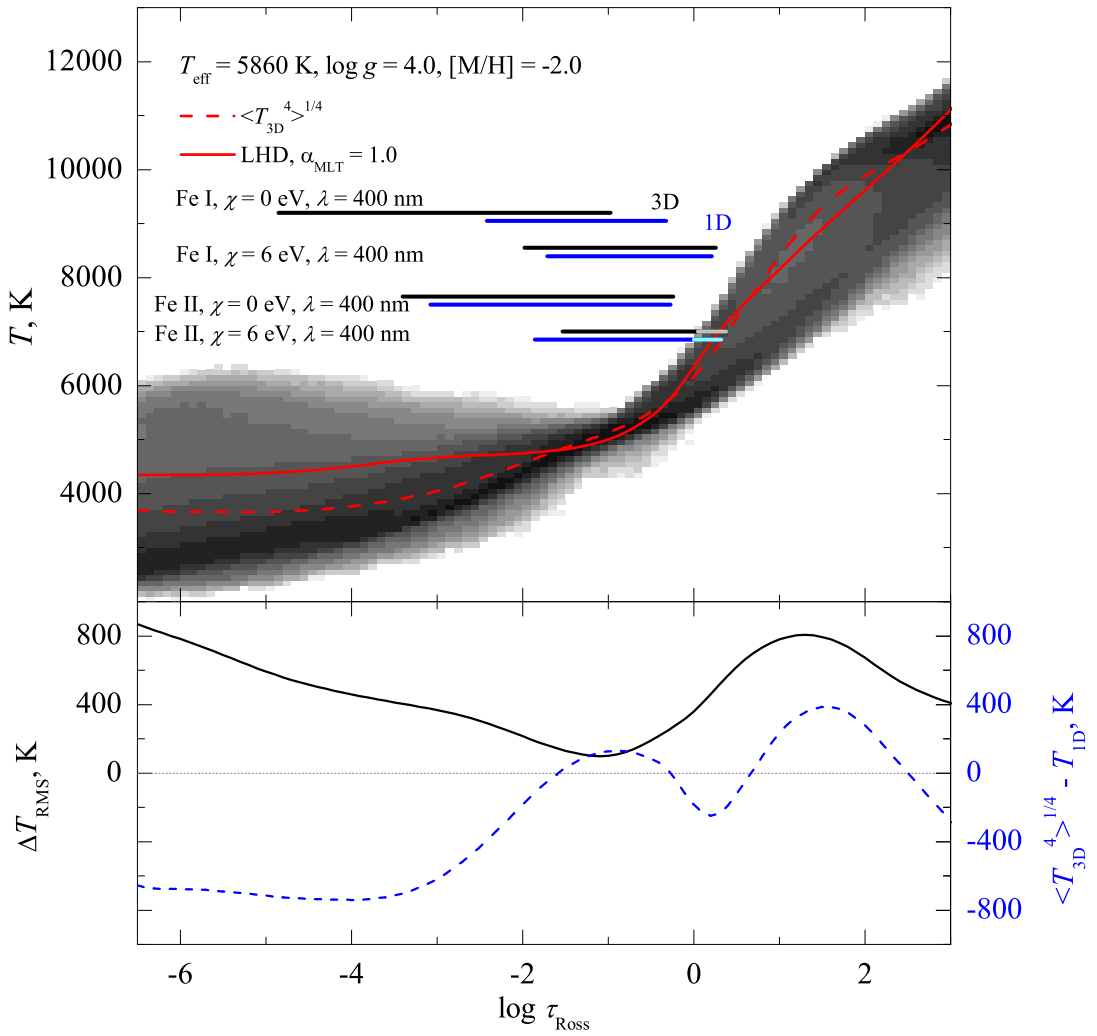

Fig. 2.18. Same as in Fig. 2.17 but for the model atmosphere with $T_{\rm eff}/\log g/$ [M/H] = 5860/4.0/ − 2.0.

[M/H] = 0.0 and −2.0 models, respectively. One aspect in which these models differ from those of red giant stars is readily visible in Fig 2.18: at lower metallicities, the difference between the temperature profiles of the average ⟨3D⟩ and 1D model atmospheres is significantly larger than it is in red giants. It may be thus anticipated that in the case of TO stars the $\Delta_{\langle 3D\rangle-1D}$ abundance corrections may play significantly more important role than they do in the atmospheres of red giants.

2.3.2 The influence of convection on the spectral line formation: abundance corrections for neutral atoms

The 3D–1D abundance corrections for neutral atoms computed using 3D hydrodynamical and classical 1D model atmospheres of TO stars are plotted

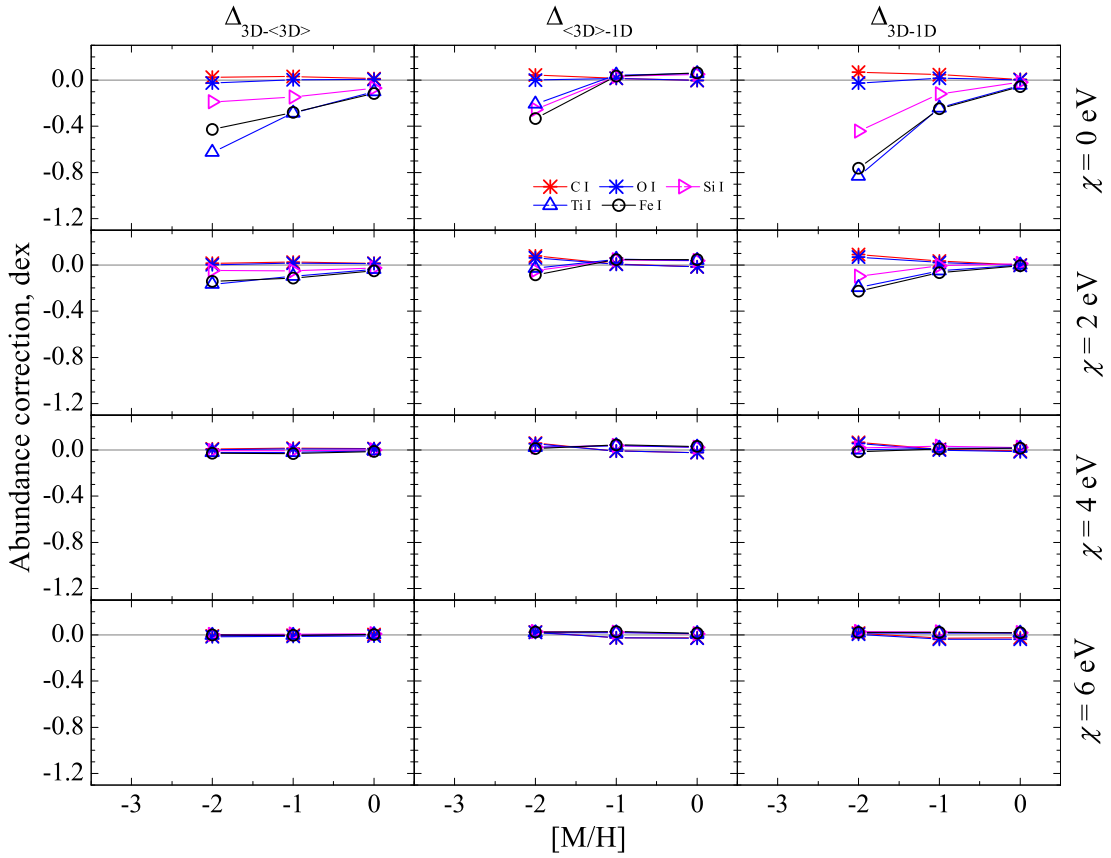

Fig. 2.19. Abundance corrections for spectral lines of neutral atoms plotted versus metallicity at $\lambda = 400$ nm: $\Delta_{\mathrm{3D-\langle 3D\rangle}}$ (left column), $\Delta_{\mathrm{\langle 3D\rangle-1D}}$ (middle column), and $\Delta_{\mathrm{3D-1D}}$ (right column). Corrections in each row were calculated at different excitation potentials, as indicated on the right side of each row.

in Fig. 2.19, 2.20, and 2.21, for $\lambda = 400$, 850, and 1600 nm, respectively. Each figure shows three abundance corrections, $\Delta_{\mathrm{3D-\langle 3D\rangle}}$, $\Delta_{\mathrm{\langle 3D\rangle-1D}}$, and $\Delta_{\mathrm{3D-1D}}$, plotted versus metallicity at four different line excitation potentials, $\chi = 0$, 2, 4, and 6 eV.

In general, the 3D–1D abundance corrections computed using the models of TO stars show very similar behavior to those obtained for the giant stars. There is a strong dependence of the abundance corrections on metallicity: corrections are small at [M/H] = 0.0 but they grow quickly with decreasing metallicity and for certain elements may reach to –1.1 dex at $\lambda = 850$ nm and [M/H] = −2.0 (Fig. 2.19–2.21). This is significantly larger than similar corrections obtained in the case of red giant stars (see Sect. 2.2.3). This is because the $\Delta_{\mathrm{\langle 3D\rangle-1D}}$ abundance corrections are larger in TO stars, which leads to larger total abundance corrections, $\Delta_{\mathrm{3D-1D}}$, than seen in red giant stars. This is an interesting result which indicates that the atmospheres of

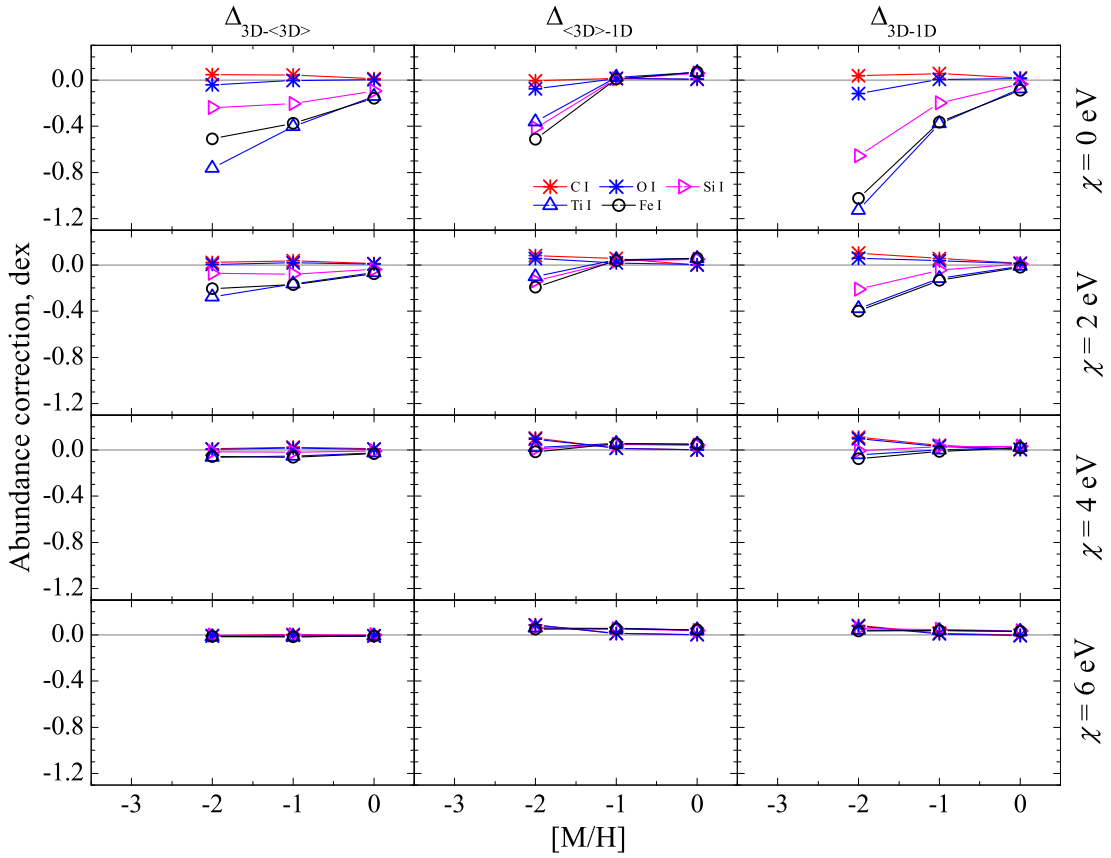

Fig. 2.20. The same as in Fig. 2.19 but at $\lambda = 850\,\mathrm{nm}$.

red giant and main sequence stars may be rather different, with the physical reasons causing these differences still awaiting to be understood.

Just as in the case with giants, the 3D–1D abundance corrections are largest at the lowest excitation potentials, $\chi = 0, 2\,\mathrm{eV}$ and they decrease with increasing χ. Such behavior is determined by the location of line formation regions associated with particular spectral lines, and the underlying physical conditions there, as in the case of giant stars. At all metallicities, lines with lower excitation potentials form in the outer atmospheric layers, but their formation regions move deeper into the atmosphere with increasing χ (Fig. 2.17-2.18). Therefore, the abundance corrections are largest for the lowest excitation lines which form in the atmospheric layers where both horizontal temperature fluctuations *and* differences in the temperature profiles of the average $\langle 3\mathrm{D} \rangle$ and 1D model atmospheres are largest.

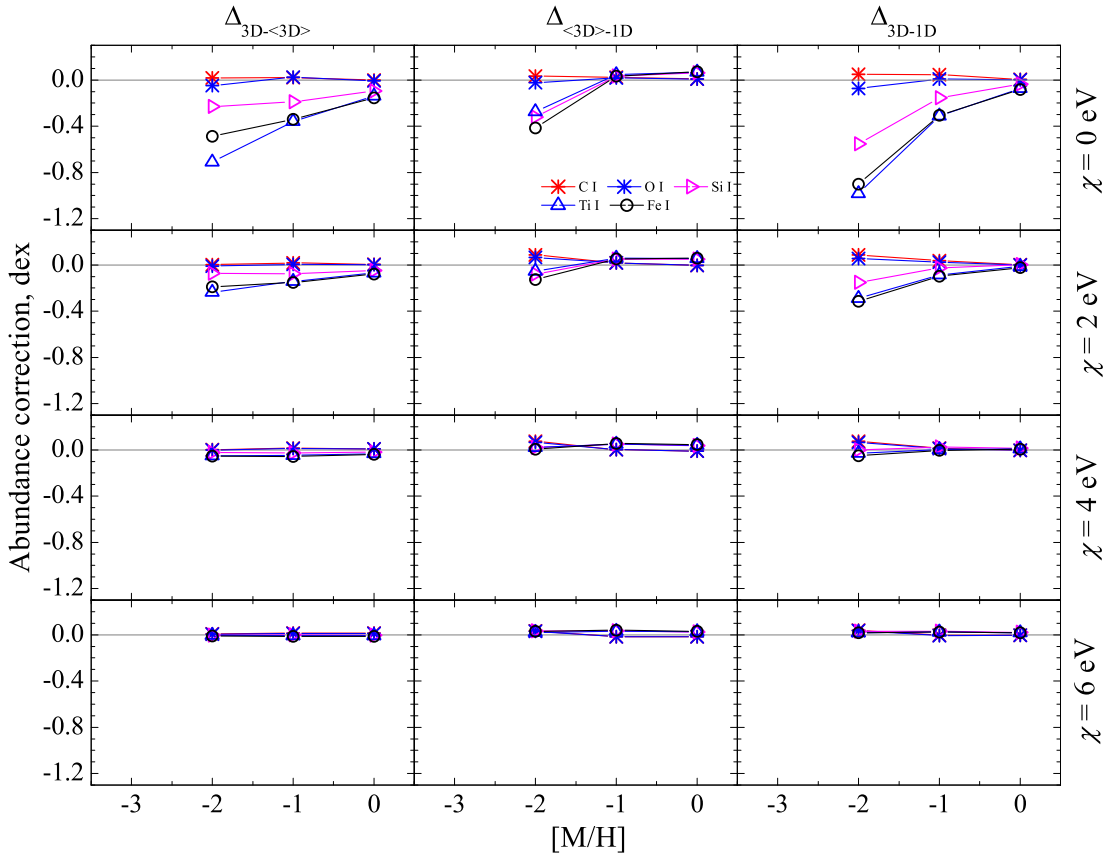

Fig. 2.21. The same as in Fig. 2.19 but at $\lambda = 1600$ nm.

2.3.3 The influence of convection on the spectral line formation: abundance corrections for ionized atoms

The 3D–1D abundance corrections for ionized atoms are shown in Fig. 2.22, 2.23, and 2.24, at $\lambda = 400$, 850, and 1600 nm, respectively. As in the case with neutral atoms, we provide three abundance corrections, $\Delta_{\rm 3D-\langle 3D\rangle}$, $\Delta_{\rm \langle 3D\rangle-1D}$, and $\Delta_{\rm 3D-1D}$, plotted versus metallicity at four different line excitation potentials, $\chi = 0$, 2, 4, and 6 eV.

The 3D–1D abundance corrections for low excitation potential lines are larger in case of turn-off point stars than those obtained for giant stars. We find that in case of TO stars and for the spectral lines at $\lambda = 850$ nm and $\chi = 0$ eV the total abundance correction may reach to -0.3 dex (Fig. 2.23), while in case of red giants it does not exceed ~ 0.1 dex (Fig. 2.11). Similarly to the spectral line formation in the red giant model atmospheres (Sect. 2.2.4) lines of ionized atoms form significantly deeper in the atmosphere of the TO star where both the horizontal temperature fluctuations (which determine

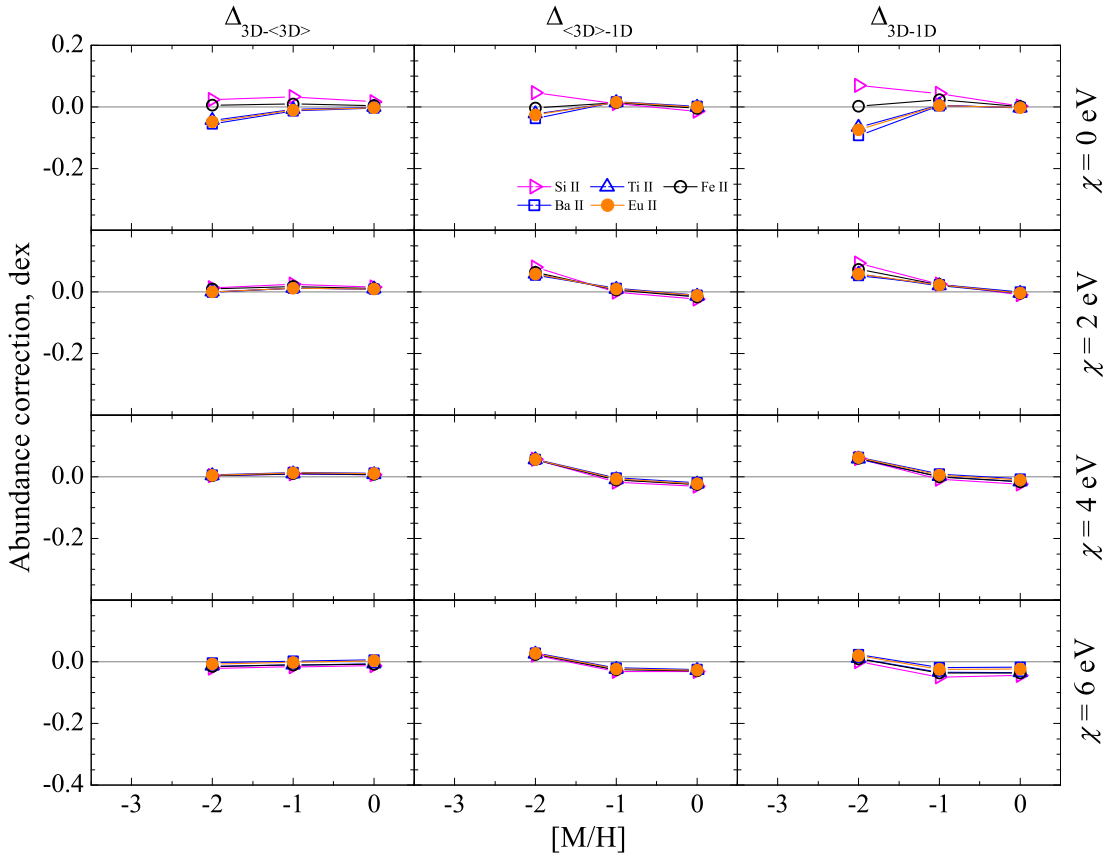

Fig. 2.22. Abundance corrections for lines of ionized atoms plotted versus metallicity at $\lambda = 400$ nm: $\Delta_{\mathrm{3D-\langle 3D\rangle}}$ (left column), $\Delta_{\mathrm{\langle 3D\rangle-1D}}$ (middle column), and $\Delta_{\mathrm{3D-1D}}$ (right column). Corrections in each row were calculated at different excitation potentials, as indicated on the right side of each row.

the size of $\Delta_{\mathrm{3D-\langle 3D\rangle}}$ correction) and the differences between temperature profiles of the $\langle$3D$\rangle$ and 1D models are smallest at all metallicities and change little with [M/H] (Figs. 2.17–2.18). This leads to smaller abundance corrections that are, at the same time, also less sensitive to changes in [M/H] and χ compared to the spectral lines of neutral atoms discussed in Section 2.3.2. Nevertheless, it is interesting to note that in TO stars the $\Delta_{\mathrm{\langle 3D\rangle-1D}}$ correction is larger than the $\Delta_{\mathrm{3D-\langle 3D\rangle}}$ correction, contrary to what was seen in the case of giants.

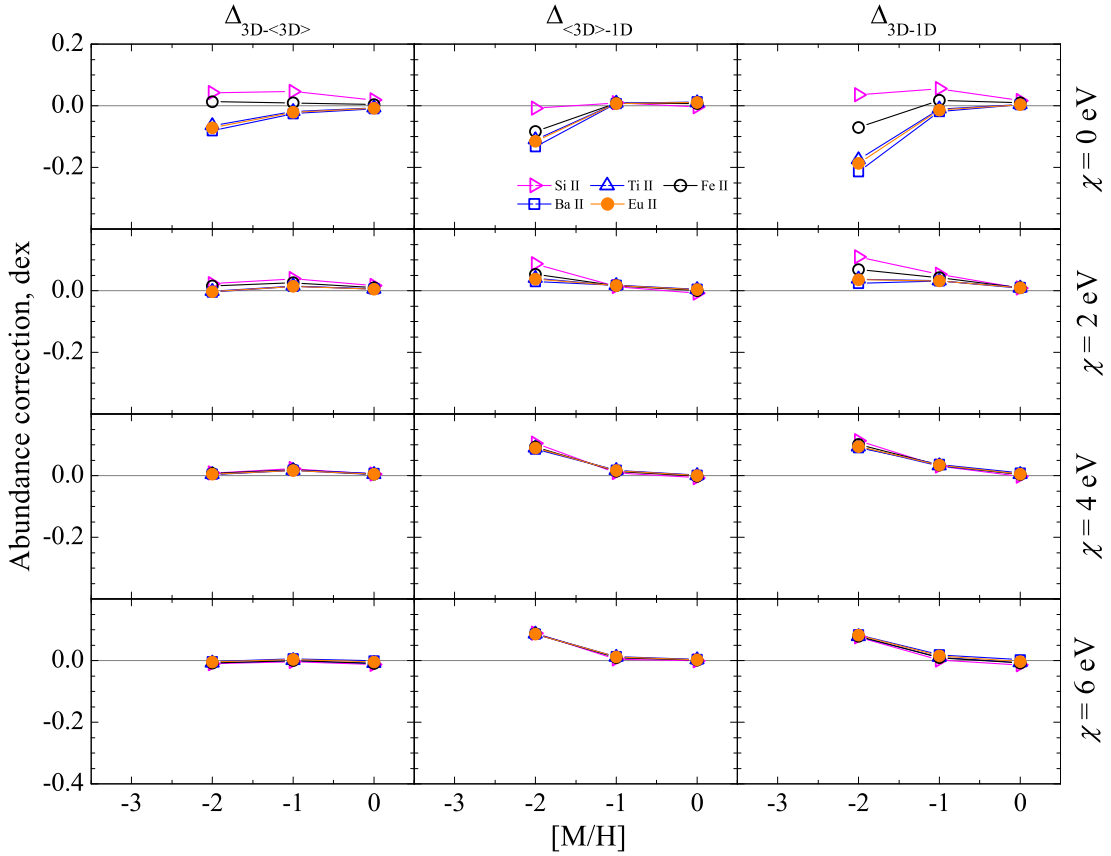

Fig. 2.23. The same as in Fig. 2.22 but at $\lambda = 850\,\mathrm{nm}$.

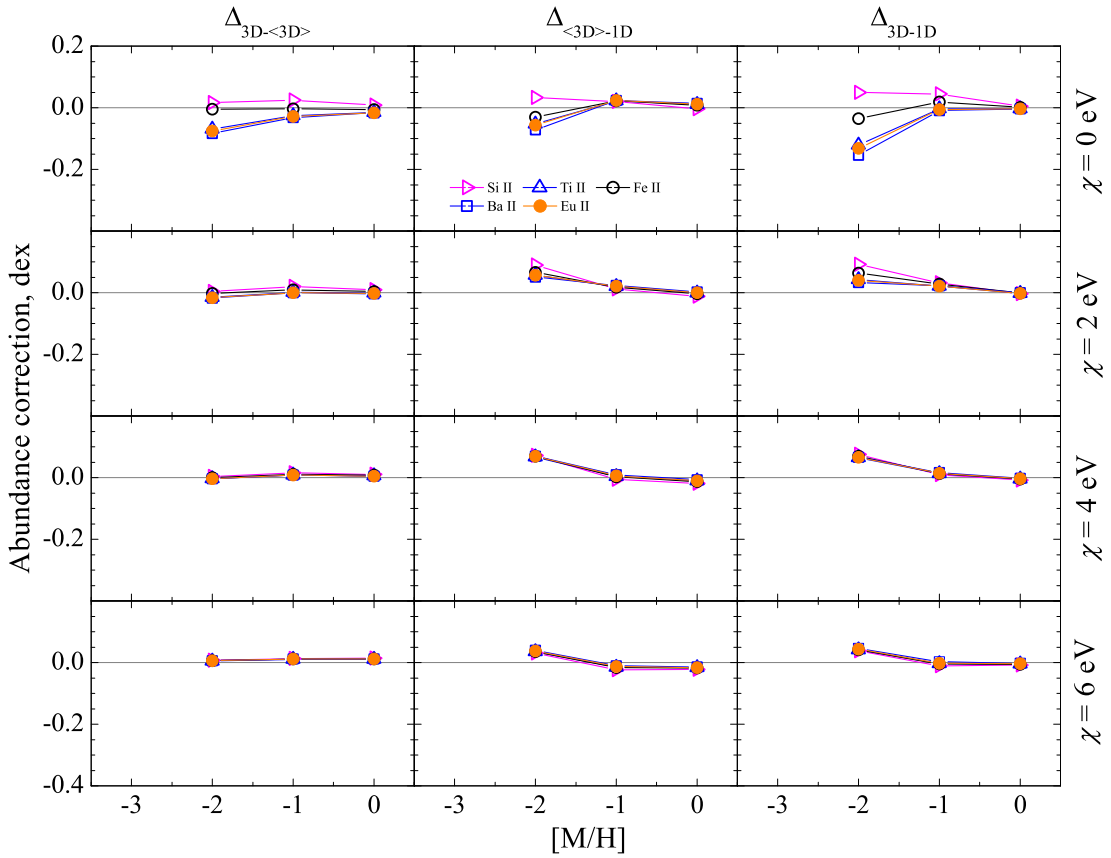

Fig. 2.24. The same as in Fig. 2.22 but at $\lambda = 1600\,\mathrm{nm}$.

Chapter 3

Abundances of chemical elements in Galactic globular cluster stars: effects of convection and non-equilibrium radiation transfer

Galactic globular clusters (GGCs), along with the halo field stars, are amongst the oldest Galactic stellar populations, therefore investigation of their composition may provide important information about the early chemical evolution of the Milky Way. Although the GGC stars display a noticeable scatter in their light element abundances (such as lithium, oxygen, sodium), generally, there is no spread in the abundances of iron-peak and heavier elements larger than the typical measurement errors (≈0.1 dex). The few known exceptions are ω Cen (Suntzeff & Kraft 1996; Norris et al. 1996), M 54 (Carretta et al. 2010b), M 22 (Lehnert et al. 1991; Da Costa et al. 2009; Marino et al. 2011), Terzan 5 (Origlia et al. 2011; Massari et al. 2012), and NGC 1851 (Carretta et al. 2011; Gratton et al. 2012) which do show noticeable star-to-star variations in the iron abundance. However, it is thought that these clusters are not genuine GGCs but, instead, the remnants of dwarf galaxies accreted by the Milky Way or cluster mergers. The first globular cluster where significant start-to-star variation in heavy element abundances was detected was M 15 (Sneden et al. 1997, 2000; Otsuki et al. 2006; Sobeck et al. 2011). Roederer & Sneden (2011) found that the abundances of heavy elements La, Eu, and Ho in 19 red giants of M 92 show a significant star-to-star variation. The latter claim, however, was questioned by Cohen (2011), who found no heavy element abundance spread larger than ~ 0.07 dex in 12 red giants belonging to M 92. The primary formation channels of the s-process elements are low- and intermediate-mass asymptotic giant branch (AGB) stars, thus the information about the vari-

ations in heavy element abundances may shed light on the importance of AGB stars to the chemical evolution of GGCs.

A large amount of work done during the past few decades in the abundance analysis of Galactic globular cluster stars (for a review see, e.g., Gratton et al. 2004; Carretta et al. 2010) led to the discovery of abundance anti-correlations for Na–O (Kraft 1994; Gratton et al. 2001; Carretta et al. 2009a), Mg–Al (see, e.g., Carretta et al. 2009b), Li–Na (Pasquini et al. 2005; Bonifacio et al. 2007), and Li–O abundance correlation (Pasquini et al. 2005; Shen et al. 2010). It is important to note that abundance (anti-)correlations of different light elements are unique to Galactic globular cluster stars and they are not observed in the Galactic field stars of similar metallicity, nor in the open clusters. One exception here is massive open cluster NGC 6791 where Geisler et al. (2012) detected a possible sodium–oxygen abundance anti-correlation, typical for the globular clusters.

The overwhelming majority of such abundance studies focusing on Galactic globular cluster stars was made so far by using classical 1D model atmospheres. On the other hand, results presented in Chapter 2 show that convection plays a significant role in the spectral line formation taking place in stellar atmospheres, and that it should become increasingly important in the low-metallicity stars. This may lead to significant differences in the elemental abundances derived with the 3D hydrodynamical and classical 1D model atmospheres, especially if they are determined using low-excitation spectral lines (e.g., resonance lines). It would be therefore very important to investigate what kind of new information the use of 3D hydrodynamical model atmospheres may bring to the field of abundance studies in Galactic globular cluster stars. At the same time, it is important to understand how the 3D–1D abundance differences compare with those stemming from the effects related with non-equilibrium radiation transfer, e.g., as measured by the NLTE-LTE abundance differences. Both 3D and NLTE effects are expected to be largest at low metallicities, thus the understanding of their relative importance may even lead to new insights in the abundance-related work with Galactic globular cluster stars.

In this Chapter we therefore apply the 3D hydrodynamical model atmospheres in the abundance analysis of chemical elements in stars of two

Galactic globular clusters, 47 Tuc and NGC 6752. Additionally, we also use classical 1D model atmospheres to assess the importance of NLTE effects in the spectral line formation and correct the obtained elemental abundances for their influence. By doing this, we aim to better understand the relative importance of the 3D and NLTE effects in the abundance determinations, as well as to determine 3D+NLTE abundances of a number of chemical elements in the atmospheres of Galactic globular cluster stars. The results of this analysis are presented in Sections 3.1–3.2.

3.1 Abundances of lithium, oxygen, and sodium in Galactic globular cluster 47 Tuc

3.1.1 Observational data

Our study of the turn-off (TO) stars in Galactic globular cluster 47 Tuc was based on the archival spectra obtained with the GIRAFFE spectrograph during the period of August – September 2008, under the programme 081.D-0287(A) (PI: Shen). The same data set was independently analyzed by D'Orazi et al. (2010).

All program stars were observed in the Medusa mode, using three high resolution setups: HR15N (647.0 – 679.0 nm, R = 17 000), HR18 (746.8 – 788.9 nm, R = 18 400) and HR20A (807.3 – 863.2 nm, R = 16 036). In each setup, 114–116 fibers were dedicated to the program stars and 14–16 were used for the sky spectra. There were 12 exposures made using HR15N setup, 10 exposures using HR18, and 6 exposures made using HR20A setup, with each individual exposure lasting 3600 s.

Raw spectra were bias-subtracted, flat-fielded and wavelength calibrated using the command-line version (*EsoRex* v.2.8.9) of GIRAFFE pipeline[1]. All sky spectra from each setup were median-averaged and the obtained master sky spectrum was subtracted from each individual star spectrum using a custom-written IDL routine (there is no sky subtraction routine included in the standard pipeline). After the sky subtraction, individual spectra were corrected for the barycentric radial velocity and co-added to

[1] `http://www.eso.org/sci/software/pipelines/giraffe/giraf-pipe-recipes.html`

increase the signal-to-noise ratio. Signal-to-noise ratio of the final combined spectra was $S/N = 80 - 90$ near the infrared oxygen triplet at 777 nm. In total, spectra of 113 TO stars were extracted during the data reduction procedure. Finally, continuum normalization of the GIRAFFE spectra was performed with the IRAF[2] task *continuum*. An example of the typical spectrum is shown in Fig. 3.3.

3.1.2 Cluster membership

The initial stellar sample selection was based on the color-magnitude diagram of 47 Tuc (Fig. 3.1). We then determined radial velocity of all selected stars to check whether they fulfill kinematic membership requirements. Radial velocity was calculated from the measured central wavelengths of two sodium lines (see Table 3.9), by taking the average value of the two measurements (line profile fit quality was not considered in the radial velocity determination procedure). Radial velocity from both sodium lines agreed to within 1.0 $\mathrm{km\,s^{-1}}$ for 74 stars (66 % of the sample) while the largest difference on velocity values determined from the two lines never exceeded 3.5 $\mathrm{km\,s^{-1}}$.

Average barycentric radial velocity of the 113 sample stars is -17.6 $\mathrm{km\,s^{-1}}$, which agrees well with the value of -18.0 $\mathrm{km\,s^{-1}}$ listed for this cluster in the catalog of Harris (1996). Our obtained radial velocity dispersion is 7.2 $\mathrm{km\,s^{-1}}$, with the lowest and highest velocity values of -32.0 $\mathrm{km\,s^{-1}}$ and $+1.3$ $\mathrm{km\,s^{-1}}$, respectively. We note that the velocity dispersion determined by us is slightly smaller than that obtained by Harris (1996), 11.0 $\mathrm{km\,s^{-1}}$. This, however, should be expected since all stars studied here are located between 4.5′and 11.5′from the cluster center, that is, beyond its half-light radius of 3.17′(Harris 1996). On the contrary, the dispersion value provided in (Harris 1996) was determined using stars located within the half-light radius and therefore, their dispersion value is expected to be larger than that obtained by us. We note that our results agrees well with the radial velocity dispersion determined by Lane et al. (2010) at this radial distance. Our radial velocity results therefore lead us to conclude

[2]IRAF is distributed by the National Optical Astronomy Observatories, which are operated by the Association of Universities for Research in Astronomy, Inc., under cooperative agreement with the National Science Foundation.

that all selected stars were highly probable members of 47 Tuc.

3.1.3 Atmospheric parameters

Effective temperature of the program stars was determined by fitting wings of the observed Hα line profiles with the theoretical Hα profiles (Fuhrmann et al. 1993; Barklem 2008; Cayrel et al. 2011). The fitting was done automatically, by minimizing χ^2 differences between the observed and theoretical line profiles. Theoretical line profiles were computed in LTE with a modified version of the Kurucz's `BALMER` code[3], which allows to use different theories for the self-broadening and Stark broadening of the line profile (see Sbordone et al. 2010). In our case, we used the theory of Barklem et al. (2000a,b) for the self-broadening and that of Stehlé & Hutcheon (1999) for the Stark broadening. A grid of input models for computing synthetic Hα profiles was calculated using `ATLAS9` model atmosphere code (see Sect. 1.1.1 for details). In the fitting procedure, we only used Hα line wings ($\geqq$90% of the normalized flux) which are the most temperature sensitive. We avoided the line core region because it forms in the outer atmospheric layers where deviations from the LTE are possible and, thus, the LTE approach used in the `BALMER` code may not be adequate (Fig. 3.2). We also excluded two spectral lines located on the wings of the Hα profile, to avoid possible systematic shifts in the effective temperature determination. In Fig. 3.2 we show the spectral range around Hα line and highlight the regions that were used in (and excluded from) the fitting procedure.

It is important to note that effective temperatures determined from the Hα line wings are sensitive to surface gravity (see, e.g., Sbordone et al. 2010). On the other hand, surface gravities of the studied TO stars were derived using empirical formula that requires the knowledge of effective temperatures (Sect. 3.1.3.1). Therefore, effective temperatures and gravities of the TO stars studied here were derived using iterative procedure, by adjusting $T_{\rm eff}$ and $\log g$ simultaneously. However, because the program stars occupy very narrow range both in $T_{\rm eff}$ and $\log g$ (see Fig. 3.1, Table 14), the corrections applied during the iterative procedure typically did not exceed $\pm$10 K and $\pm$0.05 dex, respectively.

[3]The original version of the code is available from `http://kurucz.harvard.edu`

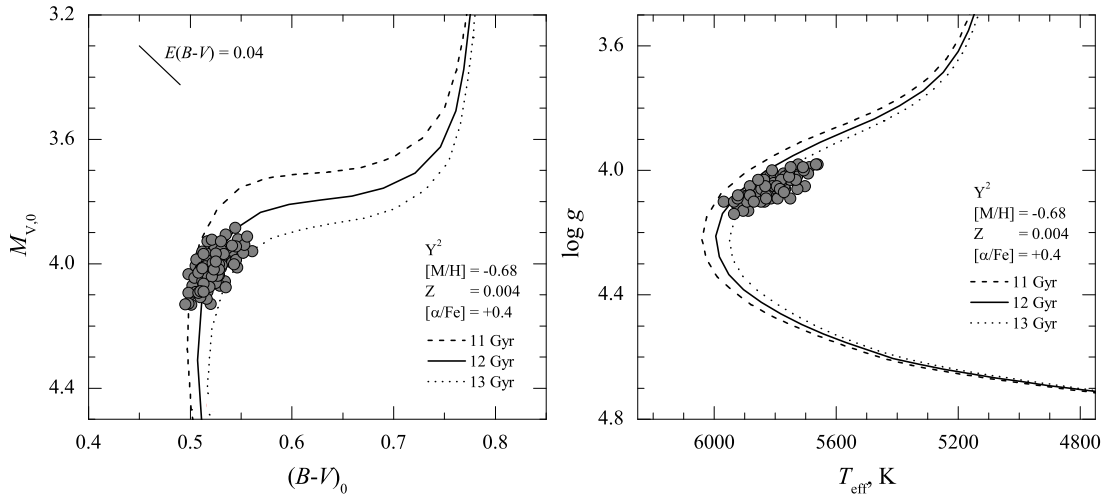

Fig. 3.1. Left: de-reddened $M_{\rm V,0} - (B-V)_0$ CMD of the TO stars studied in 47 Tuc. Lines are Yonsei-Yale (Y^2) isochrones (11, 12, and 13 Gyr), computed assuming $Z = 0.004$ ([M/H] $= -0.68$) and $[\alpha/{\rm Fe}] = +0.4$. Line in the upper left corner shows the reddening vector assuming $A_{\rm V}/E(B-V) = 3.1$. **Right:** HR diagram showing the TO sample stars in 47 Tuc, with the effective temperatures and gravities determined as described in Sect. 3.1.3. Solid lines are Y^2 isochrones.

3.1.3.1 Gravities

Iron ionization equilibrium condition enforcement is one of the most widely used methods to estimate stellar surface gravity. However, we were not able to use this approach due to the small number – only two – of ionized iron lines available in our spectra. Instead, we determined surface gravities using the following relation (with $T_{\rm eff}$ derived from the Hα line wings)

$$\log g \ = \log g_{\odot} + \log(M/M_{\odot}) - \log(L/L_{\odot}) + 4\log(T_{\rm eff}/T_{\rm eff}^{\odot})\,, \qquad (3.1)$$

where $\log g_{\odot} = 4.44$ is the adopted solar surface gravity, $T_{\rm eff}^{\odot} = 5780$ K is the adopted solar effective temperature, M and L are stellar mass and luminosity, respectively (sub-/upper-script $\odot$ denotes solar values). Stellar luminosity of the individual stars was determined from the Yonsei-Yale isochrones (see Sect. 3.1.3.3) using their absolute magnitudes, $M_{\rm V}$, derived from photometry.

In Sect. 3.1.3.2–3.1.3.3 below we outline the procedures used to derive absolute magnitudes and masses, i.e., the quantities needed to obtain surface gravities of the program stars using Eq. 3.1.

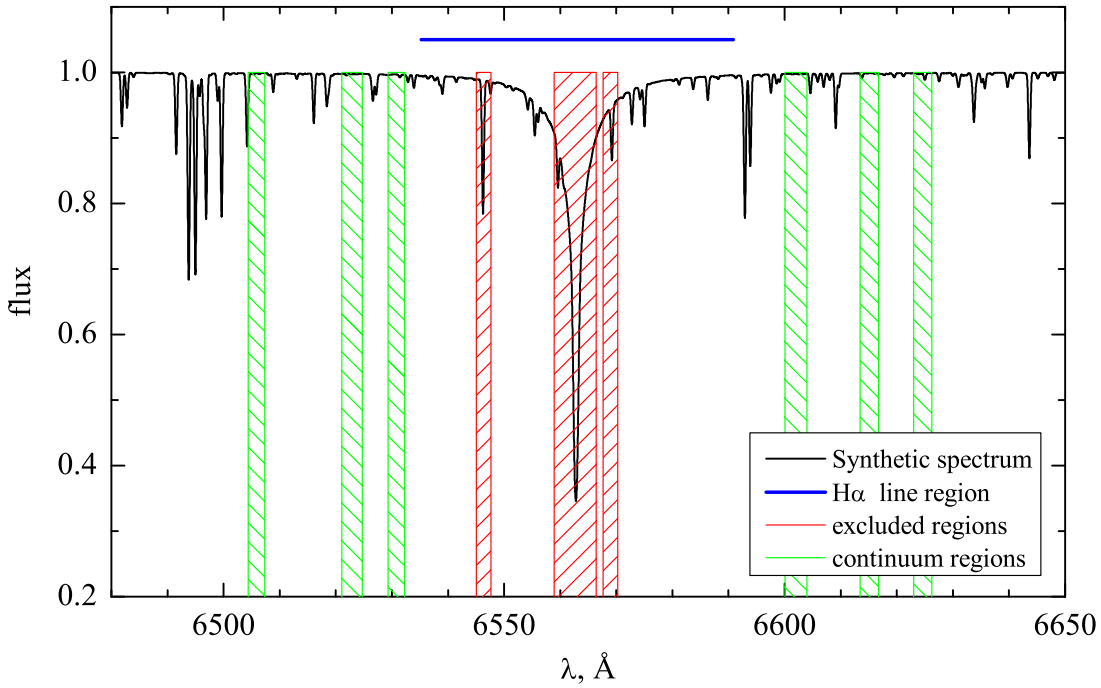

Fig. 3.2. Synthetic spectrum of a TO star in 47 Tuc (star ID 00006129, $T_{\rm eff}$ = 5850 K, $\log g$ = 4.06) showing Hα line region used for the effective temperature determination. Blue bar above the synthetic spectrum indicates the range were fitting of the Hα line wings was done, red dashed rectangles mark the regions excluded from the fitting procedure, while green dashed rectangles highlight the spectral regions used to determine continuum level.

3.1.3.2 Absolute magnitudes M_V

We used BV photometry from Bergbusch & Stetson (2009) to determine M_V of our program stars. During the visual inspection, we have found two possible photometric blends among the sample of program stars, namely stars with designations 00043029 (V_1 = 17.83 mag, V_2 = 18.49 mag, separation = 1.5″) and 00112168 (V_1 = 17.64 mag, V_2 = 18.65 mag, separation = 0.5″). These stars were unresolved or marginally resolved by the GIRAFFE fiber having 1.2″aperture on the sky, which led to incorrect determination of their atmospheric parameters. The two stars were therefore excluded from the abundance analysis.

Due to its high Galactic latitude ($b = -45°$, Harris 1996), 47 Tuc experiences little interstellar reddening: the values found in the literature range from $E(B-V)$ = 0.032 (Schlegel et al. 1998) [4] to $E(B-V)$ = 0.055 (Gratton et al. 1997). Similarly, Grundahl et al. (2002) obtained $E(B-V)$ = 0.04

[4] http://irsa.ipac.caltech.edu/applications/DUST/

Table 3.1. Masses of the program stars derived from the Y^2 isochrones of different age.

t, Gyr	mass range, $M_\odot$	$\langle M \rangle$, $M_\odot$
12	0.84 - 0.86	0.85
13	0.82 - 0.84	0.83

from the Strömgren *uvby* photometry. We note that the reddening uncertainty of $\Delta E(B-V) = 0.02$ would lead to the uncertainty of $\Delta \log g \approx 0.02$ in the surface gravity and therefore would have a minor impact on the effective temperature determination. To correct for the interstellar reddening, we adopted $E(B-V) = 0.04$ from Harris (1996). The distance modulus, $V - M_{\rm V} = 13.37$, was also taken from Harris (1996).

3.1.3.3 Stellar mass

We determined stellar mass from the comparison of the observed color-magnitude diagram (CMD) of 47 Tuc with theoretical isochrones. For this purpose, we used $t = 11$, 12, and 13 Gyr age Yonsei-Yale[5] (Y^2) isochrones, computed for the metallicity of Z = 0.004 and $\alpha-$element enhancement of $[\alpha/{\rm Fe}] = +0.4$. The observed CMD was fitted best with the 12–13 Gyr Y^2 isochrones (Fig. 3.1). The narrow magnitude range occupied by the program stars ($V = 17.23 - 17.51$ mag) translates into a mass interval of $\sim 0.02\,{\rm M}_\odot$ (Table 3.1). Using Eq. 3.1 we find that the uncertainty in stellar mass of $\Delta M = 0.02\,{\rm M}_\odot$ leads to a change in surface gravity of only $\Delta \log g \approx 0.01$ (while keeping the effective temperature and luminosity fixed).

Small mass range of the program stars, together with a small change in the average mass between the 12 and 13 Gyr isochrones, led us to assume a fixed average mass of 0.84 $M_\odot$ for all program stars.

We assumed constant microturbulence velocity value of $\xi_{\rm micro} = 1.0\ {\rm km\,s^{-1}}$ for all stars. In any case, none of the lines analyzed in our study was saturated and therefore the resulting abundances show little sensitivity to the choice of microturbulence velocity (see Table 3.5).

The final stellar sample used in this work contained 110 TO stars. Their atmospheric parameters derived using the prescriptions given in the previ-

[5] `http://www.astro.yale.edu/demarque/yyiso.html`

ous sections are provided in Table 14.

3.1.4 Determination of elemental abundances

Abundances of lithium, oxygen, and sodium in the TO stars of 47 Tuc were determined using slightly different procedures. For sodium and oxygen, the 1D NLTE abundances were derived by best-fitting the observed line profiles with the synthetic spectra computed with the 1D NLTE spectral synthesis code `MULTI`(see Sect. 1.2.1). The obtained 1D NLTE abundances of oxygen and sodium were then corrected for the 3D effects using 3D–1D abundance corrections computed with the 3D hydrodynamical and 1D hydrostatic model atmosphere codes `CO5BOLD` and `LHD`, respectively.

The abundance of lithium, on the other hand, was determined using the equivalent widths of the Li I 670.8 nm resonance doublet measured in the spectra of the program stars. Then, we used the interpolation formula from Sbordone et al. (2010) to directly obtain the 3D NLTE lithium abundance estimate.

In the following sections we will focus on the steps involved in the abundance determinations of all three elements discussed here.

3.1.5 Spectral lines and their atomic parameters

Atomic parameters of spectral lines used in the abundance derivations of lithium, oxygen, and sodium are provided in Table 3.9. Central line of the oxygen triplet (777.416 nm) was significantly affected by telluric emission and thus proved to be unsuitable for the abundance determinations. Oxygen abundance was therefore derived using the two remaining lines of the oxygen triplet located at 777.194 nm and 777.539 nm. Examples of the observed spectral line profiles best-fitted with the synthetic profiles are shown in Fig. 3.3.

3.1.6 3D+NLTE abundances of oxygen and sodium

The 1D NLTE abundances of oxygen and sodium were derived by fitting the observed spectral line profiles with the synthetic spectra computed using the 1D spectral synthesis code `MULTI`. We then corrected the obtained 1D NLTE abundances for the 3D hydrodynamical effects, by using 3D–1D abundance corrections calculated with the 3D hydrodynamical `CO5BOLD` and 1D `LHD`

Table 3.2. Atomic parameters of the spectral lines used in the abundance determinations of lithium, oxygen, and sodium.

Element	λ, nm	χ, eV	log gf[a]	log γ_{rad}[b]	log $\frac{\gamma_4}{N_e}$[c]	log $\frac{\gamma_6}{N_H}$[d]
Li I	670.776	0.000	−0.009	7.56	−5.78	−7.574
Li I	670.791	0.000	−0.309	7.56	−5.78	−7.574
O I	777.194	9.146	0.324	7.52	−5.55	−7.443[e]
O I	777.539	9.146	−0.046	7.52	−5.55	−7.443[e]
Na I	818.326	2.102	0.230	7.52[e]	−5.62[e]	−7.425[e]
Na I	819.482	2.104	0.490	7.52[e]	−5.62[e]	−7.425[e]

[a] Kurucz (1993); [b] natural broadening constant (from Kupka et al. 2000); [c] Stark broadening constant (from Kupka et al. 2000); [d] van der Waals broadening constant (from Kupka et al. 2000); [e] classical value (from Castelli 2005b).

model atmospheres. In the latter two cases, spectral line synthesis was done using the `Linfor3D` package, under the assumption of LTE. A constant microturbulence velocity of $\xi_{\rm micro} = 1.0$ km s^{-1} was assumed for all program stars in the spectral synthesis calculations using the 1D model atmospheres (i.e., `ATLAS9` and `LHD`), irrespective whether it was done with the `MULTI` or `Linfor3D` line synthesis packages. Let us note though, that none of the spectral lines analyzed in this paper were strongly saturated and therefore the resulting abundances were insensitive to the choice of microturbulence velocity (see Table 3.5). The steps involved in the derivation of oxygen and sodium abundances are summarized below.

3.1.6.1 1D NLTE abundances of O and Na

The model atoms of oxygen and sodium described in Sections 1.2.1.1 and 1.2.1.2 were used to derive abundances of the two elements in the TO stars of 47 Tuc. For this purpose, we employed the spectral synthesis code `MULTI` (Carlsson 1986) in its version modified by Korotin et al. (1999), while the abundances were determined by fitting synthetic line profiles to those in the observed spectra of TO stars using χ^2 minimization. Throughout the spectral synthesis computations we used fixed microturbulence $\xi_{\rm micro} = 1.0$ km s^{-1}. Macroturbulence velocity was varied as a free parameter to achieve the best fit to the observed line profiles, with its typical values determined in the range of 1–5 km s^{-1}.

Table 3.3. Parameters of the 3D hydrodynamical CO5BOLD atmosphere models used in this work.

$T_{\rm eff}$, K	$\log g$	[M/H]	Grid dimension, Mm x × y × z	resolution x × y × z
5475	4.0	0	$20.3 \times 20.3 \times 10.6$	$140 \times 140 \times 150$
5533	4.0	−1	$19.9 \times 19.9 \times 10.6$	$140 \times 140 \times 150$
5927	4.0	0	$25.8 \times 25.8 \times 12.5$	$140 \times 140 \times 150$
5850	4.0	−1	$25.8 \times 25.8 \times 12.5$	$140 \times 140 \times 150$

Examples of the observed and best-fitted synthetic 1D NLTE spectral line profiles are shown in Fig. 3.3, while the determined 1D NLTE abundances of O and Na are provided in Table 14 (Appendix A). We note that typical average differences between the abundances of oxygen and sodium obtained using 1D NLTE and LTE spectral line synthesis (estimated by fitting the NLTE and LTE synthetic profiles to the observed line profile) are indeed significant, $\Delta_{\rm 1D\,NLTE-LTE} \approx -0.20$ and ≈ -0.35 dex, respectively.

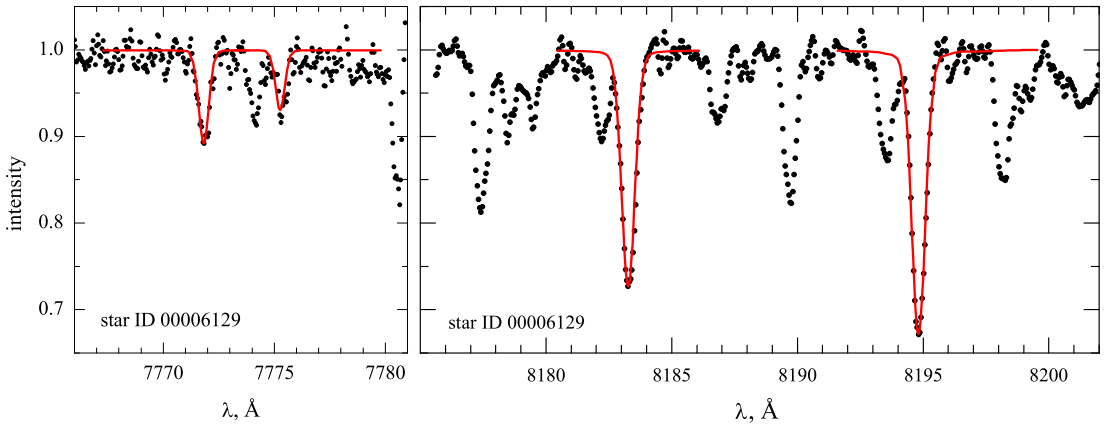

Fig. 3.3. Typical observed GIRAFFE spectrum of TO star in 47 Tuc (star ID 00006129, dotted lines), together with synthetic spectrum (red solid lines) computed using the MULTI code and fitted to the oxygen 777 nm triplet (**left** panel), sodium 818.3 nm, and sodium 819.5 nm (both in the **right** panel) lines.

3.1.6.2 3D–1D abundance corrections for O and Na

Convection has a significant impact on the spectral line formation in the atmospheres of cool stars. A number of recent studies have shown that treating convection in one-dimensional hydrostatic model atmospheres with the mixing-length theory may lead to significant differences in the abundances of chemical elements with respect to those determined using 3D hydrodynamical model atmospheres (a non-exhaustive list includes Asplund et al.

1999; Collet et al. 2007; Caffau & Ludwig 2007; González Hernández et al. 2008; Bonifacio et al. 2010; Dobrovolskas et al. 2012). The role of convection becomes especially important in the atmospheres of metal-poor stars ([Fe/H] < -2), where horizontal fluctuations of thermodynamic quantities and changes in the vertical temperature and velocity profiles may lead to significant differences in the predicted spectral line strengths. We therefore used 3D hydrodynamic CO^{5}BOLD stellar model atmospheres (Freytag et al. 2012) to assess the impact of such effects on the spectral line formation in the atmospheres of our program stars.

The CO^{5}BOLD models used for this purpose were taken from the CIFIST 3D hydrodynamical model atmosphere grid (Ludwig et al. 2009). Since the model spacing in the $T_{\rm eff} - \log g - [{\rm M/H}]$ plane is rather coarse, there are no CIFIST models with the atmospheric parameters exactly corresponding to those of the program stars. We therefore used four CO^{5}BOLD models bracketing the parameters of TO stars with their $T_{\rm eff}$ and [M/H]. The desired quantities (e.g., line strengths) were computed using each of the four models and then interpolated to the effective temperature and metallicity of a given TO star. Atmospheric parameters of the 3D hydrodynamical models are provided in Table 3.3. Each simulation run covered about ≈ 7.5 days in stellar time, or $\approx$19 convective turnover times as measured by the Brunt-Vaisälä timescale (see Kučinskas et al. 2013, for the definition; note that the advection time scale was always significantly shorter). Monochromatic opacities used in the model calculations were taken from the MARCS stellar atmosphere package (Gustafsson et al. 2008) and were grouped into several opacity bins using the opacity binning technique (Nordlund 1982; Ludwig 1992; Ludwig et al. 1994; Vögler et al. 2004): five opacity bins were used for the [M/H] = 0.0 models and six bins for the [M/H] = −1.0 models. The models were computed using solar-scaled elemental abundances from Asplund et al. (2005), by applying a constant enhancement in the alpha-element abundances of $[\alpha/{\rm Fe}] = +0.4$ for the models at [M/H] = −1.0. All model simulations were performed under the assumption of LTE, with scattering treated as true absorption (for more details on the model calculations see Ludwig et al. 2009).

To perform spectral line synthesis calculations, from the four 3D hy-

drodynamical model runs we selected four smaller subsamples of 20 model structures (further called snapshots; 18 snapshots were selected in the case of model at $T_{\rm eff} = 5927$ K, $\log g = 4.0$, [M/H] = 0.). The selected snapshots were spaced nearly equidistantly in time and spanned the entire length of each simulation run. Each snapshot ensemble was selected in such a way as to ensure that its most important statistical properties (the average effective temperature, its standard deviation, mean velocity at the optical depth unity, mean velocity and residual mass flux profiles) would match those of the entire simulation run as closely as possible. Time separation between the individual snapshots in the 20 snapshot ensemble was ≈ 0.4 days (≈ 1 convective turnover time) which allows us to consider them statistically independent.

As in our previous work (e.g., Kučinskas et al. 2013; Dobrovolskas et al. 2013), the influence of convection on the spectral line formation was assessed with the help of 3D–1D abundance corrections (see Section 1.3 for details). To remind, the 3D–1D abundance correction, $\Delta_{\rm 3D-1D}$, is defined as a difference between the abundance A(X) of chemical element X derived at the observed equivalent width of a given spectral line using 3D and 1D model atmospheres, $\Delta_{\rm 3D-1D} = A({\rm X})_{\rm 3D} - A({\rm X})_{\rm 1D}$. We also made use of two additional abundance corrections, $\Delta_{\rm 3D-\langle 3D\rangle} \equiv A({\rm X})_{\rm 3D} - A({\rm X})_{\langle 3D\rangle}$, and $\Delta_{\langle 3D\rangle-1D} \equiv A({\rm X})_{\langle 3D\rangle} - A({\rm X})_{\rm 1D}$. These corrections utilize average $\langle$3D$\rangle$ models which were computed by horizontally averaging all atmospheric structures in the twenty 3D model snapshot ensemble (the fourth power of temperature was averaged on surfaces of equal optical depth). Obviously, the average $\langle$3D$\rangle$ models do not contain information about the horizontal fluctuations of dynamical and thermodynamic quantities. Therefore, the first of the two corrections, $\Delta_{\rm 3D-\langle 3D\rangle}$, allows to assess the importance of the horizontal fluctuations, while the other, $\Delta_{\langle 3D\rangle-1D}$, the role of differences between the temperature profiles of the average $\langle$3D$\rangle$ and 1D models. The total 3D–1D abundance correction is indeed the sum of the two constituents, $\Delta_{\rm 3D-1D} \equiv \Delta_{\rm 3D-\langle 3D\rangle} + \Delta_{\langle 3D\rangle-1D}$.

To compute the abundance corrections, 3D hydrodynamical, average $\langle$3D$\rangle$, and 1D `LHD` model atmospheres were used to synthesize spectral lines with the equivalent widths, EW, equal to those measured in the given pro-

gram star, and to obtain the 3D, ⟨3D⟩, and 1D abundances of a given chemical element (note that this approach differs from that applied in Chapter 2 and in Dobrovolskas et al. 2013; Kučinskas et al. 2013, where only very weak lines were used to compute the abundance corrections). The resulting $\Delta_{\mathrm{3D-\langle 3D\rangle}}$, $\Delta_{\mathrm{\langle 3D\rangle-1D}}$, and $\Delta_{\mathrm{3D-1D}}$ abundance corrections were then interpolated to the effective temperature of the given program star and the metallicity of 47 Tuc (the latter was kept fixed at [Fe/H] = −0.7). We note that CO^{5}BOLD and LHD model atmospheres were computed using identical atmospheric parameters, equation of state, and opacities, in order to minimize the possible sources of discrepancies in their predicted line strengths. This allowed us to focus solely on the differences arising due to different treatment of convection in the 3D hydrodynamical and 1D hydrostatic model atmospheres.

We thus computed 3D–1D abundance corrections for oxygen and sodium, for every object in the sample of 110 TO stars studied here and for every spectral line used in the abundance determination, using the line equivalent widths obtained during the 1D NLTE abundance analysis. The 1D NLTE abundances were then corrected for the 3D effects, by adding the average 3D–1D abundance correction obtained for a given element in a given star to its average 1D NLTE abundance. Abundances obtained using such procedure will be further referred to as 3D+NLTE abundances, in order to make a clear distinction from the 3D NLTE abundances of lithium which were obtained based on full 3D NLTE spectral line synthesis calculations. The obtained 3D+NLTE abundances of oxygen and sodium are provided in Table 14 (Appendix A).

The information about the obtained abundance corrections is summarized in Table 3.4, where we provide $\Delta_{\mathrm{3D-\langle 3D\rangle}}$, $\Delta_{\mathrm{\langle 3D\rangle-1D}}$, and $\Delta_{\mathrm{3D-1D}}$ abundance corrections for the spectral lines of oxygen and sodium used in our study. In each case, we list the average, minimum and maximum values of the correction computed from the ensemble of individual corrections corresponding to each of 110 TO stars in 47 Tuc. Obviously, the 3D–1D abundance corrections are small and typically do not exceed $\Delta_{\mathrm{3D-1D}} \approx 0.07$ dex.

Finally, we would like to warn the reader that the procedure used by us to obtain 3D+NLTE abundances should be utilized with caution. The

Table 3.4. Average, minimum, and maximum abundance corrections for the spectral lines of Li, O, and Na in the sample of 110 TO stars in 47 Tuc.

species	λ, nm	$\Delta_{\text{3D}-\text{<3D>}}$			$\Delta_{\text{<3D>}-\text{1D}}$			$\Delta_{\text{3D}-\text{1D}}$		
		aver	min	max	aver	min	max	aver	min	max
O I	777.2	0.000	−0.028	+0.015	+0.067	+0.049	+0.074	+0.067	+0.021	+0.089
O I	777.5	−0.012	−0.033	+0.007	+0.061	+0.046	+0.072	+0.049	+0.013	+0.079
Na I	818.3	−0.063	−0.098	−0.043	+0.066	+0.044	+0.093	+0.003	−0.037	+0.031
Na I	819.5	−0.056	−0.076	−0.041	+0.075	+0.048	+0.102	+0.019	−0.013	+0.042

reason for this is that population numbers of atomic levels in NLTE depend very sensitively on temperature but this is not taken into account by applying 3D–1D LTE corrections to 1D NLTE abundances. Our test simulations utilizing full 3D NLTE radiation transfer and the 3D hydrodynamical models used above show that in the case of lithium the 3D+NLTE approach may in fact be justifiable at solar metallicity. However, at [M/H] = −1.0 (and below) the full $\Delta_{\mathrm{3D\,NLTE–1D\ LTE}}$ abundance correction becomes significantly different from the combined $\Delta_{\mathrm{1D\,NLTE–LTE}} + \Delta_{\mathrm{3D–1D\ LTE}}$ correction. Such deviation occurs because the lithium line formation extends rather far into the outer atmosphere where the amplitude of horizontal temperature fluctuations (and thus, its influence on the atomic level populations) is largest. Moreover, weaker line blanketing in the metal-poor stellar atmospheres leads to more efficient photoionization. All this may result in significantly different population numbers in 3D NLTE and 1D NLTE cases. Clearly, these differences can not be accounted for in the 3D+NLTE approach, by applying 3D–1D LTE corrections to the 1D NLTE abundances. In this respect, the situation is somewhat safer with oxygen and sodium since in these two cases the contribution of horizontal temperature fluctuations and differences between the average 3D and 1D temperature profiles to the total 3D–1D abundance correction are about equal but of opposite sign, which leads to smaller total abundance correction, $\Delta_{\mathrm{3D–1D\ LTE}}$ (see Table 3.4). It is nevertheless obvious that full 3D NLTE spectral synthesis should be utilized whenever such possibility is available; hopefully, this may gradually become more accessible with the implementation of NLTE methodology into the 3D spectral synthesis codes (Lind et al. 2013; Prakapavičius et al. 2013; Holzreuter & Solanki 2013).

3.1.7 3D NLTE abundances of lithium

As a first step in the abundance analysis of lithium, we determined the equivalent width of the lithium 670.8 nm resonance doublet by fitting the observed spectrum of a given star with a synthetic line profile computed using 1D NLTE spectral synthesis package `SYNTHE` (Kurucz 2005; Sbordone 2005). We then used the obtained *EW*s to determine the 3D NLTE lithium abundance by using analytical formula (B.1) from Sbordone et al. (2010).

Table 3.5. Li, O, and Na abundance sensitivity to changes in the atmospheric parameters.

Element	$\Delta T_{\rm eff}$ ±100 K	$\Delta \log g$ ±0.1 dex	$\Delta \xi_{\rm micro}$ ±0.2 km s^{-1}	ΔA dex
Li I	+0.09	−0.01	0.00	0.09
	−0.08	+0.01	0.00	0.08
O I	−0.08	+0.03	−0.01	0.09
	+0.09	−0.03	+0.01	0.10
Na I	+0.06	−0.05	−0.03	0.08
	−0.07	+0.04	+0.02	0.08

This interpolation formula was obtained by utilizing the results of 3D NLTE spectral synthesis computations done for a range of lithium abundances and by covering the effective temperatures and surface gravities typical to those of the main sequence stars. The fitting formula of Sbordone et al. (2010) was derived using models in the metallicity range of [Fe/H] = −1.0 to –3.0, thus for the stars in 47 Tuc we were extrapolating to slightly higher metallicities.

We were able to detect the lithium resonance doublet in 94 TO stars. The derived 3D NLTE lithium abundances span the range of $1.24 < A(\mathrm{Li}) < 2.21$ dex, with the average value of $\langle A(\mathrm{Li})\rangle = 1.78 \pm 0.18$ (the error is standard deviation of the lithium abundance in the ensemble of 94 TO stars). The obtained lithium abundances are provided in Table 14 (Appendix A).

3.1.8 Abundances sensitivity to changes in the atmospheric parameters

The influence of the uncertainties in the atmospheric parameters to the abundance determinations of Li, O and Na was assessed by varying atmospheric parameters within their typical uncertainty ranges: effective temperature by ±100 K, surface gravity by ±0.1 dex, and microturbulence velocity by ±0.2 km s^{-1}. We took the average atmospheric parameters and spectral line strengths measured in the TO stars of 47 Tuc as reference values for this test. The corresponding changes in the elemental abundances are provided in Table 3.5. The numbers in the case of lithium were obtained by varying the corresponding atmospheric parameters in the formula of Sbordone et al. (2010), while for oxygen and sodium sensitivity determination was made using `ATLAS9` model atmospheres and 1D NLTE line synthesis with `MULTI`.

The last column contains all three abundance changes added in quadrature and thus may serve as a measure of combined sensitivity to changes in the uncertainty all atmospheric parameters. The results show that the uncertainty in the effective temperature has by far the largest impact on the abundance determination of all three elements investigated in this work.

3.1.9 Sensitivity of sodium abundances to blending with CN lines

Spectral region around the sodium lines used in this study contains several weak CN lines which may blend with the lines of sodium. Since the TO stars in 47 Tuc show large spread in carbon and nitrogen abundances (Cannon et al. 1998; Carretta et al. 2005), CN blends with sodium lines may introduce systematic changes in the derived sodium abundances, and may thus distort the resulting sodium abundance correlations. We therefore deemed it necessary to test the impact of CN spectral lines on the sodium abundance determination.

To this end, we synthesized a number of synthetic spectra with the Linux version (Sbordone 2005) of the spectral synthesis code `SYNTHE` (Kurucz 2005), by using a number of `ATLAS9` model atmospheres that corresponded to the average and extreme values of atmospheric parameters of the studied TO stars in 47 Tuc. The spectra were synthesized using different combinations of C and N abundances representing the most CN-rich and CN-poor stars, as well as those with the average CN abundance (see Table 3.6). For reference, we also computed a synthetic spectrum neglecting CN lines. Equivalent widths of synthetic sodium lines were then measured in each synthetic spectrum and sodium abundances were determined using the measured equivalent widths, utilizing for this purpose the Linux version of the `WIDTH` code (Kurucz 1993; Kurucz 2005; Castelli 2005). We found that difference in the sodium abundance obtained from the spectrum without CN lines and that computed with the nitrogen enhancement of [N/Fe] = +1.25 dex is ≈ 0.02 dex for the sodium 819 nm line and < 0.01 dex for the 818 nm line. We therefore conclude that the impact of CN line blending on the sodium abundance derivations may be safely ignored.

Table 3.6. Combinations of carbon and nitrogen abundances used to estimate the impact of blending with CN lines on the determined sodium abundances.

[C/Fe]	[N/Fe]
−0.10	−0.35
−0.25	+0.50
−0.45	+1.25

3.1.10 Discussion

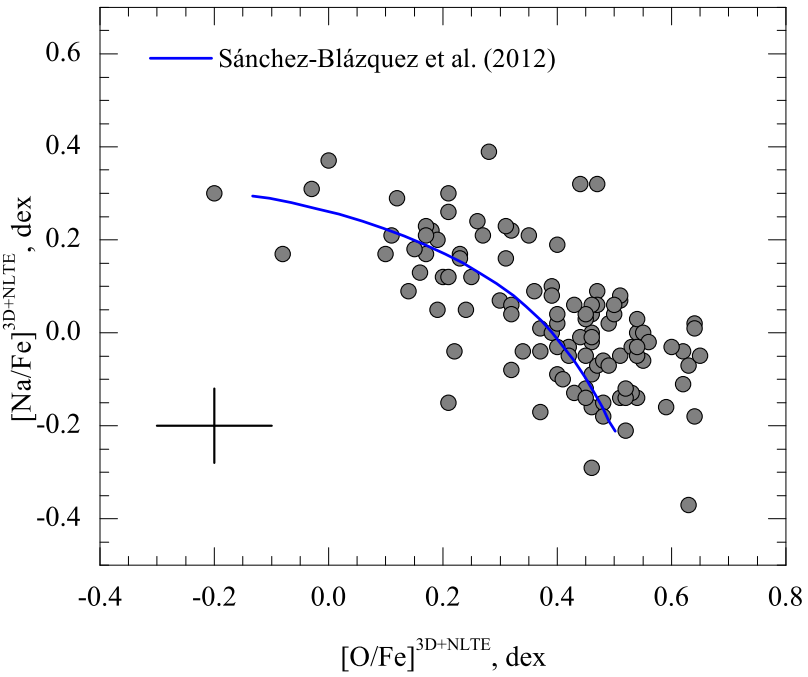

Fig. 3.4. Abundances of oxygen and sodium in the TO stars of 47 Tuc derived in this work by taking into account 3D hydrodynamical and NLTE effects. Typical error bars are shown in the bottom-left corner of the panel. Blue solid line shows chemical evolution model of 47 Tuc from Sánchez-Blázquez et al. (2012)

In Fig. 3.4 we plot the determined abundances of oxygen against those of sodium. Our results confirm the presence of the Na–O abundance anti-correlation. This finding is in good agreement with the results of D'Orazi et al. (2010) although we obtain a slightly smaller spread in the sodium abundance (Fig. 3.4). It is interesting to note that the observed Na–O abundance anti-correlation agrees surprisingly well with the model predictions of Sánchez-Blázquez et al. (2012).

We find that the effects of convection play a minor role in the spectral line formation of O and Na taking place in the atmospheres of TO stars in

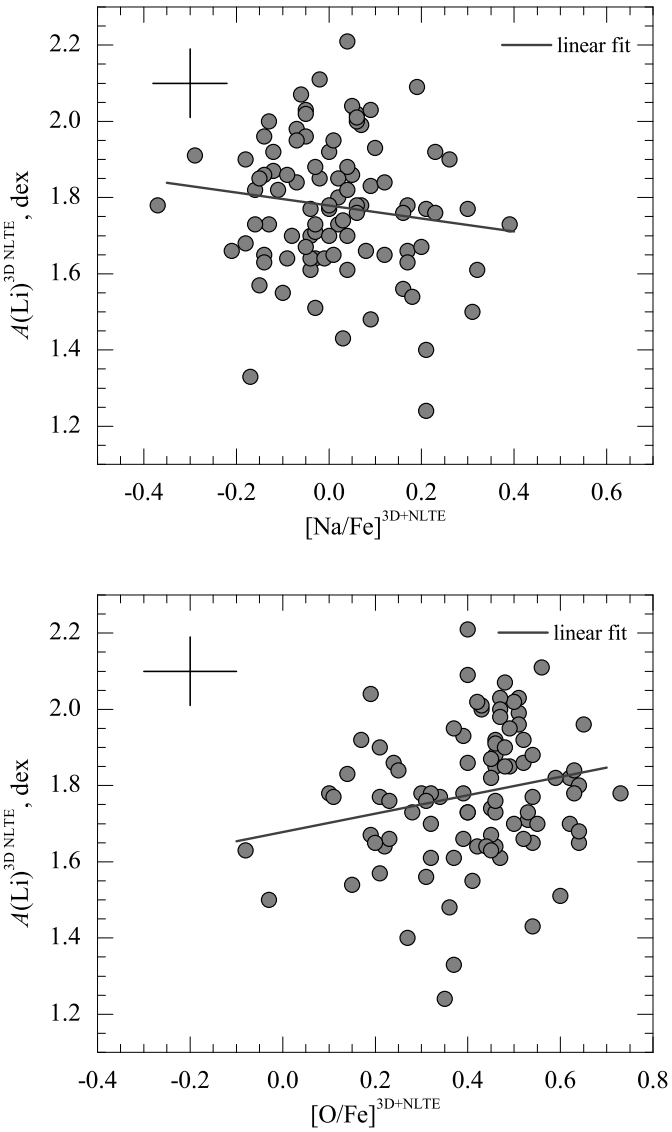

Fig. 3.5. Lithium–sodium (top panel) and lithium–oxygen (bottom panel) abundances determined in this work. Typical error bars are shown in the top left-corner of the panels. Unweighted linear fits to the data are shown by solid lines.

47 Tuc, leading to relatively small $\Delta_{\mathrm{3D-1D}}$ abundance corrections, $-0.04 \cdots +$ 0.04 dex for sodium and $+0.01 \cdots +0.09$ dex for oxygen. On the other hand, deviations from LTE are substantial: on average, the NLTE abundance correction is as large as -0.35 dex for sodium and -0.20 dex for oxygen.

Although less convincingly, our results also hint towards the existence of Li–O correlation (Fig. 3.5). This is supported by the results of Kendall's tau (τ) test (Press et al. 1992) which detects the existence of Li–O correlation at 95 % probability level, with $\tau = 0.14$. Although one should note that the data scatter is large, this result is nevertheless robust even if the two

Table 3.7. Average lithium abundance and its spread in Galactic globular clusters and the open cluster NGC 2243.

Cluster	N	[Fe/H]	$\langle A(\mathrm{Li})\rangle$	$A(Li)_{min}$	$A(Li)_{max}$	Reference
M 4	73	−1.33	2.14	1.82	2.40	Monaco et al. (2012)
M 92	6	−2.31	2.35	2.04	2.55	Bonifacio (2002)
NGC 6397	79	−2.02	2.30	2.01	2.52	González Hernández et al. (2009)
NGC 6752	102	−1.42	2.29	1.84	2.61	Shen et al. (2010)
ω Cen	52	−1.71	2.19	1.76	2.49	Monaco et al. (2010)
47 Tuc	94	−0.76	1.78	1.24	2.21	This paper
NGC 2243	20	−0.55	2.61	2.33	2.85	François et al. (2013)

stars with the lowest oxygen abundance are excluded from the test. On the other hand, evidence for the Li–Na anti-correlation is weak: in this case, Kendall's tau test yields the detection at the level of only 58 % ($\tau = -0.06$).

Lithium, along with hydrogen and helium, was synthesized during the Big-Bang nucleosynthesis what makes it particularly important element because of its relevance to cosmology. On the assumption that its abundance in the oldest stars has not been altered since the star formation, the knowledge of the lithium abundance may allow to test the models of primordial nucleosynthesis. In the warm metal-poor stars the lithium abundance is roughly constant, $A(\mathrm{Li}) = 2.1 - 2.3$, what is known as *Spite Plateau* (Spite & Spite 1982a,b; Sbordone et al. 2010). Primordial lithium abundance based on the WMAP measurements of the baryonic density (Spergel et al. 2003; Komatsu et al. 2011) and Standard Big Bang Nucleosynthesis (SBBN) is predicted to be $A(\mathrm{Li}) = 2.7$ (Cyburt et al. 2008). The value derived from the measurements of Planck satellite (Planck Collaboration et al. 2013) is the same within errors (Coc et al. 2013). It is still not clear yet why the *Spite Plateau* is ≈ 3 times lower than the predicted primordial abundance (see Sbordone et al. 2010, for a discussion of possible explanations).

The spread in the lithium abundances derived in our study in the TO stars in 47 Tuc appears to be larger and the mean abundance lower than what is found in other globular clusters: if the exceptionally Li-rich stars Cl* NGC 6397 K 1657 (Koch et al. 2011) and Cl* M 4 M 37934 (Monaco et al. 2012) are excluded, other globulars show a rather uniform lithium abundance. In Table 3.7 we have assembled literature data of the mean $A(\mathrm{Li})$ abundance and the range in $A(\mathrm{Li})$ variation for the handful of globular clusters, and added to these the metal-poor open cluster NGC 2243 (François et al. 2013). When confronted with several analyses of the same cluster in the literature we chose, when available, the ones with the 3D NLTE lithium abundances obtained using the fitting formula of Sbordone et al. (2010) were used, to be directly comparable to the present results. For M 92 we chose the reanalysis of Bonifacio (2002) rather than the original analysis of Boesgaard et al. (1998), though this choice would bear no consequences to our discussion. The globular cluster NGC 6752 (Shen et al. 2010) is the one with the larger range in Li abundances, after 47 Tuc, and has a higher

mean A(Li) abundance, too. ω Cen is not an ordinary globular cluster but rather the stripped core of a satellite galaxy, and is the only cluster in Table 3.7 that shows a large spread in [Fe/H]. In Table 3.7 and Fig. 3.6 we adopted [Fe/H] = −1.71 as a median of the metallicities in the Monaco et al. (2010) sample. In Fig. 3.6 we have also plotted the values for old (4.35 Gyr, Kaluzny et al. 2006), metal-poor ([Fe/H]=–0.54, François et al. 2013) open cluster NGC 2243, from the analysis of François et al. (2013). We also complemented the plot with the data for a number of open clusters having different ages (taken from Sestito & Randich 2005), and Galactic field stars from Lambert & Reddy (2004).

There are several facts that are evident from the inspection of Fig. 3.6:

- all globular clusters display a dispersion in lithium abundances, probably due to the chemical evolution of the cluster itself, as suggested by the Li–O correlation and, possibly, Li–Na anti-correlation;
- this dispersion is small with respect to the "gap" between the mean cluster abundance and the primordial lithium abundance predicted by SBBN and WMAP measurements of the baryonic density;
- the mean lithium abundance of the metal-poor globular clusters (i.e., all except 47 Tuc) traces well the *Spite Plateau*;
- 47 Tuc has lower mean lithium abundance and higher dispersion than other globular clusters;
- the mean lithium abundance and its dispersion in 47 Tuc are compatible with lithium abundances observed in the field stars at the same metallicity and older than 12 Gyr;
- metal poor, old open cluster NGC 2243, with a metallicity close to that of 47 Tuc, has higher mean Li abundance;
- field stars younger than 2 Gyr have, on average, higher lithium abundances than those that are older than 12 Gyr;
- at approximately solar metallicity, there is a clear tendency for open clusters to have lower lithium abundance with increasing age.

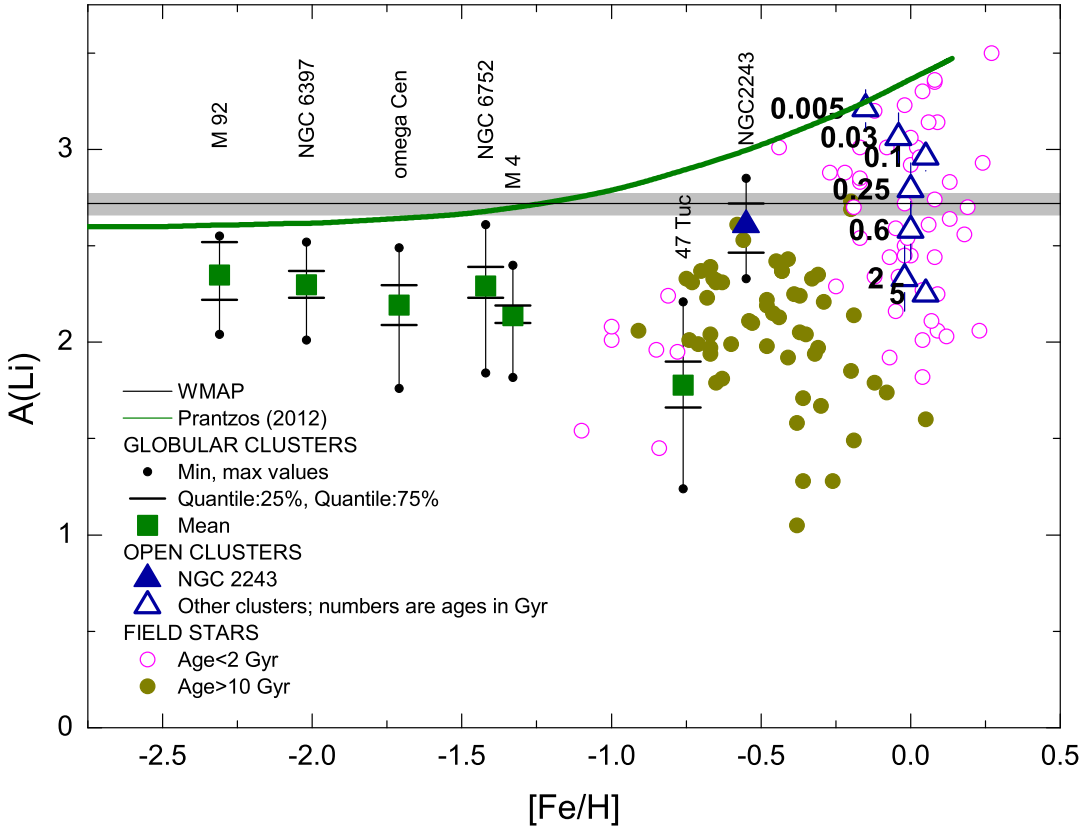

Fig. 3.6. Lithium abundance in Galactic globular and open clusters, and field stars, plotted versus metallicity. We show the mean (filled green rectangles), minimum, and maximum values (small black dots connected by vertical solid lines), and 25% and 75% quantiles (black horizontal bars) of lithium abundances as derived in unevolved stars of Galactic globular clusters M 92, NGC 6397, ω Cen, NGC 6752, and 47 Tuc, and the old, metal-poor open cluster NGC 2243 (filled blue triangle, $\sim$ 4.4 Gyr, Kaluzny et al. 2006, see also Table 3.7 for details). The data for open clusters (open blue rectangles) were taken from Sestito & Randich (2005), with each datapoint typically representing averages for several open clusters in a given age bin (ages are indicated by numbers next to the symbols, in Gyr, error bars in this case mark 1σ spread in lithium abundances). Data for the Galactic field stars (filled and open circles) were taken from Lambert & Reddy (2004) and are shown for two age sub-groups: stars that are older than 10 Gyr (filled circles) and stars that are younger than 2 Gyr (open circles). Solid green line shows theoretically predicted evolution of Galactic lithium abundance from Prantzos (2012).

These facts may be understood in terms of the following scenario. The stars in the globular clusters all form with the same Li abundance. This abundance may be slightly altered in the course of the star's life (see González Hernández et al. 2009). On top of this effect, one observes Li differences amongst the stars of first and successive generations, due to the effect of pollution of the cluster medium by the first generation stars (this would explain the Li–O correlation). All these effects are of second order, so that the mean cluster abundance is close to the original initial abundance, which is confirmed by nearly uniform Li abundance in all metal-poor clusters seen in Fig. 3.6. In the most metal-rich clusters, like 47 Tuc, the convective envelope is deeper and photospheric material is brought down to layers where the temperature is sufficient to destroy lithium. For this reason, the mean Li abundance of 47 Tuc is lower and its Li dispersion is larger than in the other globular clusters. The old metal-rich field stars follow the same fate, and this is why, on average, they have a lower Li abundance. As time passes, Li is produced in the Galaxy so that the stars and clusters formed more recently are formed with higher Li abundance. The open cluster NGC 2243 clearly shows this: in spite of the fact that its metallicity is only slightly different from that of 47 Tuc, its mean Li abundance is clearly higher. Importantly, the highest Li abundance found in 47 Tuc is lower than the lowest abundance observed in NGC 2243 (excluding the Li-dip stars, of course). A prediction of this simplistic qualitative scenario, would be that, by analogy to what is observed in 47 Tuc, when NGC 2243 will reach the age of 12 Gyr it should have a mean Li abundance by 0.5 dex lower than its present-day value.

Chemical evolution of lithium in the Galaxy is difficult to model, due to the existence of several sources that can, potentially, produce lithium besides the Big Bang Nucleosynthesis (see Matteucci 2010, for a review). Current models assume that the Galaxy started with the WMAP+SBBN lithium abundance, thus the evolution curve of lithium abundance stays well above the *Spite Plateau* (Matteucci 2010; Prantzos 2012). It has already been pointed out by François et al. (2013) that the lithium abundance predicted by the model of Prantzos (2012) is higher, by a factor of 2, than the highest Li abundance observed in NGC 2243. We may add here one further

observation that while 47 Tuc lies at a metallicity at which, according to the model, Galactic cosmic rays are already contributing as much as 20% of the primordial lithium abundance, it lies well below the other globular clusters. It should, however, be borne in mind that although 47 Tuc is as metal-rich as many disc stars, it is much older, therefore it could not have benefited of the lithium produced by cosmic ray spallation. Similarly, it may be simply because of its rather old age that the lithium abundance in NGC 2243 is significantly lower than that predicted by the models of Galactic chemical evolution.

The scenario we have described assumes that the initial lithium abundance in Galactic globular clusters and metal-poor field stars was close to the value of the *Spite Plateau*. While it could be also possible to conceive that it had the initial WMAP+SBBN value instead, a very contrived mechanism for the Li-depletion must be sought for in order to explain, simultaneously: *(i)* the *Spite Plateau*, *(ii)* the lower abundance of 47 Tuc, and *(iii)* the depletion of lithium, with respect to the predictions of chemical evolution models, in NGC 2243.

3.2 Abundances of lithium, sodium, and barium in NGC 6752

3.2.1 Observational data

In our abundance analysis of lithium, sodium, and oxygen in the Galactic globular cluster NGC 6752 we used reduced (bias subtracted, flat-fielded, and wavelength calibrated) spectra of 20 red giants available from the ESO Science Archive[6]. The high resolution ($R = 60\,000$) spectral material was acquired with the UVES spectrograph at the VLT-UT2 (programme 65.L–0165(A), PI: F. Grundahl). Spectra obtained during the three individual exposures were co-added to achieve the average signal-to-noise ratio $S/N \approx 130$ at ~ 600.0 nm. Observations were taken in the standard Dic 346+580 nm setting which covered the 670.8 nm resonance Li I doublet and 568.3, 568.8, 615.4, and 616.1 nm lines of Na I but did not cover the

[6] `http://archive.eso.org/eso/eso_archive_adp.html`

Ba II 455.4 nm resonance line. Nevertheless, the other three Ba II lines located at 585.369, 614.173, and 649.691 nm (see Table 3.9) were all found in the upper CCD of the red arm covering the range 583-680 nm. More details of the spectra acquisition and reduction procedure are provided by Yong et al. (2005). All red giants studied here were located at or below the red giant branch (RGB) bump.

3.2.2 Atmospheric parameters and iron abundances

Continuum normalization of the observed spectra and equivalent width (EW) measurements were made using the `DECH20T`[7] software package (Galazutdinov 1992), where the EWs were determined using a Gaussian fit to the observed line profiles.

Stellar model atmospheres used in the abundance determinations were calculated with the Linux port version (Sbordone et al. 2004; Sbordone 2005) of the `ATLAS9` code (Kurucz 1993), using the ODFNEW opacity distribution tables from Castelli & Kurucz (2003). Models were computed using the mixing length parameter $\alpha_{\rm MLT} = 1.25$ and microturbulence velocity of $\xi_{\rm t} = 1\,{\rm km\ s^{-1}}$, with the overshooting option switched off. The LTE abundances were derived using the Linux port version (Sbordone et al. 2004; Sbordone 2005) of the Kurucz WIDTH9[8] package (Kurucz 1993; Kurucz 2005; Castelli 2005).

The effective temperature, $T_{\rm eff}$, was determined under the assumption of excitation equilibrium, i.e., by requiring that the derived iron abundance should be independent of the excitation potential, χ (Fig. 3.7, upper panel). We required that the iron abundances determined from the Fe I and Fe II lines would be equal to obtain the value of surface gravity, $\log g$. The microturbulence velocity, $\xi_{\rm t}$, was determined by requiring that Fe I lines of different EWs would provide the same iron abundance (Fig. 3.7, lower panel). The derived effective temperatures, gravities, and microturbulence velocities of individual stars agreed to within 60 K, 0.2 dex, and 0.16 km s^{-1}, respectively, with those determined by Yong et al. (2005).

One should note, however, that determination of effective temperatures assuming excitation equilibrium of Fe I and Fe II lines must be done using

[7] `http://www.gazinur.com/DECH-software.html`

[8] `http://wwwuser.oat.ts.astro.it/castelli/sources/width9.html`.

3D hydrodynamical model atmospheres. This would be much desired since, as it was already shown in Chapter 2, the 3D–1D abundance corrections of Fe I may in fact be very large for stars at low metallicities and thus, in principle, this should influence the derived effective temperatures. In practice, however, such approach is not yet feasible, first of all because the CIFIST 3D model atmosphere grid is very sparse, with the large steps both in the effective temperatures and gravities (500 K and 1.0 dex, respectively). Nevertheless, it is obvious that such tests are necessary to better understand the combined effect stemming from the effective temperature and iron abundance determinations with the 3D hydrodynamical model atmospheres.

The LTE iron abundances for all stars in our sample were derived using 50-60 neutral iron lines (Table 15, Appendix B; note that the iron abundance derived from the ionized lines was required to match that of neutral iron, i.e., to obtain the estimate of surface gravity, thus it is not an independent iron abundance measurement). To minimize the impact of NLTE effects on the iron abundance determinations, we avoided neutral iron lines with the excitation potential $\chi < 2.0$ eV. Oscillator strengths and damping constants for all iron lines were retrieved from the VALD database (Kupka et al. 2000). The obtained iron abundances are provided in Table 3.8. The contents of the Table are as follows: the star identification and its coordinates are given in Cols. 1–3, effective temperatures and iron abundance derivatives relative to the excitation potential are in columns 4 and 5, respectively, the adopted microturbulence velocity and iron abundance derivative relative to the equivalent width are in columns 6 and 7, respectively, the adopted values of $\log g$ are in column 8, iron abundances obtained from Fe I and Fe II lines are in columns 9 and 10, respectively, and the difference between them is in column 11.

The mean iron abundance obtained for the 20 stars is $\langle$[Fe/H]$\rangle = -1.60 \pm 0.05$, which is in excellent agreement with [Fe/H] $= -1.62 \pm 0.02$ obtained by Yong et al. (2005).

3.2.3 1D LTE abundances

The only spectral feature of lithium available for the abundance analysis in stellar spectra is closely spaced resonance doublet located at 670.8 nm (see

Table 3.8. Target stars in NGC 6752, their adopted atmospheric parameters, and derived iron abundances.

Star	RA (2000)	Dec. (2000)	$T_{\rm eff}$, K	$dA/d\chi$ $\times 10^{-3}$, dex/eV	$\xi_{\rm t}$, km s^{-1}	dA/dEW $\times 10^{-3}$, dex/pm	log g, [cgs]	[Fe/H]$_{\rm I}$	[Fe/H]$_{\rm II}$	A(Fe I) – A(Fe II), dex
NGC 6752–1	19:10:47	−60:00:43	4750	−2.0	1.37	−1.9	1.95	−1.53	–1.50	−0.03
NGC 6752–2	19:11:11	−60:00:17	4780	−3.1	1.35	−0.2	1.98	−1.54	–1.52	−0.02
NGC 6752–3	19:11:00	−59:56:40	4800	6.9	1.37	−0.2	2.03	−1.59	−1.60	0.01
NGC 6752–4	19:11:33	−60:00:02	4810	−4.9	1.42	0.8	2.04	−1.59	−1.58	−0.01
NGC 6752–6	19:10:34	−59:59:55	4800	−7.6	1.40	0.3	1.97	−1.58	−1.58	0.00
NGC 6752–7	19:10:57	−60:00:41	4830	−11.1	1.39	0.2	2.10	−1.77	−1.75	−0.02
NGC 6752–8	19:10:45	−59:58:18	4910	0.9	1.31	−0.3	2.25	−1.60	−1.60	0.00
NGC 6752–9	19:10:26	−59:59:05	4820	5.8	1.38	−0.9	2.26	−1.61	−1.59	−0.02
NGC 6752–10	19:11:18	−59:59:42	4840	−1.4	1.34	0.3	2.13	−1.56	−1.55	−0.01
NGC 6752–11	19:10:50	−60:02:25	4870	1.6	1.33	0.9	2.13	−1.56	−1.56	0.00
NGC 6752–12	19:10:20	−60:00:30	4840	3.5	1.36	0.4	2.15	−1.60	−1.63	0.03
NGC 6752–15	19:10:49	−60:01:55	4850	0.6	1.35	−1.3	2.19	−1.57	−1.56	−0.01
NGC 6752–16	19:10:15	−59:59:14	4850	−0.8	1.35	0.5	2.06	−1.63	−1.63	0.00
NGC 6752–19	19:11:23	−59:59:40	4930	−4.0	1.45	0.1	2.23	−1.64	−1.63	−0.01
NGC 6752–20	19:10:36	−59:56:08	4930	2.5	1.25	−0.1	2.33	−1.56	−1.59	0.03
NGC 6752–21	19:11:13	−60:02:30	4900	−10.3	1.34	0.0	2.33	−1.62	−1.61	−0.01
NGC 6752–23	19:11:12	−59:58:29	4960	1.7	1.28	1.9	2.35	−1.57	−1.55	−0.02
NGC 6752–24	19:10:44	−59:59:41	4950	−2.8	1.19	1.3	2.28	−1.63	−1.63	0.00
NGC 6752–29	19:10:17	−60:01:00	4900	1.9	1.31	−2.0	2.24	−1.68	−1.63	−0.05
NGC 6752–30	19:10:39	−59:59:47	4940	−4.5	1.18	−0.3	2.42	−1.64	−1.62	−0.02
mean								−1.60	−1.60	
σ								0.05	0.05	

Note: Fe II abundances were adjusted to match the abundances determined from Fe I lines, in order to estimate the surface gravities of the target stars. The difference between the corresponding abundance ratios, [Fe/H]$_{\rm I}$, and [Fe/H]$_{\rm II}$, is thus only indicative of the goodness of the gravity estimates.

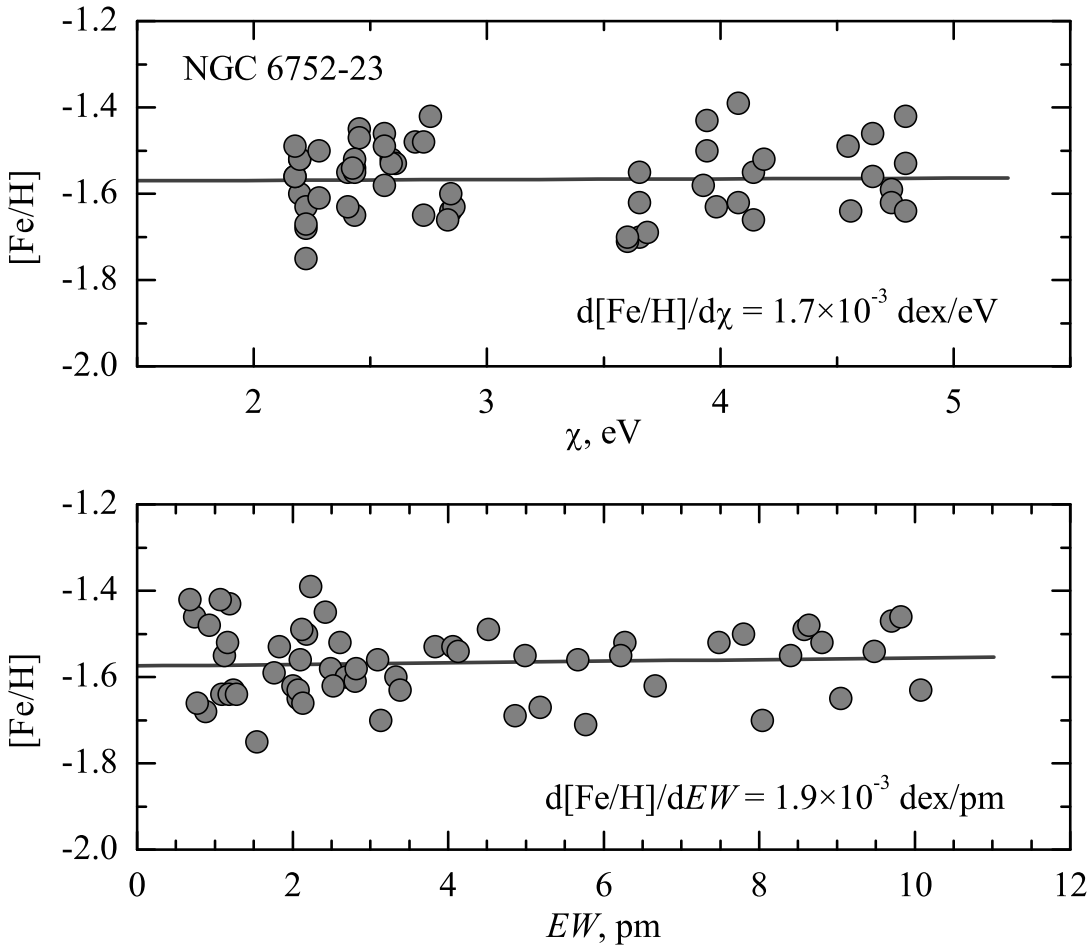

Fig. 3.7. [Fe/H] abundance ratios derived from Fe I lines for the star NGC 6752–23, plotted versus the excitation potential (top) and line equivalent width (bottom). Linear fits to the data are shown as solid lines. Note that there is a slight correlation between the best-fit slopes in the two panels: adjusting the temperature by zeroing the slope in the upper panel slightly changes the slope in the lower panel, while changes to the microturbulence velocity influence the slope in the upper panel. This correlation does not allow us to obtain zero-valued slopes in both panels simultaneously. The adopted atmospheric parameters of this star are $T_{\rm eff} = 4960\,{\rm K}$, $\log g = 2.35$, $\xi_{\rm t} = 1.28\,{\rm km\ s^{-1}}$, and [Fe/H] = −1.57.

Table 3.9). Gaussian function provides a poor fit to the asymmetric lithium line profile, therefore we obtained 1D LTE lithium abundances by fitting synthetic spectra to the observed spectral line profiles. Synthetic spectra were computed in 1D LTE using the Synthe spectral synthesis code, and `ATLAS9` model atmospheres computed using stellar atmospheric parameters from Table 3.8. An example of observed spectrum with the best fitting synthetic Li line profiles is shown in Fig 3.8. Values of the equivalent widths of the best fitting synthetic Li line profiles are provided in Table 16, Ap-

Table 3.9. Atomic parameters of the spectral lines used in this work.

element	λ[a], nm	χ, eV	log gf	log γ_{rad}	log $\frac{\gamma_4}{N_e}$[c]	log $\frac{\gamma_6}{N_H}$
Li I	670.776	0.00	−0.009	7.56	−5.78	−7.574
Li I	670.791	0.00	−0.309	7.56	−5.78	−7.574
Na I	568.263	2.10	−0.700	0.00	0.00	−6.855
Na I	568.821	2.10	−0.400	0.00	0.00	−6.855
Na I	615.423	2.10	−1.560	7.85	−4.39	0.00
Na I	616.075	2.10	−1.260	7.85	−4.39	0.00
Ba II	585.3688	0.604[a]	−1.000[a]	8.20[b]	−5.460	−7.190[d]
Ba II	614.1730	0.704[a]	−0.076[a]	8.20[b]	−5.480	−7.470[d]
Ba II	649.6910	0.604[a]	−0.377[a]	8.10[b]	−5.480	−7.470[d]

[a] Wiese & Martin (1980); [b] natural broadening constant, from Mashonkina & Bikmaev (1996); [c] Stark broadening constant, from Kupka et al. (2000); [d] van der Waals broadening constant, from Korotin et al. (2011)

pendix C.

Sodium abundances were obtained using the `WIDTH9` code and equivalent width measurements obtained by fitting Gaussian function to the observed spectral lines (see Table 17, Appendix C). We were unable to estimate oxygen abundance in the giants of NGC 6752 due to severe telluric contamination of the oxygen line at 630 nm, thus we adopted oxygen abundances determined by Yong et al. (2005). Sodium and oxygen abundances determined in the investigated stars are shown in Fig. 3.10, and the abundance of lithium versus that of sodium and oxygen is plotted in Fig. 3.11.

Barium abundances were derived using classical 1D model atmospheres, under the assumption of LTE. For this, three Ba II lines centered at 585.3688 nm, 614.1730 nm, and 649.6910 nm were used. Damping constants and other atomic parameters of the three barium lines are provided in Table 3.9. The line equivalent widths were measured with the `DECH20T` software (Table 18, columns 2–4). Hyperfine splitting of the 649.6910 nm line was not taken into account in the 1D LTE analysis. The derived barium abundances and barium-to-iron abundance ratios are given in Table 18, columns 5 and 7, respectively.

We note that the barium line at 614.1730 nm is blended with a neutral iron line located at 614.1713 nm. To estimate how this affects the accuracy of the abundance determination, we synthesized the barium 614.1730 nm

Table 3.10. Sensitivity of abundance to changes in atmospheric parameters.

Element	$\Delta T^*_{\rm eff}$ ±80 K	$\Delta \log g^*$ ±0.1 dex	$\Delta \xi^*_{\rm micro}$ ±0.1 km s^{-1}
Li I	+0.11	+0.00	−0.00
	−0.11	−0.00	+0.00
Na I	+0.04	−0.00	−0.01
	−0.04	+0.00	+0.01
Ba II	−0.03	−0.02	−0.07
	+0.03	+0.02	+0.07

line with and without the blending iron line, for all stars in our sample. The comparison of the equivalent widths of blended and non-blended lines reveals that the contribution of the iron blend never exceeds ∼ 2.4 %, or ≤ 0.05 dex in terms of the barium abundance. The contribution of the iron blend to the *EW* of the 614.1730 nm line was thus taken into account by reducing the measured equivalent widths of this barium line by 2.4 % for all stars. We would like to point out, however, that in the 1D NLTE analysis the barium abundances were derived by fitting the synthetic spectrum to the observed line profile, thus the influence of the iron blend at 614.1713 nm was properly taken into account.

Assessment of the abundance sensitivity on the atmospheric parameters is given in the Table 3.10. Lines of lithium are weak ($EW < 3$ pm) therefore its abundance is insensitive to the microturbulence velocity. Sodium lines are weak to moderately strong ($EW < 8$ pm) in the spectra of investigated red giants, which makes also sodium abundance only weakly sensitive to the choice of microturbulence velocity. However, barium lines in the target stars are strong and situated in the saturated part of the curve of growth, therefore it is not surprising that the uncertainty in the microturbulence velocity is the largest contributor to the uncertainty in the derived barium abundance.

The total contribution from the individual uncertainties in $T_{\rm eff}$, $\log g$, and $\xi_{\rm t}$ leads to the following systematic uncertainties in the abundance determinations of lithium, sodium, and barium: ∼ 0.11 dex, ∼ 0.04 dex,and ∼ 0.08 dex, respectively. We note, however, that the these numbers do not account for the uncertainty in the equivalent width determination and thus may only provide the lower limit to the systematic uncertainty (e.g., 5 per-

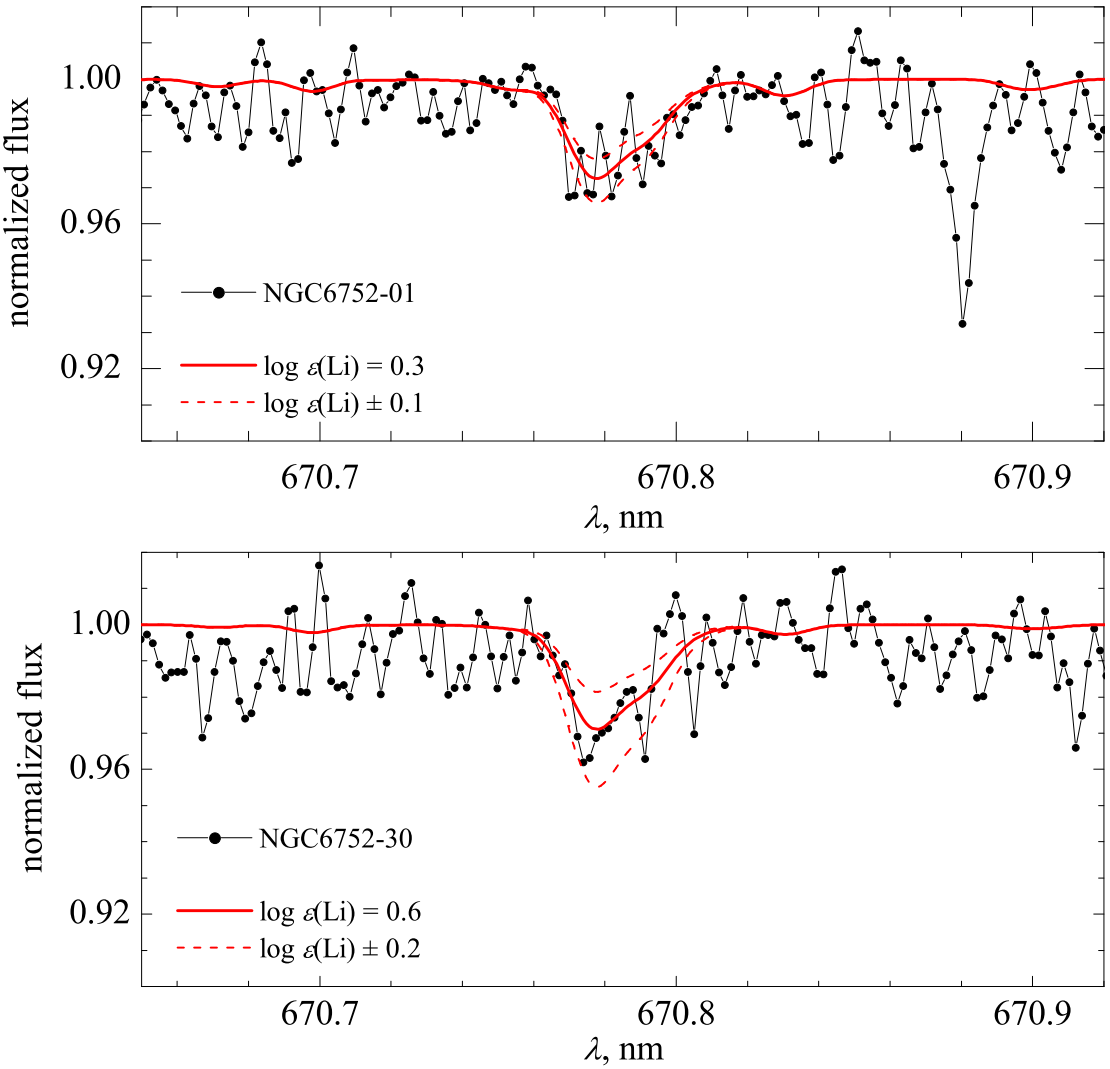

Fig. 3.8. Fit of the synthetic LTE profiles of the lithium line (red solid line) to the observed spectra of two red giants NGC 6752–01 (top) and NGC 6752–30 (bottom). Synthetic line profiles corresponding to the abundances 0.2 dex higher/lower than the best fit value are shown as red dashed lines.

cent in the equivalent width determination leads to the barium abundance uncertainty of ~ 0.1 dex).

The obtained mean 1D LTE abundance of lithium for the sample of 20 red giants in NGC 6752 is $\langle A(\mathrm{Li})\rangle_{\mathrm{1D\ LTE}} = 0.89 \pm 0.18$. Similarly, the obtained mean 1D LTE abundance of sodium for the same sample of stars is $\langle \mathrm{A(Li)}\rangle_{\mathrm{1D\ LTE}} = 4.78 \pm 0.31$ and the sodium-to-iron ratio is $\langle[\mathrm{Na/Fe}]\rangle_{\mathrm{1D\ LTE}} = 0.06 \pm 0.29$. The obtained mean 1D LTE barium abundance for the sample of 20 stars in NGC 6752 is $\langle A(\mathrm{Ba})\rangle_{\mathrm{1D\ LTE}} = 0.80 \pm 0.09$ and the barium-to-iron ratio is $\langle[\mathrm{Ba/Fe}]\rangle_{\mathrm{1D\ LTE}} = 0.24 \pm 0.05$. In all cases, the error is a square root of the variance calculated for the ensemble of

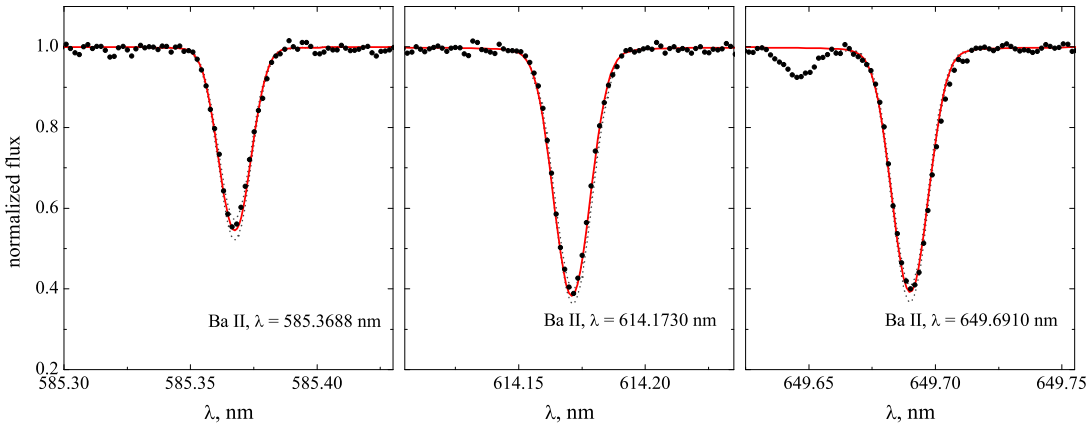

Fig. 3.9. Fit of the synthetic NLTE profiles of the Ba II lines (solid line) to the observed spectrum of the red giant NGC6752–23 (dots). Synthetic line profiles corresponding to the abundances 0.1 dex higher/lower than the best-fit value are shown as dashed lines.

individual abundance estimates of 20 stars. The difference between the individual barium abundances derived in a given star using the three barium lines is always below ~ 0.1 dex.

3.2.4 1D NLTE abundances

The one dimensional (1D) NLTE abundances of barium were determined using the version of the 1D NLTE spectral synthesis code `MULTI` (Carlsson 1986) modified by Korotin et al. (1999) (Section 1.2.1).

The solar abundances of iron and barium were assumed to be $\log A(\mathrm{Fe})_\odot = 7.50$ and $\log A(\mathrm{Ba})_\odot = 2.17$ respectively, on the scale where $\log A(\mathrm{H})_\odot = 12$. These abundances were determined using the Kurucz Solar Flux Atlas (Kurucz et al. 1984) and the same NLTE approach as applied in this study.

A typical fit of the synthetic line profiles to the observed spectrum is shown in Fig. 3.9, where we plot synthetic and observed profiles of all three barium lines used in the analysis. The elemental abundances and barium-to-iron abundance ratios derived for the individual cluster giants are provided in Table 18 (columns 6 and 8, respectively).

The mean sodium-to-iron ratio derived in 20 red giants of NGC 6752 using 1D hydrostatic model atmospheres and assuming NLTE is $\langle[\mathrm{Na/Fe}]\rangle_{\mathrm{1D\ NLTE}} = 0.05 \pm 0.23$. Similarly, the mean derived 1D NLTE barium-to-iron ratio for the 20 cluster red giants is $\langle[\mathrm{Ba/Fe}]\rangle_{\mathrm{1D\ NLTE}} =$

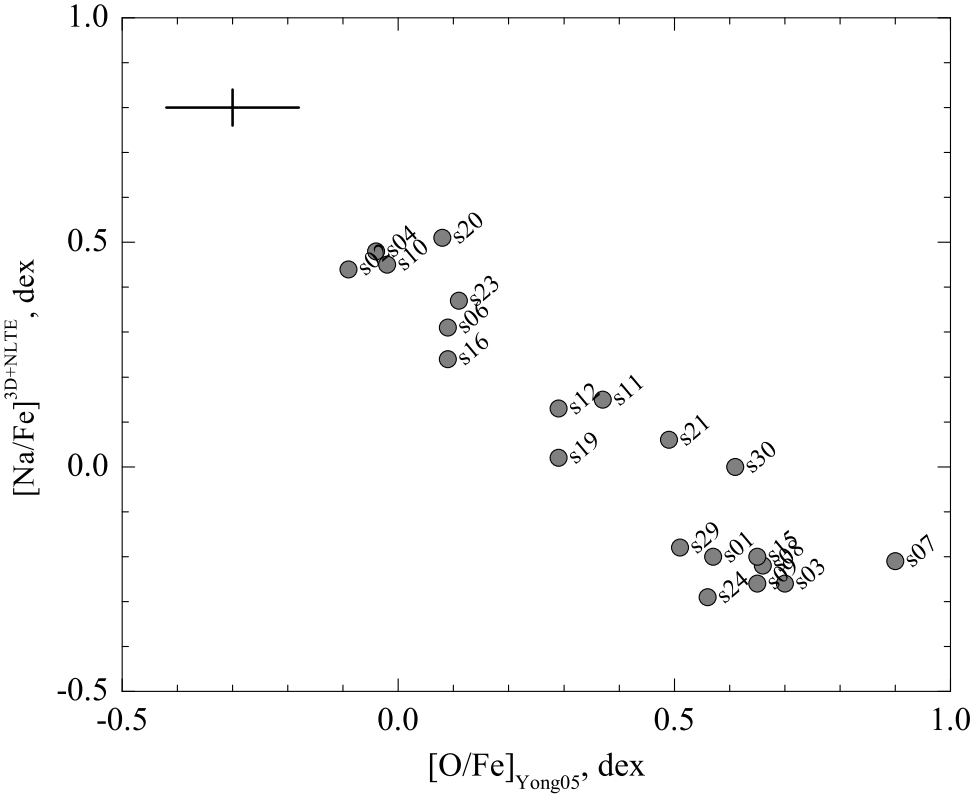

Fig. 3.10. Sodium-oxygen abundance in the giants of NGC 6752. Sodium abundance was estimated in this work, while oxygen abundance is from Yong et al. (2005). Star identifications corresponding to Table 3.8 are shown next to symbols.

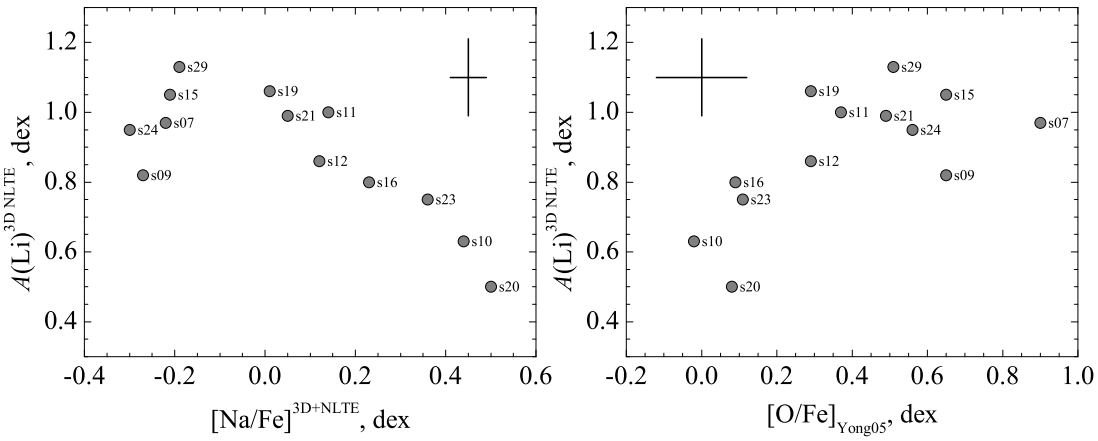

Fig. 3.11. Lithium abundance shown against sodium (left panel) and oxygen **(right panel)** abundances in the red giants of NGC 6752. Lithium and sodium abundances were estimated in this work, while the oxygen abundance was taken from Yong et al. (2005). Typical error bars are shown in the top right/left corners of the panels. Star identifications corresponding to Table 3.8 are shown next to symbols.

0.05 ± 0.06. In both cases the error is the square root of the variance in abundance estimates obtained assuming 1D NLTE for the ensemble of 20 stars, thus measures the star-to-star variation in the element-to-iron ratio. The individual line-to-line abundance scatter was always significantly smaller than 0.1 dex both for sodium and barium.

We find that barium lines generally appear stronger in NLTE than in LTE, which leads to lower NLTE barium abundances. This is in accord with the results obtained by Short & Hauschildt (2006) for the metallicity of NGC 6752, and similar to the trends obtained for cool dwarfs by Mashonkina et al. (1999). The NLTE–LTE abundance corrections for the three individual barium lines are always very similar, with the differences being within a few hundredths of a dex.

3.2.5 3D–1D abundance corrections

We have used the 3D hydrodynamical CO^{5}BOLD (Freytag et al. 2012) and 1D hydrostatic LHD (Caffau & Ludwig 2007) stellar atmosphere models to investigate how strongly the formation of lithium, sodium, and barium lines may be affected by convective motions in the stellar atmosphere (detailed description of the model atmospheres used is provided in Chapter 1).

Since we did not have CO^{5}BOLD models available for the entire atmospheric parameter range covered by the red giants in NGC 6752, we estimated the importance of 3D hydrodynamical effects only for stars on the lower RGB. For this purpose, we used a set of 3D hydrodynamical CO^{5}BOLD models with $T_{\rm eff}$ = 5000 K and $\log g$ = 2.5, at four different metallicities, [M/H] = 0.0, −1.0, −2.0, and −3.0[9]. Allowing for the error margins of ∼ 100 K in the effective temperature and ∼ 0.25 dex in gravity, we assumed that the effective temperature and gravity of this model set is representative of the atmospheric parameters of the stars NGC 6752–08, and NGC 6752–19 to NGC6752–30 (8 objects, see Table 3.8). For these stars, the extreme deviations from the parameters of the 3D model are $\Delta T_{\rm eff}$ ∼ 110 K and $\Delta \log g$ ∼ 0.26. These differences would only have a marginal effect on the uncertainty in the abundance estimates, i.e., the systematic uncertainty for the 3D barium abundance derivations would only increase from ±0.08 dex

[9]The models at four metallicities were used to interpolate the 3D–1D abundance corrections at the metallicity of NGC 6752.

Table 3.11. Parameters of the 3D hydrodynamical CO^{5}BOLD atmosphere models used in this work.

$T_{\rm eff}$, K	$\log g$	[M/H]	Grid dimension, Mm x × y × z	resolution x × y × z
4970	2.5	0	573×573×243	160×160×200
4990	2.5	−1	573×573×245	160×160×200
5020	2.5	−2	584×584×245	160×160×200
5020	2.5	−3	573×573×245	160×160×200

quoted in Sect. 3.2.3 to ±0.10 dex.

The 3D hydrodynamical models were taken from the CIFIST 3D model atmosphere grid (Ludwig et al. 2009). The model parameters are summarized in Table 3.11. The physical size of the 3D model box was chosen so that it would accommodate at least ten convective cells in the horizontal plane. Monochromatic opacities used in the model calculations were grouped into five opacity bins for [M/H] = 0.0 and six opacity bins for [M/H] = −1.0, −2.0, −3.0 models. The 1D LHD models were calculated for the same set of atmospheric parameters using the same equation of state, opacities, and chemical composition as in the case of the 3D hydrodynamical models.

To illustrate the differences between the 3D hydrodynamical and 1D classical stellar model atmospheres, we show their temperature stratifications at the metallicity of [M/H] = −2.0, which is the closest to that of NGC 6752 (Fig. 3.12, upper panel). In the same figure, we also indicate the typical formation depths of the three barium lines. It is obvious that at these depths, temperature of the 3D hydrodynamical model fluctuates very strongly, especially in the outer atmosphere, as indicated by the RMS value of horizontal temperature fluctuations ($\Delta T_{\rm RMS} = \sqrt{\langle (T - T_0)^2 \rangle_{x,y,t}}$, where T_0 is the temporal and horizontal temperature average obtained on surfaces of equal optical depth). As we see below, differences in the atmospheric structures lead to differences in the line formation properties and henceforth to differences in barium abundances obtained with the 3D hydrodynamical and 1D classical model atmospheres.

Twenty 3D snapshots (i.e., 3D model structures at different instants in time) were selected to calculate the Li I, Na I, and Ba II line profiles. The snapshots were chosen in such a way that the statistical properties of the

snapshot sample (average effective temperature and its r.m.s value, mean velocity at the optical depth unity, etc.) would match as close as possible those of the entire ensemble of the 3D model run. The 3D line spectral synthesis was performed for each individual snapshot and the resulting line profiles were averaged to yield the final 3D spectral line profile.

The 3D–1D abundance corrections for Li, Na, and Ba were calculated using the equivalent widths and microturbulence velocities of the target stars derived in Sect. 3.2.2 and 3.2.3. Furthermore, cubic interpolation was used to interpolate between the 3D–1D abundance corrections derived at four different metallicities to obtain its value at the metallicity of the cluster, [Fe/H] = −1.6. The cubic interpolation between the four values of metallicities was chosen because of the nonlinear dependence of the 3D–1D abundance corrections on metallicity.

3D–1D abundance corrections for the sodium lines which have higher excitation potential compared to the barium lines (2.1 eV and 0.6 eV respectively) are always positive and never exceed 0.025 dex (see Table 3.12). On the other hand, convection has a larger impact on the formation of lithium lines: the 3D–1D abundance correction is $\Delta_{\mathrm{3D-1D\ LTE}} = -0.16$ dex. Spectral lines of sodium were moderately strong ($EW \leq 8$ pm) and thus were less sensitive to the choice of microturbulence velocity used with the comparison 1D model atmosphere. This resulted in very weak dependence of the 3D–1D abundance corrections on the microturbulence velocity (see Table 3.12).

On the other hand, barium lines in the target stars are strong (cf. Table 18) and thus the derived 3D–1D abundance corrections are sensitive to the microturbulence velocity, ξ_{t}, of the comparison 1D model. The abundance corrections are provided in Table 3.13, which contains the $\Delta_{\mathrm{3D-1D}}$ and $\Delta_{\mathrm{3D-\langle 3D\rangle}}$ abundance corrections for the three individual Ba II lines (columns 2–4), the 3D–1D abundance correction for each star (i.e., averaged over the three barium lines, column 5), the microturbulence velocity used with the 1D comparison model (column 6, from Sect. 3.7), the 3D LTE barium abundances (column 7), the 3D LTE barium-to-iron ratio (column 8), and finally both the 1D NLTE barium-to-iron ratio before (column 9, from Sect. 3.2.4) and after correction for the 3D effects (column 10).

Table 3.12. The 3D+NLTE sodium abundances in the atmospheres of red giants in NGC 6752.

Star	$\Delta^{\rm line}_{\rm 3D-1D}$, $\Delta^{\rm line}_{\rm 3D-\langle 3D\rangle}$, dex			$\Delta_{\rm 3D-1D}$	$\xi_{\rm t}$	A(Na)	[Na/Fe]	[Na/Fe]	[Na/Fe]
	NaI5683	NaI5688	NaI6161	dex	km s^{-1}	3D LTE	3D LTE	1D NLTE	3D+NLTE
NGC 6752–08	0.01 −0.04	0.01 −0.05	0.01 −0.04	0.01	1.31	4.51	−0.08	−0.14	−0.13
NGC 6752–19	0.01 −0.05	0.01 −0.05	0.01 −0.04	0.01	1.45	4.71	0.16	0.09	0.10
NGC 6752–20	0.02 −0.06	0.02 −0.06	0.01 −0.05	0.02	1.25	5.28	0.65	0.58	0.60
NGC 6752–21	0.01 −0.06	0.02 −0.05	0.01 −0.04	0.02	1.34	4.77	0.20	0.15	0.17
NGC 6752–23	0.01 −0.05	0.02 −0.06	0.01 −0.04	0.01	1.28	5.13	0.51	0.42	0.43
NGC 6752–24	0.01 −0.04	0.01 −0.04	0.01 −0.04	0.01	1.19	4.41	−0.15	−0.16	−0.15
NGC 6752–29	0.01 −0.04	0.01 −0.04	0.01 −0.04	0.01	1.31	4.47	−0.04	−0.10	0.00
NGC 6752–30	0.01 −0.05	0.01 −0.05	0.01 −0.04	0.01	1.18	4.69	0.14	0.12	0.13
					mean:	4.75	0.17	0.12	0.14
					sigma:	0.31	0.28	0.27	0.26

Table 3.13. The 3D+NLTE barium abundances of red giants in NGC 6752.

Star	$\Delta^{\rm line}_{\rm 3D-1D}$, $\Delta^{\rm line}_{\rm 3D-\langle 3D\rangle}$, dex						$\Delta_{\rm 3D-1D}$	$\xi_{\rm t}$	A(Ba)	[Ba/Fe]	[Ba/Fe]	[Ba/Fe]
	BaII5854		BaII6142		BaII6497		dex	km s^{-1}	3D LTE	3D LTE	1D NLTE	3D+NLTE
NGC 6752–08	0.05	0.00	0.08	−0.01	0.06	−0.03	0.06	1.31	0.90	0.33	0.15	0.21
NGC 6752–19	0.13	0.08	0.18	0.11	0.15	0.07	0.15	1.45	0.84	0.31	0.04	0.19
NGC 6752–20	0.01	−0.04	0.04	−0.05	0.02	−0.07	0.02	1.25	0.89	0.28	0.14	0.16
NGC 6752–21	0.07	0.02	0.10	0.02	0.08	−0.01	0.08	1.34	0.90	0.35	0.09	0.17
NGC 6752–23	0.02	−0.03	0.06	−0.02	0.04	−0.05	0.04	1.28	0.92	0.32	0.12	0.16
NGC 6752–24	−0.02	−0.07	−0.01	−0.08	−0.03	−0.10	−0.02	1.19	0.66	0.12	−0.01	−0.03
NGC 6752–29	0.05	0.00	0.08	0.01	0.06	−0.02	0.06	1.31	0.73	0.24	0.02	0.08
NGC 6752–30	−0.03	−0.08	−0.01	−0.09	−0.02	−0.11	−0.02	1.18	0.80	0.27	0.13	0.11
								mean:	0.83	0.28	0.08	0.13
								sigma:	0.09	0.07	0.06	0.08

Abundance corrections are sensitive to the choice of the 1D microturbulence velocity and line strength, therefore stars with very similar atmospheric parameters may have different abundance corrections. This is, for example, the case with NGC 6752-19 and NGC 6752-30. These two stars have largest and smallest microturbulence velocities in the entire sample, respectively, and NGC 6752-19 has slightly stronger barium lines than NGC 6752-30 (Table 18, Appendix C). This leads to noticeably different abundance corrections, despite both stars having very similar effective temperatures and gravities (Table 3.13).

3.2.6 Discussion

3.2.6.1 1D LTE and NLTE abundances in NGC 6752

Our results show a rather well defined sodium-oxygen abundance anti-correlation, such as the one observed in the majority of Galactic globular clusters (Gratton et al. 2012). Obtained results results agree well with those obtained in a similar study of Carretta et al. (2007) but for a much larger sample of approximately 150 RGB stars. There are also hints for lithium-sodium abundance anti-correlation and lithium-oxygen abundance correlation, although their statistical significance due to small sample size is not high.

Lithium and oxygen abundances in NGC 6752 were determined in a much larger sample of 112 turn-off (TO) point stars by Shen et al. (2010). Their analysis has shown that lithium and oxygen abundances were positively correlated, with a 98% probability. In addition, unevolved stars showed significantly larger lithium abundance for a given oxygen abundance compared to giants. The largest lithium abundance determined in the TO stars by Shen et al. (2010) is 2.5–2.6 dex. This could be compared to 1.1–1.2 dex obtained for the giants in this work (Fig 3.11). The difference of $\approx$ 1.4 dex in the lithium abundance can be explained by the evolutionary effects, i.e., when deepening convective zone of a star which moves from the main sequence to the red giant branch brings stellar material to deeper and hotter layers where lithium is gradually destroyed in nuclear reactions.

Generally, the mean 1D LTE barium-to-iron abundance ratio obtained in this work, $\langle[\mathrm{Ba/Fe}]\rangle_{\mathrm{1D\ LTE}} = 0.24 \pm 0.05$, agrees well with the 1D LTE

abundance ratios derived for this cluster by other authors. For example, James et al. (2004) derived $\langle$[Ba/Fe]$\rangle = 0.18 \pm 0.11$ from 9 main-sequence and 9 subgiant stars in NGC 6752. We note that the mean barium-to-iron ratio of James et al. (2004) based on the measurements of only subgiant stars is $\langle$[Ba/Fe]$\rangle = 0.25 \pm 0.08$, i.e., in this case the agreement with our LTE estimate is even better. The barium-to-iron ratios obtained by Norris & Da Costa (1995) and Yong et al. (2005) are lower, $\langle$[Ba/Fe]$\rangle = 0.00 \pm 0.13$ and $\langle$[Ba/Fe]$\rangle = -0.06 \pm 0.13$, respectively.

The disagreement between the results of Yong et al. (2005) and those obtained here is somewhat concerning, especially since both studies were based on the same set of UVES spectra, while the atmospheric parameters and iron abundances of individual stars employed by us and Yong et al. (2005) agree very well (Sect. 3.2.2). Moreover, the comparison of the equivalent width measurements obtained by us and Yong et al. (2005) also shows good agreement. One would thus also expect good agreement in the derived barium abundances – which is unfortunately not the case. We therefore felt it was important to look into the possible causes of this discrepancy.

To this end, we first obtained the 1D LTE barium abundances using the `MULTI` code. This independent abundance estimate was made using the same procedure as for the 1D NLTE abundance derivations, i.e., by fitting the observed and synthetic line profiles of the three Ba II lines, with the difference that in this case the line profile calculations performed with `MULTI` were done under the assumption of LTE. The mean barium-to-iron abundance ratio obtained in this way, $\langle$[Ba/Fe]$\rangle = 0.22 \pm 0.06$, agrees well with the value derived in Section 3.2 ($\langle$[Ba/Fe]$\rangle = 0.24 \pm 0.05$).

In their abundance determinations, Yong et al. (2005) used an older version of the `ATLAS9` models (Kurucz 1993). The differences between these `ATLAS9` models and those used in our work is that (a) different opacity tables were used in the two cases (i.e., ODFNEW from Castelli & Kurucz 2003, with our models), and (b) the `ATLAS9` models of Kurucz (1993) were calculated with the overshooting parameter switched on, while in our case the overshooting was switched off. To check the influence of these differences on the abundance derivations, we obtained the 1D LTE barium abundance using the older atmosphere models of Kurucz (1993), with the atmospheric pa-

rameters and iron abundances derived in Sect. 3.2.2. In this case, the mean derived barium-to-iron abundance ratio was $\langle$[Ba/Fe]$\rangle_{\rm 1D\ LTE} = 0.23 \pm 0.05$, i.e., the effect of differences in the model atmospheres was only ~ 0.01 dex. The change in the barium abundances owing to differences in the atomic parameters (line broadening constants, oscillator strengths) used in the two studies was more significant, i.e., the abundances derived by us using the atomic parameters of Yong et al. (2005) were ~ 0.1 dex lower. However, this still leaves a rather large discrepancy, ~ 0.15 dex, between the barium-to-iron ratios obtained by us and Yong et al. (2005), for which we unfortunately cannot find a plausible explanation.

As in the case of the 1D LTE abundances, the extent of the star-to-star variations in the derived 1D NLTE barium-to-iron ratio, $\langle$[Ba/Fe]$\rangle_{\rm 1D\,NLTE} = 0.05 \pm 0.06$, is small and can be fully explained by the uncertainties in the abundance determination. The 1D NLTE barium-to-iron ratio derived here is similar to the value $\langle$[Ba/Fe]$\rangle_{\rm 1D\,NLTE} = 0.09 \pm 0.20$ obtained for two red giants in M10 by Mishenina et al. (2009). The elemental ratios obtained in the two studies are thus very similar, although one should keep in mind that the estimate of Mishenina et al. (2009) is based on only two stars. The metallicities of the two clusters are very similar too, [Fe/H] = −1.56 in the case of M10 (Harris 1996, 2010 edition) and [Fe/H] = −1.60 for NGC 6752 (Sect. 3.2.2). Galactic field stars typically show no pronounced dependence of [Ba/Fe] on metallicity, although the scatter at any given metallicity is large (Sneden et al. 2008). One may therefore conclude that, taken into account the high [Ba/Fe] spread in field stars, the $\langle$[Ba/Fe]$\rangle$ ratio derived here is comparable to those seen in Galactic field stars and other globular clusters of similar metallicity.

3.2.6.2 3D-corrected NLTE abundances in NGC 6752

The 3D–1D abundance corrections of sodium and barium computed for eight RGB stars in NGC 6752 in our study (see Section 3.2.5 above) may provide a hint about the net extent to which the 3D hydrodynamical effects may influence spectral line formation (and thus, the abundance determinations) in their atmospheres (Table 3.12–3.13). In the case of all red giants investigated, the corrections for both elements are small, −0.03 to +0.15 dex,

with the mean abundance correction for the eight stars of $\Delta_{\rm 3D-1D} = 0.02$ and 0.05 for sodium and barium, respectively. We note though that the individual contributions to the abundance correction, $\Delta_{\rm 3D-\langle 3D\rangle}$ and $\Delta_{\rm \langle 3D\rangle-1D}$, are substantial ($\sim \pm 0.1$ dex) but often because of their opposite sign nearly cancel and thus the resulting abundance correction is significantly smaller (Table 3.13). This clearly indicates that the role of convection-related effects on the spectral line formation in these red giants cannot be neglected, even if the final 3D–1D abundance correction, $\Delta_{\rm 3D-1D}$, is seemingly very small.

The mean 3D LTE barium-to-iron abundance ratio obtained for the eight red giants is $\langle {\rm [Ba/Fe]} \rangle_{\rm 3D\ LTE} = 0.28 \pm 0.07$. The 3D LTE barium abundance measurements made for a given star from the three barium lines always agree to within ≈ 0.03 dex. In the case of all twenty giants studied here, the mean 1D NLTE barium-to-iron ratio corrected for the 3D-related effects is $\langle {\rm [Ba/Fe]} \rangle_{\rm 3D+NLTE} = 0.10 \pm 0.08$ and therefore is only slightly different from the 1D NLTE value obtained in Sect. 3.2.4. However, the positive sign of the 3D–1D abundance differences indicates that in the spectra of red giants in NGC 6752 the three studied Ba II lines will be *weaker* in 3D than in 1D, in contrast to what is generally seen in red giants at this metallicity (cf. Collet et al. 2007; Dobrovolskas et al. 2013).

For the Ba II lines, the 3D–1D abundance corrections are sensitive to the choice of microturbulence velocities used with the 1D models: an increase in the microturbulence velocity by 0.10 km s^{-1} leads to an increase of 0.07 dex in the 3D–1D abundance correction. At the same time, due to change in the microturbulence velocity of 0.10 km s^{-1} the 1D abundance itself would *decrease* by roughly –0.07 dex. The result therefore is that although the 3D correction is sensitive to microturbulence, the 3D corrected abundance is not.

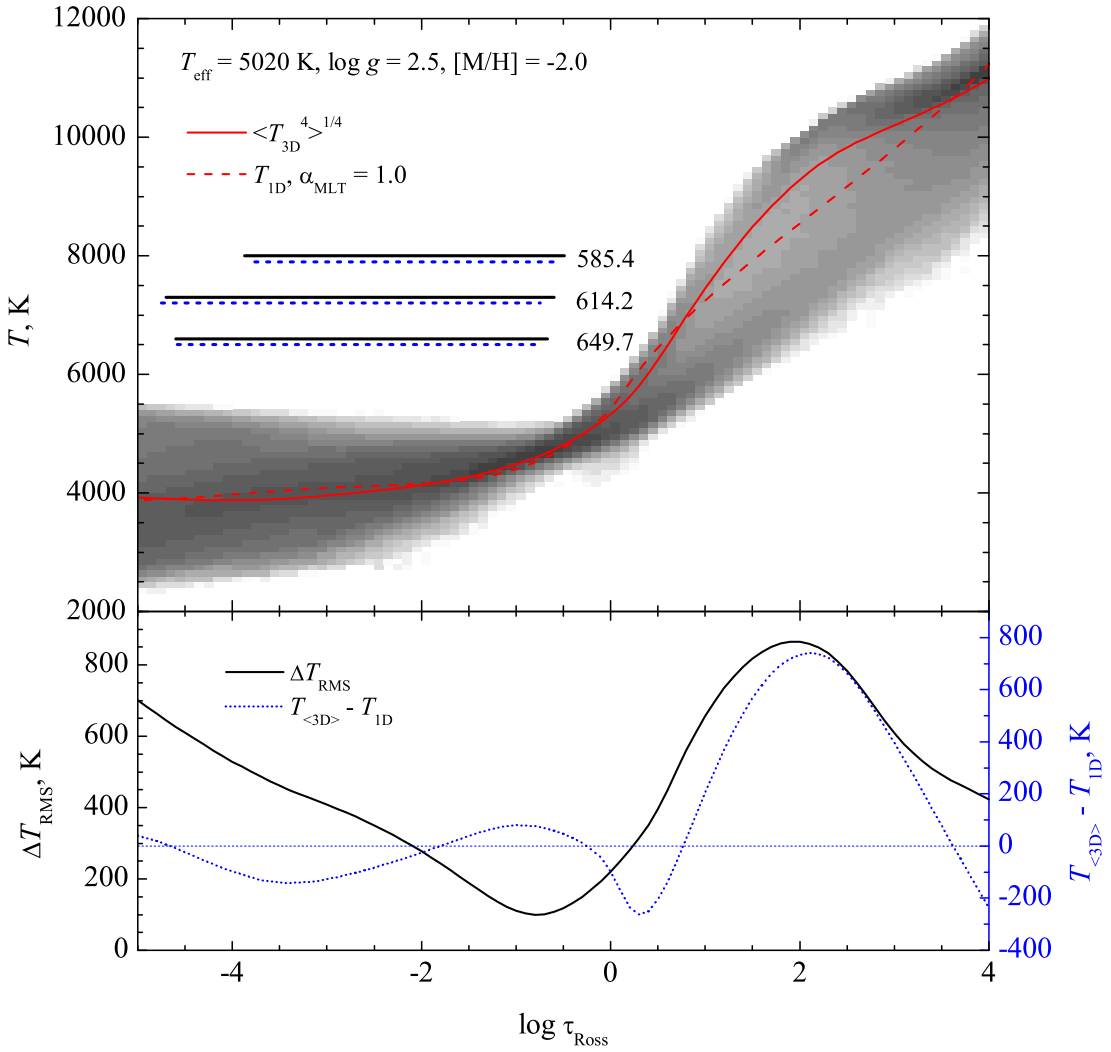

Fig. 3.12. Top panel: Temperature stratification in a single snapshot of the 3D hydrodynamical CO5BOLD model at the metallicity [M/H]= –2. Gray shaded area shows the temperature probability density on a logarithmic scale, with darker shades meaning a higher probability of finding a particular temperature value in the 3D model simulation box. Solid red line shows the mean temperature stratification of the 3D model and dashed red line is the 1D LHD model temperature stratification. Horizontal bars show the optical depth intervals where 90% of the line equivalent width is formed in LTE: black bars correspond to the 3D model while the blue dashed bars mark line forming regions in 1D. Numbers next to the bars designate the wavelength of the given Ba II line in nm. **Bottom panel:** RMS value of horizontal temperature fluctuations in the 3D model (black line) and temperature difference between the mean 3D and 1D models (blue dashed line).

Summary and conclusions

We have investigated the influence of convection on the spectral line formation in the atmospheres of main sequence turn off (TO) point and red giant branch (RGB) stars. To this end, we synthesized a large number of fictitious atomic lines of astrophysically important tracer elements, using for this purpose the 3D hydrodynamical CO^{5}BOLD and classical 1D LHD stellar model atmospheres (both types of models shared identical atmospheric parameters, opacities, equation of state, and chemical composition). The influence of convection on the line formation was investigated by focusing on the differences between the abundances inferred from a given spectral line by the requirement of producing a given equivalent width with the 3D and 1D model atmospheres, assuming LTE.

Overall, convection plays a considerable role in the atmospheres of both TO and RGB stars studied here. There are significant horizontal temperature fluctuations seen at different optical depths in the atmospheres of these stars that are caused either by convective up- or downflows (inner atmosphere), convective overshoot, and/or shock wave activity (outer atmosphere). This leads to substantial horizontal variations in the number densities of chemical species, causing significant deviations from the predictions of classical 1D models.

In particular, spectral line formation noticeably affected by convection in the atmosphere of red giant located close to the tip of RGB, but this influence depends on the line parameters and chemical species under consideration. The differences in elemental abundances inferred from a given spectral line with the 3D and 1D model atmospheres, $\Delta_{\rm 3D-1D}$, are most pronounced for high-excitation lines of ions and atoms of predominantly neutral elements. Their abundance corrections grow larger with increasing excitation potential, reaching values of $\Delta_{\rm 3D-1D} \approx -0.4$ dex for excitation potential $\chi = 10$ eV. The main physical reason for this 3D–1D difference is the increasingly nonlinear temperature dependence of the line opacity as χ increases. In a 3D atmosphere, the horizontal temperature fluctuations then lead to an enhancement of the effective line opacity with respect to

the 1D case, resulting in stronger lines in 3D and negative 3D–1D abundance corrections. Lines of neutral atoms of predominantly ionized elements have significantly smaller corrections, with $\Delta_{\mathrm{3D-1D}}$ not exceeding ± 0.1 dex. Here the temperature dependence of the line opacity due to ionization and excitation tend to partially cancel each other.

It is important to emphasize that in the case of a cool red giant studied here the 3D–1D corrections for all chemical species studied in this work showed a significant wavelength dependence. In most cases, the abundance corrections were significantly smaller in the near-infrared at λ 1600 nm than in the optical spectral range. Careful investigation revealed that this does not indicate that the atmospheric layers where the infrared lines originate were less affected by convection. Rather, the strong wavelength dependence of the 3D corrections is related to the fact that the continuum opacity is much more temperature dependent at λ 1600 nm (mainly H^- free-free absorption) than around λ 850 nm (mainly H^- bound-free absorption). It should be stressed though that this conclusion about the wavelength dependence of the 3D–1D corrections was reached for the red giant located close to the RGB tip; in case of stars located at the base of RGB this dependence is significantly less pronounced.

One may thus conclude that the spectral line formation in the atmospheres of red giant stars is a delicate process, governed by the subtle interplay between microscopic (atomic line parameters) and macroscopic (local temperature fluctuations) physics. The size of the 3D-hydrodynamical fluctuations and their effects on the line formation process can therefore only be assessed by dedicated radiation hydrodynamics simulations and detailed 3D line formation calculations.

We have also studied the influence of convection on the spectral line formation in the model atmospheres of a red giant stars located in the lower part of the RGB ($T_{\mathrm{eff}} \approx 5000\,\mathrm{K}$, $\log g = 2.5$), at four different metallicities, [M/H] $= 0.0, -1.0, -2.0, -3.0$. Again, the influence of convection was studied by focusing on the 3D–1D abundance corrections, i.e., the differences in abundances predicted for the same line equivalent width by the 3D hydrodynamical CO^{5}BOLD and classical 1D LHD model atmospheres. The abundance corrections were computed for a set of fictitious spectral lines of

various astrophysically important elements (C, O, Si, Ti, Fe, Ni, Ba, Eu), at three different wavelengths (λ = 400, 850, and 1600 nm) and four line excitation potentials ($\chi = 0, 2, 4, 6$ eV). Only weak lines ($EW < 0.5$ pm) were used in the analysis in order to avoid the influence of the microturbulence velocity used with the average $\langle$3D$\rangle$ and 1D model atmospheres.

The abundance corrections for the low-excitation lines of neutral atoms show significant dependence on both metallicity and line excitation potential, especially at low metallicities where differences in the abundances obtained with the 3D and 1D model atmospheres, $\Delta_{\rm 3D-1D}$, may reach to -0.6 dex. The corrections are largest for elements with the lowest ionization potentials (generally, < 6 eV), i.e., those that are predominantly ionized throughout the entire model atmosphere. The line opacity in this case is proportional to $\kappa_\ell \sim 10^{(E_{\rm ion}-\chi)/kT}$ which makes the low-excitation lines most temperature sensitive. Since the formation regions of low-excitation lines extend well into the outer atmosphere where temperature fluctuations are largest, this, in combination with the strong temperature sensitivity of the low excitation lines, leads to largest abundance corrections (note that differences between the average temperature profile of the 3D model and that of the 1D model are essentially depth-independent and typically do not exceed a few hundred Kelvin, irrespective of metallicity; the abundance corrections arising due to differences in the temperature profiles, $\Delta_{\langle\rm 3D\rangle-1D}$, are thus significantly smaller, typically $\leq \pm 0.1$ dex, whereas corrections due to horizontal temperature fluctuations, $\Delta_{\rm 3D-\langle 3D\rangle}$, may be significantly larger and reach to -0.6 dex, which also leads to large total abundance corrections, $\Delta_{\rm 3D-1D}$). The corrections decrease quickly with increasing excitation potential and for lines with $\chi > 2$ eV they are confined to ± 0.1 dex within the entire metallicity range. This is because lines with higher χ are less sensitive to temperature and, besides, they form deeper in the atmosphere where temperature fluctuations are significantly smaller. On the other hand, there is very little variation of abundance corrections with both metallicity and excitation potential for lines of neutral atoms of elements with high ionization potentials (eg. carbon and oxygen), i.e., those that are predominantly neutral throughout the entire atmosphere. In this case, it is the high-excitation lines that are most temperature sensitive, but since they

form deep in the atmosphere where temperature fluctuations are smaller the resulting abundance corrections are also small.

In case of lines of ionized atoms, the abundance corrections are small at all metallicities and excitation potentials ($\leq \pm 0.1$ dex) and show little variation with either [M/H] or χ. For elements that are predominantly ionized it is the high-excitation lines that are most temperature sensitive. Such lines form deep in the atmosphere where the horizontal temperature fluctuations are small, which leads to small $\Delta_{\mathrm{3D}-\langle\mathrm{3D}\rangle}$ abundance corrections. Since the $\Delta_{\langle\mathrm{3D}\rangle-\mathrm{1D}}$ corrections are never large, the total corrections are therefore significantly smaller than those for lines of, e.g., neutral atoms with low ionization potentials.

The abundance corrections obtained for red giants located close to the base of RGB show little variation with wavelength, at least in the range of 400–1600 nm. This is in contrast to what was obtained in the case of cooler red giant located close to the RGB tip, for which the corrections at 1600 nm were significantly smaller than in the optical wavelength range. This suggests that for certain elements the effects of convection on the spectral line formation may be equally large in a rather wide wavelength range.

Rather surprisingly, we find that differences in the treatment of scattering in the radiative transfer calculations seem to have a rather small impact on the resulting thermal structures of the red giant atmospheres studied here. The differences in the temperature profiles obtained when scattering opacity is neglected in optically thin regions and when scattering is treated as true absorption are always confined to < 120 K and only occur at the optical depths $\log\tau_{\mathrm{Ross}} \leq -2.0$. Nevertheless, for certain low-excitation lines this may lead to noticeable changes in the abundance corrections, with largest for lines of neutral elements with low ionization energies, ~ 0.1 dex. For lines of other neutral elements, as well as of ionized species, the changes are significantly smaller (< 0.02 dex).

In addition we have studied the influence of convection on the spectral line formation in the model atmospheres of main sequence stars ($T_{\mathrm{eff}} \approx 5900$ K, $\log g = 4.0$), at four different metallicities, [M/H] $= 0.0, -1.0,$ and -2.0. In this case, the 3D–1D abundance corrections for

the low-excitation lines of neutral atoms show significant dependence on both metallicity and line excitation potential, especially at low metallicities where differences in the abundances obtained with the 3D and 1D model atmospheres, $\Delta_{\rm 3D-1D}$, may reach to −1.1 dex. The results for a main sequence stars qualitatively agree with those obtained for red giants, in a sense that convection plays an increasingly important role on the spectral line formation with the decreasing metallicity, although the abundance corrections for main sequence stars are larger.

We have derived 1D NLTE abundances of lithium, sodium, and barium in the atmospheres of 20 RGB stars in the Galactic globular cluster NGC 6752. The mean lithium, sodium, and barium abundances are $\langle {\rm A(Li)} \rangle = 0.89 \pm 0.18$, $\langle {\rm [Na/Fe]} \rangle_{\rm 1D\ NLTE} = 0.05 \pm 0.23$, and $\langle {\rm [Ba/Fe]} \rangle_{\rm 1D\ NLTE} = 0.05 \pm 0.06$, respectively. (the error measures the star-to-star variation in the abundance ratio, see Sect. 3.2.2). Individual barium-to-iron abundance ratios show little star-to-star variation, which leads us to conclude that there is no intrinsic barium abundance spread in the RGB stars at or slightly below the RGB bump in NGC 6752. This conclusion is in line with the results obtained in other studies, for stars in both this and other GGCs (Norris & Da Costa 1995; James et al. 2004; Yong et al. 2005). On the contrary, abundances of lithium and sodium show significant trends, besides, we find a rather clearly pronounced Na–O anticorrelation, and hints for Na-Li anticorrelation and O-Li correlation.

In the RGB stars of NGC 6752, the 3D–1D abundance corrections of sodium and barium are generally small and do not exceed +0.02 and +0.15 dex, respectively. It would be misleading, however, to conclude that the role of the 3D effects in the formation of the sodium and barium lines in the atmospheres of red giants in NGC 6752 is minor. As a matter of fact, we have found that, e.g., in the case of barium, the 3D–1D abundance corrections owing to horizontal temperature inhomogeneities in the 3D model (i.e., $\Delta_{\rm 3D-\langle 3D \rangle}$ correction) *and* differences in the temperature profiles between the average ⟨3D⟩ and 1D models ($\Delta_{\rm \langle 3D \rangle-1D}$ correction) are substantial and may reach ∼ ±0.1 dex (Table 3.13). However, their sign depends on the line strength, and owing to this subtle fine-tuning their sum is significantly smaller, from −0.03 to 0.02 dex, which for this given set of atmospheric

and atomic line parameters maintains the size of the 3D–1D abundance corrections at the level of the errors in the abundance determination. The situation is very similar in case of sodium too, which indicates clearly that the 3D hydrodynamical effects in the atmospheres of RGB stars can not be neglected in the spectral line synthesis computations.

The barium-to-iron abundance ratio derived in the RGB stars in NGC 6752 is comparable to the one observed in Galactic halo stars of the same metallicity (Sneden et al. 2008). It is also similar to the mean barium-to-iron abundance ratio obtained by Mishenina et al. (2009) for 2 red giants in the Galactic globular cluster M10. We therefore conclude that the barium-to-iron abundance ratios obtained here generally agree with those seen in the oldest Galactic populations and are not very different from those observed in halo stars.

We also determined abundance of lithium in the atmospheres of 94 TO stars, as well as those of oxygen, and sodium in 110 TO stars belonging to the Galactic globular cluster 47 Tuc, taking into account both NLTE and 3D hydrodynamical effects. The departures from LTE play a dominant role in the abundance determination: differences in the derived abundances reach to $\Delta_{\mathrm{1D\,NLTE-LTE}} \approx -0.35\,\mathrm{dex}$ in the case of sodium and to $\Delta_{\mathrm{1D\,NLTE-LTE}} \approx -0.20\,\mathrm{dex}$ in the case of oxygen. The role of convection in the atmospheres of TO stars in 47 Tuc plays a much lesser role in the spectral line formation, which leads to significantly smaller abundance corrections of $\Delta_{\mathrm{3D\,LTE-1D\,LTE}} \approx +0.02\,\mathrm{dex}$ for sodium and $\Delta_{\mathrm{3D\,LTE-1D\,LTE}} \approx +0.05\,\mathrm{dex}$ for oxygen.

Sodium and oxygen abundances determined in the TO stars of 47 Tuc are anti-correlated and our result is in good agreement with that obtained by D'Orazi et al. (2010). On the other hand, the average lithium abundance obtained in our study, $\langle A(\mathrm{Li})\rangle = 1.78 \pm 0.18$, is ≈ 0.27 dex lower than that determined by D'Orazi et al. (2010). Our data also suggests the existence of weak Li–O correlation.

The mean Li abundance in 47 Tuc is lower than what is observed in other Galactic globular clusters by roughly a factor of three. The highest Li abundance observed in 47 Tuc is *lower* than the lowest Li abundances observed in the open cluster NGC 2243, that is only 0.2 dex more metal rich

but 8 Gyr younger than 47 Tuc. When put into context with Li observations in other globular and open clusters and field stars, our results suggest a scenario in which the Li depletion during the star's MS/TO/SGB lifetime, is essentially zero for stars of metallicity lower than about −1.0, and becomes more important as soon metallicity increases. The initial lithium abundance with which the stars were created may in fact depend only on their age (it is larger for the younger stars) and not on their metallicity. These facts may explain in a natural way, for example, the difference in the lithium content between 47 Tuc and NGC 2243. To confirm (or disprove) the proposed scenario it would be important to observe lithium in other Galactic globular clusters of metallicity around −1.0, which may also allow to determine the metallicity at which the convective envelope becomes deep enough to result in significant lithium depletion.

References

Allen, C.W. 1973, Astrophysical Quantities (Athlone Press)

Andrievsky, S. M., Spite, M., Korotin, S. A., Spite, F., François, P., et al. 2009, A&A, 494, 1083

Anstee, S. D., O'Mara, B. J. 1995, MNRAS, 276, 859

Asplund, M., Nordlund, Å., Trampedach, R., & Stein, R. F. 1999, A&A, 346, L17

Asplund, M. 2005, ARA&A, 43, 481

Asplund, M., Grevesse, N., & Sauval, A. J. 2005, ASPC, 336, 25

Asplund, M., Grevesse, N., Jacques Sauval, A., & Scott, P. 2009, ARA&A, 47, 481

Bagnulo S., Jehin E., Ledoux C., Cabanac R., Melo C., et al. 2003, The ESO Paranal Science Operations Team, Messenger 114, 10

Barklem, P. S., & O'Mara, B. J. 1997, MNRAS, 290, 102

Barklem, P. S., Piskunov, N., & O'Mara, B. J. 2000a, A&A, 355, L5

Barklem, P. S., Piskunov, N., & O'Mara, B. J. 2000b, A&A, 363, 1091

Barklem, P. S. 2007, A&A, 462, 781

Barklem, P. S. 2008, Phys. Scr, 133, 4023

Barklem, P. S., Belyaev, A. K., Dickinson, A. S., & Gadéa, F. X. 2010, A&A, 519, 20

Behara, N. T., Bonifacio, P., Ludwig, H.-G., Sbordone, L., González Hernández J.I., et al. 2010, A&A, 513, 72

Bensby, T., Feltzing, S., & Lundström, I. 2004, A&A, 415, 155

Bergbusch, P. A., & Stetson, P. B. 2009, AJ, 138, 1455

Boesgaard, A. M., Deliyannis, C. P., Stephens, A., & King, J. R. 1998, ApJ, 493, 206

Böhm-Vitense, E. 1958, ZAp, 46, 108

Bonifacio, P. 2002, A&A, 395, 515

Bonifacio, P., Pasquini, L., Molaro, P., Carretta, E., François, P. et al. 2007, A&A, 470, 153

Bonifacio P., Caffau, E., & Ludwig, H.-G. 2010, A&A, 524, A96

Caffau, E., & Ludwig, H.-G. 2007, A&A, 467, L11

Caffau, E., Ludwig, H.-G., Steffen, M., Ayres, T.R., Bonifacio, P., et al. 2008, A&A, 488, 1031

Caffau, E., Maiorca, E., Bonifacio, P., Faraggiana, R., Steffen, M., et al. 2009, A&A, 498, 877

Caffau, E., Ludwig, H.-G., Steffen, M., Freytag, B., & Bonifacio, P. 2011, Sol. Phys., 268, 255

Cannon, R. D., Croke, B. F. W., Bell, R. A., Hesser, J. E., & Stathakis, R. A. 1998, MNRAS, 298, 601

Carlsson, M. 1986, UppOR, 33

Carretta, E., Gratton, R. G., Lucatello, S., Bragaglia, A., & Bonifacio, P. 2005, A&A, 433, 597

E. Carretta, A. Bragaglia, R. G. Gratton, S. Lucatello, & Y. Momany 2007, A&A, 464, 927

Carretta, E., Bragaglia, A., Gratton, R. G., Lucatello, S., Catanzaro, G., et al. 2009a, A&A, 505, 117

Carretta, E., Bragaglia, A., Gratton, R. G., & Lucatello, S. 2009b, A&A, 505, 139

Carretta, E., Bragaglia, A., Gratton, R., D'Orazi, V., & Lucatello, S. 2009, A&A, 508, 695

Carretta, E., Bragaglia, A., Gratton, R. G., Recio-Blanco, A., Lucatello, S., et al. 2010a, A&A, 516, 55

Carretta, E., Bragaglia, A., Gratton, R. G., Lucatello, S., Bellazzini, M., et al. 2010b, A&A, 520, 95

Carretta, E., Lucatello, S., Gratton, R. G., Bragaglia, A., & D'Orazi, V. 2011, A&A, 533, 69

Castelli, F. 2005, Mem. Soc. Astron. Italiana, 8, 25

Castelli, F. 2005b, Mem. Soc. Astron. Italiana, 8, 44

Castelli, F., Gratton, R. G., & Kurucz, R. L. 1997, A&A, 318, 841

Castelli, F., & Kurucz, R. L. 2003, in: 'Modeling of Stellar Atmospheres', Proc. IAU Symp. 210, eds. N.E. Piskunov, W.W. Weiss, & D.F. Gray, poster A20 (CD-ROM); synthetic spectra available at `http://cfaku5.cfa.harvard.edu/grids`

Cayrel, R., Van 't Veer-Menneret, C., Allard, N. F., & Stehlé, C. 2011, A&A, 531, 83

Coc, A., Uzan, J.-P., & Vangioni, E. 2013, arXiv:1307.6955

Cohen, J. 2011, ApJ, 740L, 38

Collet, R., Hayek, W., Asplund M., Nordlund, Å., Trampedach, R., et al. 2011, A&A, 528, A32

Collet, R., Asplund, M., & Nissen, P. E. 2009, PASA, 26, 330

Collet, R., Asplund, M., & Trampedach, R. 2007, A&A, 469, 687

Cunto, W., Mendoza, C., Ochsenbein, F., & Zeippen, C. J. 1993, A&A, 275, L5

Cyburt, R. H., Fields, B. D., & Olive, K. A. 2008, JCAP, 11, 12

Da Costa, G. S., Held, E. V., Saviane, I., & Gullieuszik, M. 2009, ApJ, 705, 1481

Delbouille, L., Neven, L., & Roland, G. 1973, Photometric atlas of the solar spectrum from λ3000 to λ10000 (Institut d'Astrophysique, Universit´e de Li'ege

Dobrovolskas, V., Kučinskas, A., Andrievsky, S. M., Korotin, S. A, Mishenina, T. V., et al. 2012, A&A, 540, A128

Dobrovolskas, V., Kučinskas, A., Steffen, M., Ludwig, H.-G., Prakapavičius, D., et al. 2013, A&A, in press, DOI: 10.1051/0004-6361/201321036

D'Orazi, V., Lucatello, S., Gratton, R., Bragaglia, A., Carretta, E., et al. 2010, ApJ, 713L, 1

Drawin, H. W. 1969, ZPhy, 225, 483

François, P., Pasquini, L., Biazzo, K., Bonifacio, P., & Palsa, R. 2013, A&A in press, arXiv:1303.3027

Freytag, B., Steffen, M., Ludwig, H.-G., Wedemeyer-Böhm, S., Schaffenberger, W., et al. 2012, Journ. Comp. Phys., 231, 919

Fuhrmann, K., Axer, M., & Gehren, T. 1993, A&A, 271, 451

Galazutdinov, G. A. 1992, Preprint SAO RAS., 92, 96

Geisler, D., Villanova, S., Carraro, G., Pilachowski, C., Cummings, J., et al. 2012, ApJ, 756, 40

González Hernández, J., Bonifacio, P., Ludwig, H.-G., Caffau, E., Spite, M., et al. 2008, A&A, 480, 233

González Hernández, J.I., Bonifacio, P., Caffau, E., Steffen, M., Ludwig, H.-G., et al. 2009, A&A, 505, 13

Gratton, R. G., Fusi Pecci, F., Carretta, E., Clementini, G., Corsi, C. E., et al. 1997, ApJ, 491, 749

Gratton, R., Bonifacio, P., Bragaglia, A., Carretta, E., Castellani, V., et al. 2001, A&A, 369, 87

Gratton, R., Sneden, C., & Carretta, E. 2004, ARA&A, 42, 385

Gratton, R. G., Carretta, E., & Bragaglia, A. 2012, A&ARv, 20, 50

Gratton, R. G., Villanova, S., Lucatello, S., Sollima, A., Geisler, D., et al. 2012, A&A, 544, 12

Gray, D. F. 2012, AJ, 143, 112

Gray, D. F. 2005, PASP, 117, 711

Gray, D. F., Carney, B. W., & Yong, D. 2008, AJ, 135, 2033

Grevesse, N., & Sauval, A.J. 1998, Space Sci. Rev., 85, 161

Grundahl, F., Stetson, P. B., & Andersen, M. I. 2002, A&A, 395, 481

Gustafsson, B., Edvardsson, B., Eriksson, K., Jørgensen, U.G., Nordlund, Å., et al. 2008, A&A, 486, 951

Harris, W. E. 1996, AJ, 112, 1487

Hayek, W., Sing, D., Pont, F., & Asplund, M. 2012, A&A, 539, 102

Holzreuter, R., & Solanki, S. K. 2013, A&A, 558, 20

Igenbergs, K., Schweinzer, J., Bray, I., Bridi, D., & Aumayr, F. 2008, Atomic Data and Nuclear Data Tables, 94, 981

James, G., François, P., Bonifacio, P., Bragaglia, A., Carretta, E., et al. 2004, A&A, 414, 1071

Johansson, S., Litzén, U., Lundberg, H., & Zhang, Z. 2003, ApJ, 584, 107

Kaluzny, J., Pych, W., Rucinski, S. M., & Thompson, I. B. 2006, AcA, 56, 237

Klevas, J., Kučinskas, A., Ludwig, H.-G., Bonifacio, P., Steffen, M., et al. 2013, Proc. of the 2nd COBOLD Workshop, Mem. Soc. Astron. Italiana Suppl., 24, 79

Koch, A., Lind, K., & Rich, R. M. 2011, ApJ, 738, L29

Komatsu, E., Smith, K. M., Dunkley, J., Bennett, C.L., Gold, B., et al. 2011, ApJS, 192, 18

Korotin, S. A., & Mishenina, T. V. 1999, Astron. Rep., 43, 533

Korotin, S. A., Andrievsky, S. M., & Luck, R. E. 1999, A&A, 351, 168

Korotin, S., Mishenina, T., Gorbaneva, T., & Soubiran, C. 2011, MNRAS, 415, 2093

Kraft, R. P. 1994, PASP, 106, 553

Kučinskas, A., Steffen, M., Ludwig, H.-G., Dobrovolskas, V., Ivanauskas, A., et al. 2013, A&A, 549, A14

Kupka, F., Ryabchikova, T. A., Piskunov, N. E., Stempels, H. C., & Weiss, W. W. 2000, BaltA, 9, 590

Kurucz, R. L. arXiv:astro-ph/0605029

Kurucz, R. L. 2005, Mem. Soc. Astron. Italiana, 8, 14

Kurucz, R. L. 1993, ATLAS9 Stellar Atmosphere Programs and 2 km/s Grid, CD-ROM No.13, Cambridge, Mass.

Kurucz, R. L. 1970, SAOSR, 309

Kurucz, R. L., Furenlid, I., Brault, J., & Testerman, L. 1984, *Solar Flux Atlas from 296 to 1300nm*, National Solar Observatory, Sunspot, New Mexico

Lambert, D. L., & Reddy, B. E. 2004, MNRAS, 349, 757

Lane, R. R., Kiss, L. L., Lewis, G. F., Ibata, R. A., Siebert A., et al. 2010, MNRAS, 401, 2521

Lehnert, M. D., Bell, R. A., & Cohen, J. G. 1991, ApJ, 367, 514

Lind, K., Melendez, J., Asplund, M., Collet, R., & Magic, Z. 2013, A&A, 554, 96L

Lodders, K., Palme, H., & Gail, H. P. 2009, "Abundances of the elements in the solar system", Landolt-Börnstein, New Series, Vol. VI/4B, Chap. 4.4, J.E. Trümper (ed.), Berlin, Heidelberg, New York: Springer Verlag, p. 560-630

Ludwig, H.-G., & Steffen, M. 2012, Ap&SSProc., pt.2, p.125

Ludwig, H.-G., Caffau, E., Steffen, M., Freytag, B., Bonifacio, P., et al. 2009, Mem. Soc. Astron. Italiana, 80, 711

Ludwig, H.-G., Jordan, S., & Steffen, M. 1994, A&A, 284, 105

Ludwig, H.-G. 1992, Non-gray Radiation Transport in Numerical Simulations of Stellar Convection, Ph.D. Thesis, University of Kiel

Marino, A. F., Sneden, C., Kraft, R. P., Wallerstein, G., Norris, J. E., et al. 2011, A&A, 532, 8

Mashonkina, L. I., & Bikmaev, I. F. 1996, ARep, 40, 94

Mashonkina, L., Gehren, T., & Bikmaev, I. 1999, A&A, 343, 519

Mashonkina, L., Gehren, T., Shi, J.-R., Korn, A. J., & Grupp, F. 2011, A&A, 528, 87

Massari, D., Ferraro, F. R., Dalessandro, E., Lanzoni, B., Mucciarelli, A., et al. 2013, Mem. Soc. Astron. Italiana, 84, 236

Matteucci, F. 2010, IAU Symposium, 268, 453

Mihalas, D. Stellar Atmospheres, Freeman and Company

Mishenina T. V., Korotin S. A., Klochkova V. G., & Panchuk V. E. 2000, A&A, 353, 978

Mishenina, T. V., Soubiran, C., Kovtyukh, V. V., & Korotin, S. A. 2004, A&A, 418, 551

Mishenina, T. V., Kučinskas, A., Andrievsky, S. M., Korotin, S.A., Dobrovolskas, V., et al. 2009, BaltA, 18, 193

Monaco, L., Bonifacio, P., Sbordone, L., Villanova, S., & Pancino, E. 2010, A&A, 519, L3

Monaco, L., Villanova, S., Bonifacio, P., Caffau, E., Geisler, D., et al. 2012, A&A, 539, A157

Nordlund, Å. 1982, A&A, 107, 1

Norris, J. E., & Da Costa, G. S. 1995, ApJ, 447, 680

Norris, J. E., Freeman, K. C., & Mighell, K. J. 1996, ApJ, 462, 241

Origlia, L., Rich, R. M., Ferraro, F. R., Lanzoni, B., Bellazzini, M., et al. 2011, ApJ, 726, 20

Otsuki, K., Honda, S., Aoki, W., Kajino, T., & Mathews, G. J. 2006, ApJ, 641, L117

Pasquini, L., Bonifacio, P., Molaro, P., François, P., Spite, F., et al. 2005, A&A, 441, 549

Planck Collaboration, Ade, P. A. R., Aghanim, N., et al. 2013, arXiv:1303.5076

Prakapavičius, D., Steffen, M., Kučinskas, A., Ludwig, H.-G., Freytag, B., et al. 2013, Proc. of the 2nd COBOLD Workshop, Mem. Soc. Astron. Italiana Suppl., 24, 111

Prantzos, N. 2012, A&A, 542, A67

Press, W., Teukolsky S., Vetterling W., & Flannery B. 1992, Numerical recipes in C: The Art of Scientific Computing, 2nd edn. (Cambridge University Press)

Ramírez, I., Collet, R., Lambert, D. L., Allende Prieto, C., & Asplund, M. 2010, ApJL, 725, 223

Ramírez, I., Allende Prieto, C., Koesterke, L., Lambert, D. L., & Asplund, M. 2009, A&A, 501, 1087

Roederer, I. U., & Sneden, C. 2011, AJ, 142, 22

Sánchez-Blázquez, P., Marcolini, A., Gibson, B. K., Karakas, A. I., Pilkington, K., et al. 2012, MNRAS, 419, 1376

Sbordone, L. 2005, Mem. Soc. Astron. Italiana, 8, 61

Sbordone, L., Bonifacio, P., Caffau, E., Ludwig, H.-G., Behara, N. T. et al. 2010, A&A, 522, 26

Sbordone, L., Bonifacio, P., Castelli, F., & Kurucz, R. L. 2004, Mem. Soc. Astron. Italiana, 5, 93

Schlegel, D. J., Finkbeiner, D. P., & Davis, M. 1998, ApJ, 500, 525

Scott, P., Asplund, M., Grevesse, N., & Sauval, A. J. 2009, ApJ, 691, L119

Sestito, P., & Randich, S. 2005, A&A, 442, 615

Shen, Z.-X., Bonifacio, P., Pasquini, L., & Zaggia, S. 2010, A&A, 524L, 2

Short, C. I., & Hauschildt, P. H. 2006, ApJ, 641, 494

Sneden, C., Kraft, R. P., Shetrone, M. D., Smith, G.H., Langer, G.E., et al. 1997, AJ, 114, 1964

Sneden, C., Pilachowski, C. A., & Kraft, R. P. 2000, AJ, 120, 1351

Sneden, C., Cowan, J. J., & Gallino, R. 2008, ARA&A, 46, 241

Sobeck, J. S., Kraft, R. P., Sneden, C., Preston, G.W., Cowan, J.J., et al. 2011, AJ, 141, 175

Spergel, D. N., Verde, L., Peiris, H. V., Komatsu, E., Nolta, M. R., et al. 2003, ApJS, 148, 175

Spite, M., & Spite, F. 1982a, Nature, 297, 483

Spite, F., & Spite, M. 1982b, A&A, 115, 357

Steenbock, W., & Holweger, H. 1984, A&A, 130, 319

Steffen, M., & Holweger, H. 2002, A&A, 387, 258

Stehlé, C., & Hutcheon, R. 1999, A&AS, 140, 93

Storey, P. J., & Zeippen, C. J. 2000, MNRAS, 312, 813

Suntzeff, N. B., & Kraft, R. P. 1996, AJ, 111, 1913

van Regemorter, H. 1962, ApJ, 136, 906

Vernazza J. E., Avrett E. H., & Loeser R. 1981, ApJ.S.S., 45, 635

Vögler, A., Bruls, J. H. M. J., & Schüssler, M. 2004, A&A, 421, 741

Wiese, W. L., & Martin, G. A. 1980, in Wavelengths and transition probabilities for atoms and atomic ions: Part 2. Transition probabilities, NSRDS-NBS Vol. 68

Yong, D., Grundahl, F., Nissen, P. E., Jensen, H. R., & Lambert, D. L. 2005, A&A, 438, 875

Appendix A. Atmospheric parameters of the main sequence turn-off point stars in 47 Tuc

Table 14. List of the investigated stars in 47 Tuc, their adopted atmospheric parameters, and determined abundances of Li, O, and Na.

ID	RA(2000)	Dec(2000)	B	V	$\log g$	$T_{\rm eff}$	A(Li)	A(O)	A(O)	A(Na)	A(Na)
	deg	deg	mag	mag	[cgs]	K	3D NLTE	1D NLTE	3D+NLTE	1D NLTE	3D+NLTE
00006129	6.15846	−71.96322	17.93	17.38	4.06	5850	1.61	8.36	8.42	5.78	5.81
00006340	5.96746	−71.96075	17.87	17.30	4.02	5820	...	8.09	8.13	5.69	5.71
00007619	6.33533	−71.94289	17.95	17.39	4.05	5790	1.24	8.24	8.30	5.68	5.70
00007969	6.11763	−71.93814	17.98	17.41	4.06	5810	1.82	8.50	8.57	5.37	5.38
00008359	6.24488	−71.93133	17.94	17.37	4.06	5840	1.99	8.40	8.46	5.55	5.56
00008881	6.16508	−71.92217	17.97	17.41	4.10	5920	2.09	8.30	8.35	5.66	5.68
00009191	6.21133	−71.91592	17.97	17.40	4.07	5830	1.92	8.34	8.41	5.46	5.49
00009243	6.27892	−71.91464	17.98	17.42	4.08	5860	1.96	8.39	8.46	5.36	5.35
00009434	6.24204	−71.91056	17.96	17.40	4.08	5870	1.86	8.15	8.19	5.54	5.54
00009540	6.11050	−71.90853	17.93	17.37	4.06	5840	1.93	8.28	8.34	5.58	5.59
00014912	5.80258	−71.96294	17.95	17.40	4.08	5860	1.56	8.20	8.26	5.63	5.65
00015086	5.76054	−71.96000	17.95	17.38	4.07	5880	2.03	8.39	8.46	5.43	5.44
00015174	5.82779	−71.95847	17.94	17.37	4.04	5790	1.66	8.28	8.34	5.56	5.57
00015346	5.58437	−71.95531	17.97	17.38	4.03	5730	1.70	8.50	8.57	5.45	5.45
00016131	5.77725	−71.94094	18.00	17.43	4.07	5820	1.71	8.41	8.48	5.44	5.46

Continued on next page

Table 14 – *Continued from previous page*

ID	RA(2000)	Dec(2000)	B	V	$\log g$	$T_{\rm eff}$	A(Li)	A(O)	A(O)	A(Na)	A(Na)
	deg	deg	mag	mag	[cgs]	K	3D NLTE	1D NLTE	3D+NLTE	1D NLTE	3D+NLTE
00016631	5.75729	−71.92917	18.01	17.44	4.08	5820	1.77	8.42	8.49	5.49	5.49
00017628	5.87896	−71.90236	18.00	17.43	4.11	5930	1.83	8.05	8.09	5.56	5.58
00017767	5.84779	−71.89828	17.95	17.39	4.06	5810	1.77	8.11	8.16	5.76	5.79
00031830	5.41504	−72.04769	17.93	17.36	4.05	5830	1.95	8.26	8.32	5.49	5.50
00036086	5.70875	−72.20400	17.92	17.35	4.05	5850	1.92	8.08	8.12	5.69	5.72
00036747	5.77333	−72.19608	18.01	17.46	4.09	5810	...	8.06	8.11	5.61	5.62
00038656	5.62004	−72.17497	17.96	17.40	4.08	5850	1.78	8.20	8.25	5.55	5.56
00040049	5.74092	−72.16181	17.95	17.40	4.07	5820	1.78	8.01	8.05	5.64	5.66
00040087	5.53888	−72.16119	17.92	17.35	4.03	5790	1.80	8.51	8.59	5.51	5.51
00040355	5.72492	−72.15906	17.93	17.36	4.06	5880	1.78	8.29	8.34	5.47	5.49
00043095	5.67775	−72.13700	17.97	17.41	4.05	5770	...	8.39	8.46	5.55	5.57
00043108	5.57883	−72.13678	17.89	17.33	4.03	5800	...	8.19	8.25	...	...
00044983	5.71950	−72.12375	17.90	17.33	4.04	5850	1.88	8.34	8.41	5.53	5.53
00045982	5.64500	−72.11706	17.90	17.33	4.00	5710	1.85	8.38	8.44	5.50	5.51
00046498	5.51050	−72.11339	17.93	17.35	4.04	5790	1.82	8.47	8.54	5.33	5.33
00049829	5.76571	−72.09175	17.88	17.29	3.99	5740	1.65	8.43	8.49	5.34	5.35

Continued on next page

Table 14 – *Continued from previous page*

ID	RA(2000)	Dec(2000)	B	V	$\log g$	$T_{\rm eff}$	A(Li)	A(O)	A(O)	A(Na)	A(Na)
	deg	deg	mag	mag	[cgs]	K	3D NLTE	1D NLTE	3D+NLTE	1D NLTE	3D+NLTE
00051341	5.55921	−72.08197	17.93	17.33	4.01	5730	...	8.43	8.50	5.44	5.43
00051740	5.53704	−72.07939	17.95	17.38	4.07	5860	1.73	8.29	8.35	5.48	5.51
00052108	5.50988	−72.07694	17.91	17.33	3.99	5690	1.84	8.50	8.58	5.42	5.42
00054596	5.61767	−72.06100	17.93	17.37	4.05	5830	1.85	8.35	8.41	5.46	5.47
00058492	5.68208	−72.03306	17.95	17.37	4.02	5730	1.64	8.31	8.37	5.46	5.46
00059579	5.66825	−72.02414	17.90	17.32	3.98	5660	1.87	8.34	8.40	5.37	5.37
00061639	5.69313	−72.00528	17.89	17.34	4.03	5780	1.91	8.35	8.41	5.21	5.20
00062314	5.56467	−71.99794	18.01	17.38	4.03	5740	...	8.42	8.49	5.43	5.44
00062737	5.58004	−71.99319	17.94	17.36	4.01	5690	...	8.07	8.12	5.64	5.66
00062773	5.87338	−71.99317	17.88	17.33	4.05	5850	1.90	8.12	8.16	5.73	5.75
00063201	5.60025	−71.98767	17.93	17.34	4.02	5760	1.73	8.41	8.48	5.36	5.36
00063954	5.77167	−71.97908	17.90	17.31	4.02	5800	1.54	8.06	8.10	5.65	5.67
00063973	5.70850	−71.97875	17.90	17.31	4.02	5780	1.86	8.29	8.35	5.40	5.40
00065981	6.05225	−72.22219	17.97	17.42	4.07	5810	...	8.21	8.27	5.69	5.71
00066603	6.05375	−72.21225	17.97	17.43	4.08	5850	1.77	8.03	8.06	5.68	5.70
00066813	6.34237	−72.20903	17.97	17.41	4.07	5820	1.61	8.27	8.32	5.44	5.45

Continued on next page

Table 14 – *Continued from previous page*

ID	RA(2000)	Dec(2000)	B	V	$\log g$	$T_{\rm eff}$	A(Li)	A(O)	A(O)	A(Na)	A(Na)
	deg	deg	mag	mag	[cgs]	K	3D NLTE	1D NLTE	3D+NLTE	1D NLTE	3D+NLTE
00066840	6.25950	−72.20878	18.04	17.50	4.10	5780	1.84	8.15	8.20	5.60	5.61
00067280	6.02708	−72.20253	17.98	17.43	4.07	5810	1.77	8.24	8.29	5.44	5.45
00069585	6.29904	−72.17517	17.95	17.39	4.08	5890	2.00	8.32	8.38	5.38	5.36
00070686	6.22921	−72.16494	17.94	17.37	4.05	5810	1.64	8.13	8.17	5.45	5.45
00070910	6.27663	−72.16297	17.95	17.40	4.06	5800	1.78	8.22	8.27	5.54	5.55
00071404	6.29454	−72.15886	17.98	17.41	4.06	5790	...	8.33	8.39	5.79	5.81
00072011	6.11733	−72.15458	18.02	17.45	4.05	5700	1.43	8.42	8.49	5.51	5.52
00096225	6.27933	−72.02936	17.90	17.34	4.04	5810	1.86	8.40	8.47	5.35	5.35
00097156	6.36075	−72.02406	17.93	17.36	4.03	5750	1.70	8.43	8.50	5.48	5.49
00099636	6.26008	−72.00881	17.94	17.40	4.06	5800	1.48	8.25	8.31	5.57	5.58
00100325	6.35675	−72.00369	17.94	17.38	4.05	5790	1.70	8.39	8.45	5.52	5.53
00102294	6.06792	−71.98808	17.89	17.32	4.01	5770	1.92	8.40	8.47	5.36	5.37
00102307	6.21471	−71.98781	17.94	17.39	4.07	5840	1.64	8.34	8.41	5.40	5.40
00103067	5.94763	−71.98056	17.88	17.31	3.98	5670	...	8.16	8.21	5.71	5.73
00103709	6.02521	−71.97353	17.89	17.31	4.02	5810	1.66	8.14	8.18	5.64	5.66
00104049	6.17200	−71.96964	17.89	17.32	4.02	5770	1.67	8.10	8.14	5.67	5.69

Continued on next page

Table 14 – *Continued from previous page*

ID	RA(2000)	Dec(2000)	B	V	$\log g$	$T_{\rm eff}$	A(Li)	A(O)	A(O)	A(Na)	A(Na)
	deg	deg	mag	mag	[cgs]	K	3D NLTE	1D NLTE	3D+NLTE	1D NLTE	3D+NLTE
00106794	6.47321	−72.18328	18.02	17.46	4.08	5790	1.74	8.34	8.40	5.53	5.52
00107260	6.45896	−72.17064	17.92	17.38	4.06	5830	1.73	8.34	8.41	5.33	5.33
00107528	6.57650	−72.16361	17.98	17.44	4.11	5920	2.02	8.38	8.45	5.55	5.55
00107618	6.59092	−72.16119	17.92	17.37	4.06	5830	2.03	8.36	8.42	5.57	5.58
00107866	6.56246	−72.15469	18.01	17.46	4.06	5730	1.78	8.51	8.58	5.14	5.12
00108171	6.40738	−72.14778	17.94	17.39	4.06	5810	...	7.92	7.95	5.84	5.86
00108389	6.58104	−72.14253	17.93	17.38	4.05	5810	1.61	8.22	8.27	5.51	5.53
00109441	6.53275	−72.11814	17.92	17.36	4.07	5880	1.70	8.22	8.27	5.42	5.41
00109777	6.50933	−72.11058	17.96	17.42	4.09	5870	2.00	8.36	8.42	5.54	5.55
00110197	6.60008	−72.10139	17.98	17.43	4.08	5820	1.78	8.60	8.68	...	...
00111136	6.48775	−72.08114	17.93	17.36	4.08	5910	1.98	8.36	8.42	5.40	5.42
00111231	6.52613	−72.07919	17.95	17.37	4.03	5730	1.66	8.41	8.47	5.28	5.28
00112473	6.59492	−72.05506	17.90	17.36	4.05	5840	1.67	8.34	8.40	5.45	5.44
00112684	6.46096	−72.05136	17.89	17.34	4.03	5780	1.55	8.30	8.36	5.39	5.39
00113090	6.47025	−72.04353	17.96	17.39	4.05	5790	1.64	8.32	8.39	5.47	5.48
00113841	6.55175	−72.02800	17.95	17.39	4.07	5850	1.96	8.52	8.60	5.44	5.44

Continued on next page

Table 14 – *Continued from previous page*

ID	RA(2000)	Dec(2000)	B	V	$\log g$	$T_{\rm eff}$	A(Li)	A(O)	A(O)	A(Na)	A(Na)
	deg	deg	mag	mag	[cgs]	K	3D NLTE	1D NLTE	3D+NLTE	1D NLTE	3D+NLTE
00113959	6.49396	−72.02594	17.93	17.38	4.10	5970	...	8.35	8.41	5.48	5.48
00115880	6.51471	−71.98331	17.94	17.37	4.06	5850	2.21	8.30	8.35	5.51	5.53
10000002	5.43304	−72.05411	17.96	17.41	4.09	5890	1.85	8.37	8.43	5.34	5.34
10000004	5.62229	−72.10428	17.95	17.40	4.10	5930	2.07	8.37	8.43	5.43	5.43
10000008	5.70025	−72.15828	18.06	17.50	4.13	5910	2.04	8.09	8.14	5.53	5.54
10000009	5.70075	−72.09483	18.04	17.48	4.09	5790	1.65	8.52	8.59	5.51	5.50
10000012	5.70475	−72.08533	17.86	17.30	4.03	5840	1.95	8.38	8.44	5.42	5.42
10000015	5.72129	−72.07636	17.91	17.34	4.02	5750	1.51	8.48	8.55	5.46	5.46
10000016	5.72533	−72.02817	17.88	17.28	3.98	5720	1.90	8.36	8.43	5.31	5.31
10000020	5.75263	−72.06483	18.00	17.46	4.10	5830	1.65	8.11	8.15	5.59	5.61
10000022	5.76167	−72.04869	17.85	17.28	3.99	5750	1.40	8.16	8.22	5.68	5.70
10000026	5.77117	−72.12517	17.97	17.41	4.06	5780	1.76	8.35	8.41	5.54	5.55
10000027	5.77721	−72.12919	18.00	17.44	4.08	5830	1.73	8.29	8.35	5.45	5.46
10000036	5.84604	−72.00550	17.90	17.34	4.00	5710	1.63	7.84	7.87	5.65	5.66
10000038	5.86846	−72.19789	17.84	17.25	4.00	5810	1.82	8.34	8.40	5.53	5.53
10000041	5.90950	−71.93806	17.93	17.38	4.08	5890	2.11	8.44	8.51	5.46	5.47

Continued on next page

Table 14 – *Continued from previous page*

ID	RA(2000)	Dec(2000)	B	V	$\log g$	$T_{\rm eff}$	A(Li)	A(O)	A(O)	A(Na)	A(Na)
	deg	deg	mag	mag	[cgs]	K	3D NLTE	1D NLTE	3D+NLTE	1D NLTE	3D+NLTE
10000043	5.94513	−72.17733	17.96	17.37	4.05	5880	1.73	8.18	8.23	5.85	5.88
10000048	5.99058	−71.98381	17.93	17.37	4.05	5830	1.76	8.14	8.18	5.64	5.65
10000049	6.00479	−72.18656	18.04	17.50	4.14	5940	2.01	8.32	8.38	5.54	5.55
10000053	6.04242	−72.20942	17.94	17.38	4.08	5880	...	8.08	8.12	5.68	5.70
10000057	6.08746	−71.93789	18.03	17.48	4.10	5850	1.76	8.21	8.26	5.70	5.72
10000062	6.12154	−71.97469	17.99	17.43	4.10	5890	...	7.73	7.75	5.76	5.79
10000068	6.15775	−71.95836	17.96	17.39	4.09	5920	...	8.03	8.07	5.74	5.78
10000072	6.19088	−71.97972	18.01	17.46	4.09	5830	...	8.12	8.16	5.60	5.61
10000073	6.21196	−72.00553	17.85	17.29	4.03	5860	1.33	8.27	8.32	5.31	5.32
10000075	6.24354	−71.96136	17.95	17.39	4.08	5880	1.88	8.43	8.49	5.46	5.46
10000079	6.27275	−72.12033	18.04	17.50	4.09	5750	1.68	8.52	8.59	5.31	5.31
10000086	6.30192	−72.05958	17.87	17.30	3.99	5710	1.57	8.11	8.16	5.35	5.34
10000088	6.31217	−72.03944	18.01	17.46	4.07	5770	1.50	7.89	7.92	5.78	5.80
10000090	6.34033	−71.96881	17.93	17.36	4.08	5920	2.02	8.31	8.37	5.43	5.44
10000094	6.42554	−72.07425	18.01	17.46	4.10	5870	1.63	8.34	8.40	5.35	5.35

Appendix B. The list of iron lines used to determine atmospheric parameters of the red giant stars in NGC 6752

Table 15. The list of the iron spectral lines lines used to determine atmospheric parameters of the red giant stars in NGC 6752.

Species	λ, nm	χ, eV	log gf	Species	λ, nm	χ, eV	log gf
Fe I	585.22187	4.548	-1.330	Fe I	627.02250	2.858	-2.464
Fe I	586.23530	4.549	-0.058	Fe I	630.15012	3.654	-0.718
Fe I	590.56720	4.652	-0.730	Fe I	632.26855	2.588	-2.426
Fe I	591.62474	2.453	-2.994	Fe I	633.53308	2.198	-2.177
Fe I	592.77891	4.652	-1.090	Fe I	633.68243	3.686	-0.856
Fe I	593.01799	4.652	-0.230	Fe I	634.41491	2.433	-2.923
Fe I	593.46549	3.928	-1.170	Fe I	635.50290	2.845	-2.350
Fe I	595.27184	3.984	-1.440	Fe I	638.07433	4.186	-1.376
Fe I	597.67750	3.943	-1.310	Fe I	639.36013	2.433	-1.432
Fe I	602.40580	4.548	-0.120	Fe I	640.00012	3.602	-0.290
Fe I	602.70509	4.076	-1.089	Fe I	641.16493	3.654	-0.595
Fe I	605.60047	4.733	-0.460	Fe I	641.99496	4.733	-0.240
Fe I	606.54822	2.608	-1.530	Fe I	642.13508	2.279	-2.027
Fe I	607.84910	4.795	-0.424	Fe I	643.08464	2.176	-2.006
Fe I	608.27106	2.223	-3.573	Fe I	647.56244	2.559	-2.942
Fe I	609.66653	3.984	-1.930	Fe I	648.18703	2.279	-2.984
Fe I	612.79066	4.143	-1.399	Fe I	649.49805	2.404	-1.273
Fe I	613.66153	2.453	-1.400	Fe I	649.64666	4.795	-0.570
Fe I	613.69947	2.198	-2.950	Fe I	651.83671	2.831	-2.460
Fe I	613.76917	2.588	-1.403	Fe I	659.38705	2.433	-2.422
Fe I	615.16181	2.176	-3.299	Fe I	660.91103	2.559	-2.692
Fe I	615.77284	4.076	-1.260	Fe I	663.37497	4.558	-0.799
Fe I	617.33356	2.223	-2.880	Fe I	667.79870	2.692	-1.418
Fe I	618.02042	2.727	-2.586	Fe I	670.35674	2.758	-3.160
Fe I	618.79904	3.943	-1.720	Fe I	675.01525	2.424	-2.621
Fe I	619.15584	2.433	-1.417	Fe I	680.68449	2.727	-3.210
Fe I	620.03129	2.608	-2.437	Fe II	599.13760	3.153	-3.540
Fe I	621.34303	2.223	-2.482	Fe II	608.41110	3.199	-3.780
Fe I	621.92810	2.198	-2.433	Fe II	614.92580	3.889	-2.720
Fe I	623.07230	2.559	-1.281	Fe II	624.75570	3.892	-2.310
Fe I	623.26412	3.654	-1.223	Fe II	636.94620	2.891	-4.160
Fe I	624.06462	2.223	-3.233	Fe II	641.69190	3.892	-2.650
Fe I	624.63188	3.602	-0.733	Fe II	643.26800	2.891	-3.520
Fe I	625.25554	2.404	-1.687	Fe II	645.63830	3.903	-2.100
Fe I	626.51340	2.176	-2.550	Fe II	651.60800	2.891	-3.320

Appendix C. Equivalent widths of lithium, sodium, and barium lines in the spectra of red giant stars in NGC 6752

Table 16. Measured equivalent widths of the lithium 670.7 nm line and the derived lithium abundances in individual red giants in NGC 6752.

Star	EW, (670.7nm) pm	$A(\mathrm{Li})_{\mathrm{1D\ LTE}}$, dex
NGC 6752–1	...	...
NGC 6752–2	...	...
NGC 6752–3	1.16	0.73
NGC 6752–4	...	...
NGC 6752–6	...	...
NGC 6752–7	1.90	0.97
NGC 6752–8	...	...
NGC 6752–9	1.66	0.82
NGC 6752–10	0.94	0.63
NGC 6752–11	2.07	1.00
NGC 6752–12	1.89	0.86
NGC 6752–15	2.36	1.05
NGC 6752–16	1.67	0.80
NGC 6752–19	2.31	1.06
NGC 6752–20	0.56	0.50
NGC 6752–21	2.10	1.00
NGC 6752–23	0.87	0.75
NGC 6752–24	1.55	0.95
NGC 6752–29	2.70	1.13
NGC 6752–30	...	...
mean		0.87
σ		0.18

Table 17. Measured equivalent widths of the sodium lines and the derived sodium abundances in individual red giants in NGC 6752.

Star	EW, (568.3nm)	EW, (568.9nm)	EW, (615.4nm)	EW, (616.1nm)	$A(\mathrm{Na})_{\mathrm{1D\ LTE}}$,	$A(\mathrm{Na})_{\mathrm{1D\ NLTE}}$,	$[\mathrm{Na/Fe}]_{\mathrm{1D\ LTE}}$,	$[\mathrm{Na/Fe}]_{\mathrm{1D\ NLTE}}$,
	pm	pm	pm	pm	dex	dex	dex	dex
NGC 6752–1	2.49	3.31	...	0.90	4.59	4.60	−0.21	−0.20
NGC 6752–2	5.77	7.99	1.21	2.58	5.22	5.22	0.43	0.43
NGC 6752–3	1.84	2.87	...	0.61	4.47	4.50	−0.27	−0.24
NGC 6752–4	5.34	7.60	1.43	2.51	5.21	5.23	0.47	0.47
NGC 6752–6	4.81	6.70	0.90	1.82	5.05	5.08	0.30	0.33
NGC 6752–7	1.29	2.39	...	...	4.34	4.45	−0.22	−0.11
NGC 6752–8	1.87	2.97	...	0.43	4.50	4.52	−0.23	−0.21
NGC 6752–9	2.06	3.17	...	0.39	4.45	4.55	−0.27	−0.17
NGC 6752–10	5.37	7.44	1.44	2.19	5.21	5.20	0.44	0.43
NGC 6752–11	3.19	5.14	0.79	1.46	4.91	4.90	0.14	0.13
NGC 6752–12	3.02	4.53	0.88	1.26	4.85	4.84	0.12	0.11
NGC 6752–15	2.03	3.14	...	0.68	4.55	4.60	−0.21	−0.16
NGC 6752–16	3.40	5.26	1.00	1.28	4.93	4.95	0.23	0.25
NGC 6752–19	2.42	3.81	...	0.81	4.70	4.76	0.01	−0.01
NGC 6752–20	5.34	7.69	1.45	2.05	5.27	4.76	0.50	−0.01
NGC 6752–21	2.58	4.58	...	0.90	4.76	4.83	0.05	0.12
NGC 6752–23	4.31	6.68	0.88	1.86	5.12	5.12	0.36	0.36
NGC 6752–24	1.17	2.55	...	...	4.40	4.55	−0.30	−0.15
NGC 6752–29	1.71	2.19	...	0.57	4.46	4.55	−0.19	−0.10
NGC 6752–30	2.07	3.71	...	0.81	4.68	4.70	−0.01	0.01
mean					4.78	4.77	0.06	0.05
σ					0.31	0.25	0.29	0.23

Table 18. Measured equivalent widths of the barium lines and the derived barium abundances in individual red giants in NGC 6752.

Star	EW, (585.4nm) pm	EW, (614.2nm) pm	EW, (649.7nm) pm	$A(\mathrm{Ba})_{\mathrm{1D\ LTE}}$, dex	$A(\mathrm{Ba})_{\mathrm{1D\ NLTE}}$, dex	$[\mathrm{Ba/Fe}]_{\mathrm{1D\ LTE}}$, dex	$[\mathrm{Ba/Fe}]_{\mathrm{1D\ NLTE}}$, dex
NGC 6752–1	8.21	12.54	12.87	0.92	0.63	0.28	−0.01
NGC 6752–2	8.43	12.45	12.08	0.91	0.65	0.28	0.02
NGC 6752–3	7.21	11.84	11.65	0.75	0.50	0.17	−0.08
NGC 6752–4	8.25	12.07	12.26	0.86	0.68	0.28	0.10
NGC 6752–6	8.23	11.96	12.80	0.87	0.60	0.28	0.01
NGC 6752–7	7.13	10.72	11.32	0.60	0.44	0.20	0.04
NGC 6752–8	7.01	11.29	11.37	0.84	0.72	0.27	0.15
NGC 6752–9	7.50	11.65	12.02	0.85	0.70	0.29	0.14
NGC 6752–10	7.57	11.58	12.16	0.87	0.67	0.26	0.06
NGC 6752–11	7.59	11.62	11.13	0.82	0.61	0.21	0.00
NGC 6752–12	7.01	11.44	11.34	0.76	0.61	0.19	0.04
NGC 6752–15	7.13	11.24	11.35	0.78	0.60	0.18	0.00
NGC 6752–16	7.36	11.51	11.59	0.80	0.58	0.26	0.04
NGC 6752–19	6.84	10.76	11.03	0.69	0.57	0.16	0.04
NGC 6752–20	6.77	11.16	10.81	0.87	0.75	0.26	0.14
NGC 6752–21	7.29	10.74	11.09	0.82	0.64	0.27	0.09
NGC 6752–23	7.17	10.71	11.21	0.88	0.72	0.28	0.12
NGC 6752–24	6.03	9.79	9.57	0.68	0.53	0.14	−0.01
NGC 6752–29	6.35	10.06	10.52	0.67	0.51	0.18	0.02
NGC 6752–30	6.39	9.92	10.57	0.82	0.66	0.29	0.13
mean				0.80	0.62	0.24	0.05
σ				0.09	0.08	0.05	0.06

Appendix D. The 3D–1D abundance corrections for the spectral lines of neutral and ionized elements in the atmospheres of red giant branch (RGB) and main sequence turn-off point (MSTO) stars

Table 19. 3D–1D abundance corrections for the spectral lines of neutral atoms in the atmosphere of red giants located close to the RGB tip. Atmospheric parameters of the 3D hydrodynamical model used to compute abundace corrections are: $T_{\rm eff} = 3600$ K, $\log g = 1.0$, [M/H] = 0.0.

element	χ	$\lambda = 400$ nm			$\lambda = 850$ nm			$\lambda = 1600$ nm		
	eV	$\Delta_{\rm 3D-1D}$	$\Delta_{\rm 3D-<3D>}$	$\Delta_{\rm <3D>-1D}$	$\Delta_{\rm 3D-1D}$	$\Delta_{\rm 3D-<3D>}$	$\Delta_{\rm <3D>-1D}$	$\Delta_{\rm 3D-1D}$	$\Delta_{\rm 3D-<3D>}$	$\Delta_{\rm <3D>-1D}$
	0	−0.003	0.011	−0.014	−0.005	0.006	−0.011	−0.030	−0.003	−0.027
	2	−0.060	−0.070	0.010	−0.040	−0.026	−0.014	−0.029	−0.002	−0.027
N I	4	−0.135	−0.194	0.059	−0.119	−0.131	0.012	−0.031	−0.015	−0.016
	6	−0.210	−0.312	0.102	−0.224	−0.288	0.064	−0.038	−0.032	−0.006
	8	−0.294	−0.430	0.136	−0.325	−0.448	0.123	−0.053	−0.054	0.001
	10	−0.398	−0.569	0.171	−0.412	−0.596	0.184	−0.078	−0.084	0.006
	0	−0.019	−0.008	−0.011	−0.010	0.002	−0.012	−0.031	−0.003	−0.028
	2	−0.090	−0.114	0.024	−0.062	−0.051	−0.011	−0.032	−0.007	−0.025
O I	4	−0.159	−0.231	0.072	−0.164	−0.190	0.026	−0.034	−0.020	−0.014
	6	−0.223	−0.333	0.110	−0.270	−0.356	0.086	−0.040	−0.034	−0.006
	8	−0.302	−0.442	0.140	−0.360	−0.504	0.144	−0.054	−0.055	0.001
	10	−0.409	−0.574	0.165	−0.439	−0.640	0.201	−0.079	−0.085	0.006
	0	0.011	0.029	−0.018	−0.001	0.010	−0.011	−0.027	−0.001	−0.026
Si I	2	−0.008	0.001	−0.009	−0.021	−0.004	−0.017	−0.019	0.011	−0.030
	4	−0.030	−0.049	0.019	−0.058	−0.054	−0.004	−0.006	0.014	−0.020
	6	−0.055	−0.107	0.052	−0.103	−0.129	0.026	0.005	0.012	−0.007
	0	0.053	0.027	0.026	0.027	−0.011	0.038	−0.030	−0.053	0.023
Ti I	2	0.055	0.045	0.010	0.033	0.014	0.019	−0.021	−0.023	0.002
	4	0.047	0.037	0.010	0.030	0.021	0.009	−0.010	−0.003	−0.007
	6	0.021	−0.008	0.029	0.012	−0.001	0.013	0.004	0.008	−0.004
	0	0.048	0.037	0.011	0.025	0.004	0.021	−0.025	−0.032	0.007
Cr I	2	0.047	0.047	0.000	0.028	0.022	0.006	−0.017	−0.008	−0.009
	4	0.037	0.032	0.005	0.020	0.019	0.001	−0.007	0.006	−0.013
	6	0.012	−0.019	0.031	−0.001	−0.011	0.010	0.006	0.012	−0.006
	0	0.020	0.037	−0.017	0.004	0.013	−0.009	−0.027	−0.004	−0.023
Fe I	2	0.012	0.027	−0.015	−0.007	0.011	−0.018	−0.019	0.011	−0.030
	4	0.000	−0.003	0.003	−0.028	−0.016	−0.012	−0.006	0.017	−0.023
	6	−0.017	−0.051	0.034	−0.054	−0.065	0.011	0.007	0.017	−0.010
	0	0.016	0.033	−0.017	0.001	0.011	−0.010	−0.027	−0.002	−0.025
Ni I	2	0.002	0.014	−0.012	−0.014	0.004	−0.018	−0.018	0.011	−0.029
	4	−0.015	−0.027	0.012	−0.042	−0.035	−0.007	−0.005	0.016	−0.021
	6	−0.038	−0.083	0.045	−0.079	−0.098	0.019	0.007	0.015	−0.008

Table 20. 3D–1D abundance corrections for the spectral lines of ionized atoms in the atmosphere of red giants located close to the RGB tip. Atmospheric parameters of the 3D hydrodynamical model used to compute abundace corrections are: $T_{\rm eff} = 3600$ K, $\log g = 1.0$, [M/H] = 0.0.

element	χ	$\lambda = 400$ nm			$\lambda = 850$ nm			$\lambda = 1600$ nm		
	eV	$\Delta_{\rm 3D-1D}$	$\Delta_{\rm 3D-<3D>}$	$\Delta_{\rm <3D>-1D}$	$\Delta_{\rm 3D-1D}$	$\Delta_{\rm 3D-<3D>}$	$\Delta_{\rm <3D>-1D}$	$\Delta_{\rm 3D-1D}$	$\Delta_{\rm 3D-<3D>}$	$\Delta_{\rm <3D>-1D}$
Si II	0	−0.148	−0.178	0.030	−0.202	−0.191	−0.011	−0.050	−0.017	−0.033
	2	−0.173	−0.238	0.065	−0.267	−0.308	0.041	−0.044	−0.023	−0.021
	4	−0.205	−0.299	0.094	−0.324	−0.413	0.089	−0.042	−0.029	−0.013
	6	−0.253	−0.374	0.121	−0.379	−0.514	0.135	−0.046	−0.040	−0.006
	8	−0.325	−0.472	0.147	−0.432	−0.617	0.185	−0.059	−0.060	0.001
	10	−0.426	−0.598	0.172	−0.494	−0.729	0.235	−0.084	−0.090	0.006
Ti II	0	−0.021	0.010	−0.031	−0.022	0.018	−0.040	−0.029	0.016	−0.045
	2	−0.070	−0.076	0.006	−0.061	−0.032	−0.029	−0.029	0.002	−0.031
	4	−0.135	−0.192	0.057	−0.132	−0.140	0.008	−0.030	−0.014	−0.016
	6	−0.204	−0.304	0.100	−0.222	−0.283	0.061	−0.036	−0.030	−0.006
	8	−0.285	−0.420	0.135	−0.314	−0.434	0.120	−0.049	−0.050	0.001
	10	−0.389	−0.554	0.165	−0.395	−0.572	0.177	−0.072	−0.079	0.007
Cr II	0	−0.036	−0.003	−0.033	−0.039	0.009	−0.048	−0.033	0.016	−0.049
	2	−0.081	−0.090	0.009	−0.080	−0.051	−0.029	−0.031	0.001	−0.032
	4	−0.139	−0.198	0.059	−0.149	−0.161	0.012	−0.031	−0.014	−0.017
	6	−0.202	−0.303	0.101	−0.232	−0.297	0.065	−0.036	−0.029	−0.007
	8	−0.279	−0.413	0.134	−0.318	−0.441	0.123	−0.048	−0.048	0.000
	10	−0.377	−0.542	0.165	−0.396	−0.574	0.178	−0.069	−0.076	0.007
Fe II	0	−0.103	−0.103	0.000	−0.134	−0.097	−0.037	−0.042	−0.002	−0.040
	2	−0.133	−0.174	0.041	−0.186	−0.192	0.006	−0.037	−0.012	−0.025
	4	−0.171	−0.249	0.078	−0.242	−0.293	0.051	−0.035	−0.021	−0.014
	6	−0.224	−0.334	0.110	−0.299	−0.398	0.099	−0.040	−0.033	−0.007
	8	−0.298	−0.438	0.140	−0.363	−0.511	0.148	−0.052	−0.053	0.001
	10	−0.400	−0.562	0.162	−0.428	−0.628	0.200	−0.075	−0.081	0.006
Ni II	0	−0.122	−0.130	0.008	−0.156	−0.123	−0.033	−0.047	−0.009	−0.038
	2	−0.150	−0.199	0.049	−0.216	−0.231	0.015	−0.040	−0.016	−0.024
	4	−0.183	−0.266	0.083	−0.272	−0.336	0.064	−0.038	−0.023	−0.015
	6	−0.231	−0.344	0.113	−0.331	−0.443	0.112	−0.041	−0.034	−0.007
	8	−0.299	−0.440	0.141	−0.383	−0.543	0.160	−0.053	−0.053	0.000
	10	−0.396	−0.564	0.168	−0.442	−0.652	0.210	−0.074	−0.080	0.006

Table 21. 3D–1D abundance corrections for the spectral lines of neutral atoms at $\lambda = 400$ nm in the atmosphere of red giants located close to the RGB base. Atmospheric parameters of the 3D hydrodynamical model used to compute abundace corrections are: $T_{\rm eff} = 5000$ K, $\log g = 2.5$

element	[M/H]	$\Delta_{\rm 3D-1D}$				$\Delta_{\rm 3D-<3D>}$				$\Delta_{\rm <3D>-1D}$			
		0 eV	2 eV	4 eV	6 eV	0 eV	2 eV	4 eV	6 eV	0 eV	2 eV	4 eV	6 eV
	−3	0.058	0.065	0.024	−0.049	0.003	0.008	−0.004	−0.042	0.055	0.057	0.028	−0.007
C I	−2	0.064	0.037	−0.009	−0.072	0.039	0.024	0.000	−0.043	0.025	0.013	−0.009	−0.029
	−1	0.002	−0.015	−0.033	−0.062	0.022	0.007	−0.016	−0.056	−0.020	−0.022	−0.017	−0.006
	0	−0.015	−0.023	−0.034	−0.052	0.005	−0.005	−0.026	−0.060	−0.020	−0.018	−0.008	0.008
	−3	−0.018	0.045	0.016	−0.061	−0.067	−0.010	−0.010	−0.052	0.049	0.055	0.026	−0.009
O I	−2	0.010	0.021	−0.015	−0.082	−0.014	0.008	−0.007	−0.055	0.024	0.013	−0.008	−0.027
	−1	−0.003	−0.012	−0.034	−0.073	−0.005	−0.002	−0.021	−0.069	0.002	−0.010	−0.013	−0.004
	0	−0.012	−0.022	−0.040	−0.071	−0.004	−0.010	−0.034	−0.080	−0.008	−0.012	−0.006	0.009
	−3	−0.315	−0.050	0.026	0.012	−0.338	−0.104	−0.022	−0.009	0.023	0.054	0.048	0.021
Si I	−2	−0.176	−0.020	0.027	0.014	−0.224	−0.075	−0.019	−0.011	0.048	0.055	0.046	0.025
	−1	0.003	0.031	0.034	0.021	−0.072	−0.020	0.000	−0.004	0.075	0.051	0.034	0.025
	0	0.020	0.028	0.029	0.022	−0.027	0.000	0.010	0.001	0.047	0.028	0.019	0.021
	−3	−0.459	−0.069	0.016	−0.009	−0.506	−0.126	−0.022	−0.020	0.047	0.057	0.038	0.011
Ti I	−2	−0.429	−0.087	0.006	−0.005	−0.492	−0.150	−0.039	−0.027	0.063	0.063	0.045	0.022
	−1	−0.073	0.002	0.025	0.014	−0.172	−0.069	−0.025	−0.023	0.099	0.071	0.050	0.037
	0	−0.022	0.010	0.025	0.020	−0.106	−0.048	−0.015	−0.015	0.084	0.058	0.040	0.035
	−3	−0.534	−0.124	0.010	0.012	−0.558	−0.179	−0.040	−0.012	0.024	0.055	0.050	0.024
Fe I	−2	−0.373	−0.097	0.005	0.013	−0.427	−0.160	−0.049	−0.019	0.054	0.063	0.054	0.032
	−1	−0.057	0.007	0.029	0.025	−0.161	−0.068	−0.023	−0.012	0.104	0.075	0.052	0.037
	0	0.001	0.022	0.031	0.028	−0.079	−0.032	−0.006	−0.002	0.080	0.054	0.037	0.030
	−3	−0.392	−0.071	0.020	0.009	−0.421	−0.128	−0.027	−0.011	0.029	0.057	0.047	0.020
Ni I	−2	−0.252	−0.048	0.018	0.012	−0.305	−0.108	−0.030	−0.015	0.053	0.060	0.048	0.027
	−1	−0.020	0.023	0.033	0.023	−0.109	−0.040	−0.009	−0.008	0.089	0.063	0.042	0.031
	0	0.015	0.028	0.031	0.025	−0.047	−0.012	0.005	0.000	0.062	0.040	0.026	0.025

Table 22. 3D–1D abundance corrections for the spectral lines of neutral atoms at $\lambda = 850$ nm in the atmosphere of red giants located close to the RGB base. Atmospheric parameters of the 3D hydrodynamical model used to compute abundace corrections are: $T_{\rm eff} = 5000$ K, $\log g = 2.5$

element	[M/H]	$\Delta_{\rm 3D-1D}$				$\Delta_{\rm 3D-<3D>}$				$\Delta_{\rm <3D>-1D}$			
		0 eV	2 eV	4 eV	6 eV	0 eV	2 eV	4 eV	6 eV	0 eV	2 eV	4 eV	6 eV
	−3	0.038	0.086	0.081	0.041	−0.001	0.006	−0.004	−0.030	0.039	0.080	0.085	0.071
C I	−2	0.081	0.073	0.044	0.003	0.059	0.044	0.019	−0.018	0.022	0.029	0.025	0.021
	−1	0.020	0.000	−0.016	−0.031	0.036	0.019	−0.004	−0.038	−0.016	−0.019	−0.012	0.007
	0	−0.010	−0.022	−0.033	−0.046	0.006	−0.008	−0.031	−0.063	−0.016	−0.014	−0.002	0.017
	−3	−0.082	0.048	0.069	0.036	−0.113	−0.027	−0.014	−0.035	0.031	0.075	0.083	0.071
O I	−2	−0.012	0.041	0.034	−0.001	−0.029	0.013	0.008	−0.023	0.017	0.028	0.026	0.022
	−1	0.003	0.002	−0.011	−0.030	−0.012	0.003	−0.008	−0.040	0.015	−0.001	−0.003	0.010
	0	−0.007	−0.017	−0.031	−0.049	−0.010	−0.012	−0.032	−0.068	0.003	−0.005	0.001	0.019
	−3	−0.484	−0.130	0.018	0.053	−0.469	−0.180	−0.061	−0.029	−0.015	0.050	0.079	0.082
Si I	−2	−0.290	−0.079	0.023	0.047	−0.315	−0.122	−0.039	−0.015	0.025	0.043	0.062	0.062
	−1	−0.016	0.028	0.042	0.040	−0.106	−0.035	−0.003	0.002	0.090	0.063	0.045	0.038
	0	0.020	0.031	0.034	0.030	−0.040	−0.007	0.008	0.006	0.060	0.038	0.026	0.024
	−3	−0.687	−0.170	0.015	0.045	−0.712	−0.241	−0.070	−0.036	0.025	0.071	0.085	0.081
Ti I	−2	−0.640	−0.190	−0.013	0.033	−0.687	−0.257	−0.085	−0.037	0.047	0.067	0.072	0.070
	−1	−0.131	−0.022	0.023	0.035	−0.245	−0.109	−0.044	−0.021	0.114	0.087	0.067	0.056
	0	−0.036	0.003	0.025	0.031	−0.138	−0.070	−0.029	−0.014	0.102	0.073	0.054	0.045
	−3	−0.753	−0.247	−0.018	0.046	−0.739	−0.298	−0.098	−0.038	−0.014	0.051	0.080	0.084
Fe I	−2	−0.544	−0.191	−0.024	0.034	−0.574	−0.248	−0.093	−0.035	0.030	0.057	0.069	0.069
	−1	−0.102	−0.012	0.028	0.040	−0.221	−0.102	−0.040	−0.014	0.119	0.090	0.068	0.054
	0	−0.005	0.020	0.034	0.036	−0.102	−0.047	−0.014	−0.002	0.097	0.067	0.048	0.038
	−3	−0.584	−0.167	0.008	0.050	−0.580	−0.222	−0.073	−0.032	−0.004	0.055	0.081	0.082
Ni I	−2	−0.392	−0.116	0.005	0.041	−0.423	−0.173	−0.061	−0.025	0.031	0.057	0.066	0.066
	−1	−0.050	0.013	0.038	0.041	−0.154	−0.063	−0.019	−0.005	0.104	0.076	0.057	0.046
	0	0.013	0.030	0.036	0.034	−0.064	−0.022	0.000	0.004	0.077	0.052	0.036	0.030

Table 23. 3D–1D abundance corrections for the spectral lines of neutral atoms at $\lambda = 1600$ nm in the atmosphere of red giants located close to the RGB base. Atmospheric parameters of the 3D hydrodynamical model used to compute abundace corrections are: $T_{\rm eff} = 5000$ K, $\log g = 2.5$

element	[M/H]	$\Delta_{\rm 3D-1D}$				$\Delta_{\rm 3D-<3D>}$				$\Delta_{\rm <3D>-1D}$			
		0 eV	2 eV	4 eV	6 eV	0 eV	2 eV	4 eV	6 eV	0 eV	2 eV	4 eV	6 eV
	−3	0.034	0.046	0.019	−0.019	−0.025	−0.014	−0.002	0.010	0.059	0.059	0.021	−0.029
C I	−2	0.049	0.023	−0.010	−0.038	0.019	0.012	0.010	0.014	0.029	0.012	−0.020	−0.052
	−1	−0.005	−0.020	−0.026	−0.024	0.013	0.010	0.011	0.013	−0.018	−0.030	−0.036	−0.037
	0	−0.015	−0.017	−0.014	−0.008	0.005	0.009	0.011	0.012	−0.020	−0.026	−0.025	−0.020
	−3	−0.051	0.023	0.013	−0.022	−0.104	−0.032	−0.005	0.008	0.053	0.056	0.019	−0.030
O I	−2	−0.011	0.007	−0.013	−0.040	−0.039	−0.006	0.006	0.011	0.027	0.013	−0.018	−0.051
	−1	−0.014	−0.018	−0.023	−0.024	−0.021	−0.002	0.007	0.010	0.007	−0.016	−0.029	−0.034
	0	−0.017	−0.016	−0.014	−0.009	−0.012	0.003	0.009	0.009	−0.005	−0.019	−0.023	−0.018
	−3	−0.375	−0.090	−0.003	0.002	−0.400	−0.145	−0.046	−0.004	0.025	0.055	0.043	0.006
Si I	−2	−0.217	−0.048	0.005	0.008	−0.268	−0.106	−0.037	−0.003	0.051	0.058	0.042	0.011
	−1	−0.022	0.008	0.015	0.014	−0.109	−0.049	−0.018	0.000	0.087	0.057	0.033	0.013
	0	−0.010	0.002	0.009	0.016	−0.069	−0.033	−0.010	0.005	0.058	0.035	0.019	0.011
	−3	−0.544	−0.118	−0.010	−0.005	−0.593	−0.174	−0.040	0.005	0.049	0.056	0.029	−0.010
Ti I	−2	−0.506	−0.131	−0.017	0.000	−0.572	−0.193	−0.055	−0.003	0.066	0.062	0.037	0.003
	−1	−0.116	−0.031	0.001	0.012	−0.226	−0.109	−0.046	−0.011	0.110	0.078	0.048	0.023
	0	−0.081	−0.040	−0.011	0.010	−0.178	−0.106	−0.053	−0.016	0.097	0.067	0.042	0.026
	−3	−0.615	−0.174	−0.023	0.000	−0.641	−0.231	−0.068	−0.009	0.026	0.057	0.045	0.009
Fe I	−2	−0.434	−0.135	−0.022	0.003	−0.491	−0.200	−0.072	−0.015	0.057	0.065	0.050	0.019
	−1	−0.093	−0.023	0.005	0.013	−0.209	−0.106	−0.049	−0.015	0.116	0.083	0.054	0.028
	0	−0.044	−0.018	−0.001	0.012	−0.137	−0.082	−0.041	−0.013	0.093	0.064	0.041	0.025
	−3	−0.461	−0.116	−0.010	0.000	−0.493	−0.173	−0.052	−0.004	0.032	0.057	0.042	0.004
Ni I	−2	−0.301	−0.080	−0.006	0.005	−0.358	−0.142	−0.050	−0.007	0.057	0.062	0.044	0.013
	−1	−0.050	−0.003	0.012	0.014	−0.151	−0.073	−0.031	−0.006	0.101	0.070	0.042	0.020
	0	−0.022	−0.004	0.007	0.016	−0.096	−0.052	−0.022	−0.001	0.074	0.048	0.029	0.017

Table 24. 3D–1D abundance corrections for the spectral lines of ionized atoms at $\lambda = 400$ nm in the atmosphere of red giants located close to the RGB base. Atmospheric parameters of the 3D hydrodynamical model used to compute abundace corrections are: $T_{\rm eff} = 5000$ K, $\log g = 2.5$

element	[M/H]	$\Delta_{\rm 3D-1D}$				$\Delta_{\rm 3D-<3D>}$				$\Delta_{\rm <3D>-1D}$			
		0 eV	2 eV	4 eV	6 eV	0 eV	2 eV	4 eV	6 eV	0 eV	2 eV	4 eV	6 eV
	−3	0.035	0.057	0.013	−0.070	−0.017	0.003	−0.010	−0.057	0.052	0.054	0.023	−0.013
Si II	−2	0.049	0.027	−0.022	−0.095	0.031	0.021	−0.006	−0.060	0.018	0.006	−0.016	−0.035
	−1	−0.007	−0.024	−0.046	−0.084	0.015	0.002	−0.025	−0.077	−0.022	−0.026	−0.021	−0.007
	0	−0.027	−0.035	−0.050	−0.080	−0.002	−0.014	−0.041	−0.088	−0.025	−0.021	−0.009	0.008
	−3	−0.049	0.038	0.020	−0.051	−0.095	−0.017	−0.009	−0.045	0.046	0.055	0.029	−0.006
Ti II	−2	−0.006	0.020	−0.010	−0.073	−0.030	0.004	−0.005	−0.047	0.024	0.016	−0.005	−0.026
	−1	−0.003	−0.010	−0.030	−0.067	−0.012	−0.002	−0.018	−0.061	0.009	−0.008	−0.012	−0.006
	0	−0.008	−0.018	−0.035	−0.065	−0.011	−0.009	−0.029	−0.072	0.003	−0.009	−0.006	0.007
	−3	−0.015	0.046	0.020	−0.054	−0.061	−0.009	−0.009	−0.047	0.046	0.055	0.029	−0.007
Fe II	−2	0.021	0.025	−0.011	−0.077	−0.001	0.011	−0.004	−0.049	0.022	0.014	−0.007	−0.028
	−1	0.003	−0.011	−0.033	−0.070	0.003	0.002	−0.018	−0.064	0.000	−0.013	−0.015	−0.006
	0	−0.010	−0.022	−0.038	−0.069	−0.001	−0.007	−0.031	−0.075	−0.009	−0.015	−0.007	0.006
	−3	−0.001	0.051	0.023	−0.051	−0.048	−0.005	−0.006	−0.044	0.047	0.056	0.029	−0.007
Ni II	−2	0.033	0.029	−0.010	−0.075	0.012	0.017	−0.001	−0.046	0.021	0.012	−0.009	−0.029
	−1	0.002	−0.014	−0.035	−0.070	0.010	0.004	−0.017	−0.062	−0.008	−0.018	−0.018	−0.008
	0	−0.016	−0.026	−0.041	−0.068	0.001	−0.008	−0.031	−0.073	−0.017	−0.018	−0.010	0.005
	−3	−0.064	0.037	0.029	−0.030	−0.106	−0.019	−0.004	−0.028	0.042	0.056	0.033	−0.002
Ba II	−2	−0.013	0.022	0.000	−0.051	−0.037	0.004	0.001	−0.029	0.024	0.018	−0.001	−0.022
	−1	−0.002	−0.005	−0.019	−0.043	−0.014	0.000	−0.009	−0.038	0.012	−0.005	−0.010	−0.005
	0	−0.006	−0.011	−0.021	−0.036	−0.012	−0.005	−0.015	−0.041	0.006	−0.006	−0.006	0.005
	−3	−0.051	0.039	0.024	−0.041	−0.096	−0.017	−0.007	−0.036	0.045	0.056	0.031	−0.005
Eu II	−2	−0.008	0.020	−0.006	−0.062	−0.032	0.004	−0.002	−0.037	0.024	0.016	−0.004	−0.025
	−1	−0.003	−0.009	−0.026	−0.055	−0.013	−0.002	−0.014	−0.049	0.010	−0.007	−0.012	−0.006
	0	−0.008	−0.016	−0.029	−0.049	−0.012	−0.008	−0.022	−0.055	0.004	−0.008	−0.007	0.006

Table 25. 3D–1D abundance corrections for the spectral lines of ionized atoms at $\lambda = 850$ nm in the atmosphere of red giants located close to the RGB base. Atmospheric parameters of the 3D hydrodynamical model used to compute abundace corrections are: $T_{\rm eff} = 5000$ K, $\log g = 2.5$

element	[M/H]	$\Delta_{\rm 3D-1D}$				$\Delta_{\rm 3D-<3D>}$				$\Delta_{\rm <3D>-1D}$			
		0 eV	2 eV	4 eV	6 eV	0 eV	2 eV	4 eV	6 eV	0 eV	2 eV	4 eV	6 eV
	−3	0.002	0.075	0.075	0.032	−0.034	−0.003	−0.007	−0.037	0.036	0.078	0.082	0.069
Si II	−2	0.059	0.062	0.035	−0.009	0.044	0.040	0.016	−0.024	0.015	0.022	0.019	0.015
	−1	0.010	−0.009	−0.025	−0.042	0.025	0.013	−0.010	−0.048	−0.015	−0.022	−0.015	0.006
	0	−0.026	−0.037	−0.047	−0.060	−0.005	−0.019	−0.043	−0.080	−0.021	−0.018	−0.004	0.020
	−3	−0.130	0.032	0.067	0.040	−0.153	−0.040	−0.016	−0.032	0.023	0.072	0.083	0.072
Ti II	−2	−0.039	0.032	0.034	0.004	−0.054	0.005	0.008	−0.019	0.015	0.027	0.026	0.023
	−1	0.000	0.003	−0.008	−0.026	−0.023	−0.001	−0.007	−0.035	0.023	0.004	−0.001	0.009
	0	−0.003	−0.011	−0.025	−0.044	−0.022	−0.014	−0.028	−0.061	0.019	0.003	0.003	0.017
	−3	−0.077	0.047	0.070	0.039	−0.102	−0.026	−0.013	−0.032	0.025	0.073	0.083	0.071
Fe II	−2	0.008	0.046	0.037	0.002	−0.007	0.020	0.012	−0.019	0.015	0.026	0.025	0.021
	−1	0.014	0.005	−0.010	−0.029	0.002	0.009	−0.005	−0.037	0.012	−0.004	−0.005	0.008
	0	−0.002	−0.016	−0.030	−0.048	−0.004	−0.009	−0.029	−0.065	0.002	−0.007	−0.001	0.017
	−3	−0.056	0.055	0.074	0.041	−0.081	−0.018	−0.009	−0.030	0.025	0.073	0.083	0.071
Ni II	−2	0.027	0.054	0.039	0.002	0.014	0.029	0.016	−0.016	0.013	0.025	0.023	0.018
	−1	0.016	0.002	−0.015	−0.032	0.014	0.013	−0.004	−0.036	0.002	−0.011	−0.011	0.004
	0	−0.010	−0.023	−0.037	−0.052	−0.001	−0.010	−0.032	−0.066	−0.009	−0.013	−0.005	0.014
	−3	−0.151	0.024	0.068	0.048	−0.169	−0.045	−0.015	−0.026	0.018	0.069	0.083	0.074
Ba II	−2	−0.051	0.030	0.038	0.012	−0.065	0.003	0.010	−0.011	0.014	0.027	0.028	0.023
	−1	−0.001	0.005	−0.004	−0.018	−0.027	−0.001	−0.003	−0.025	0.026	0.006	−0.001	0.007
	0	−0.002	−0.007	−0.018	−0.032	−0.024	−0.012	−0.021	−0.046	0.022	0.005	0.003	0.014
	−3	−0.132	0.031	0.068	0.043	−0.155	−0.041	−0.015	−0.029	0.023	0.072	0.083	0.072
Eu II	−2	−0.042	0.032	0.035	0.007	−0.057	0.004	0.008	−0.016	0.015	0.028	0.027	0.023
	−1	−0.001	0.003	−0.007	−0.023	−0.024	−0.001	−0.006	−0.031	0.023	0.004	−0.001	0.008
	0	−0.003	−0.010	−0.023	−0.039	−0.023	−0.013	−0.026	−0.055	0.020	0.003	0.003	0.016

Table 26. 3D–1D abundance corrections for the spectral lines of ionized atoms at $\lambda = 1600$ nm in the atmosphere of red giants located close to the RGB base. Atmospheric parameters of the 3D hydrodynamical model used to compute abundace corrections are: $T_{\rm eff} = 5000$ K, $\log g = 2.5$

element	[M/H]	$\Delta_{\rm 3D-1D}$				$\Delta_{\rm 3D-<3D>}$				$\Delta_{\rm <3D>-1D}$			
		0 eV	2 eV	4 eV	6 eV	0 eV	2 eV	4 eV	6 eV	0 eV	2 eV	4 eV	6 eV
	−3	0.009	0.039	0.015	−0.026	−0.046	−0.016	0.000	0.009	0.055	0.055	0.015	−0.035
Si II	−2	0.033	0.016	−0.016	−0.047	0.012	0.011	0.011	0.012	0.022	0.004	−0.028	−0.059
	−1	−0.013	−0.026	−0.030	−0.029	0.008	0.009	0.011	0.012	−0.021	−0.035	−0.041	−0.040
	0	−0.024	−0.023	−0.018	−0.012	0.004	0.009	0.012	0.010	−0.027	−0.032	−0.029	−0.021
	−3	−0.086	0.015	0.014	−0.019	−0.135	−0.042	−0.009	0.007	0.049	0.057	0.023	−0.026
Ti II	−2	−0.030	0.004	−0.011	−0.037	−0.057	−0.012	0.003	0.010	0.028	0.016	−0.014	−0.048
	−1	−0.016	−0.017	−0.022	−0.023	−0.030	−0.006	0.005	0.010	0.015	−0.010	−0.027	−0.033
	0	−0.018	−0.016	−0.013	−0.009	−0.027	−0.004	0.007	0.009	0.010	−0.011	−0.020	−0.019
	−3	−0.046	0.024	0.015	−0.020	−0.096	−0.033	−0.006	0.007	0.050	0.057	0.022	−0.027
Fe II	−2	0.002	0.011	−0.011	−0.039	−0.024	−0.002	0.006	0.011	0.026	0.013	−0.017	−0.050
	−1	−0.006	−0.016	−0.023	−0.024	−0.011	0.001	0.008	0.011	0.005	−0.018	−0.031	−0.036
	0	−0.013	−0.015	−0.014	−0.010	−0.007	0.004	0.010	0.010	−0.005	−0.020	−0.024	−0.020
	−3	−0.031	0.030	0.018	−0.019	−0.081	−0.028	−0.005	0.008	0.050	0.058	0.023	−0.027
Ni II	−2	0.015	0.015	−0.010	−0.039	−0.010	0.003	0.008	0.012	0.025	0.012	−0.018	−0.051
	−1	−0.006	−0.019	−0.025	−0.026	−0.002	0.005	0.010	0.012	−0.004	−0.024	−0.035	−0.038
	0	−0.016	−0.018	−0.016	−0.011	−0.001	0.007	0.011	0.011	−0.015	−0.025	−0.027	−0.022
	−3	−0.102	0.012	0.018	−0.011	−0.148	−0.047	−0.011	0.009	0.046	0.059	0.028	−0.020
Ba II	−2	−0.037	0.005	−0.007	−0.030	−0.066	−0.014	0.002	0.013	0.028	0.019	−0.009	−0.042
	−1	−0.016	−0.015	−0.019	−0.019	−0.034	−0.008	0.005	0.012	0.018	−0.007	−0.024	−0.031
	0	−0.018	−0.015	−0.011	−0.005	−0.031	−0.007	0.007	0.013	0.013	−0.008	−0.018	−0.017
	−3	−0.088	0.015	0.015	−0.016	−0.137	−0.043	−0.010	0.008	0.049	0.058	0.025	−0.024
Eu II	−2	−0.032	0.004	−0.010	−0.035	−0.060	−0.013	0.003	0.012	0.028	0.017	−0.013	−0.046
	−1	−0.016	−0.017	−0.022	−0.022	−0.032	−0.007	0.005	0.011	0.016	−0.010	−0.026	−0.033
	0	−0.019	−0.016	−0.013	−0.008	−0.029	−0.006	0.006	0.011	0.011	−0.010	−0.020	−0.019

Table 27. 3D–1D abundance corrections for the spectral lines of neutral atoms at $\lambda = 400$ nm in the atmospheres of MSTO stars. Atmospheric parameters of the 3D hydrodynamical model used to compute abundace corrections are: $T_{\rm eff} = 5900$ K, $\log g = 4.0$

element	[M/H]	$\Delta_{\rm 3D-1D}$				$\Delta_{\rm 3D-<3D>}$				$\Delta_{\rm <3D>-1D}$			
		0 eV	2 eV	4 eV	6 eV	0 eV	2 eV	4 eV	6 eV	0 eV	2 eV	4 eV	6 eV
C I	−2	0.068	0.091	0.064	0.014	0.024	0.013	0.007	−0.010	0.044	0.078	0.058	0.024
	−1	0.046	0.032	0.005	−0.029	0.030	0.025	0.015	−0.004	0.016	0.007	−0.010	−0.026
	0	0.005	−0.002	−0.011	−0.025	0.010	0.014	0.012	0.003	−0.005	−0.016	−0.024	−0.027
O I	−2	−0.026	0.067	0.055	0.004	−0.027	0.003	0.002	−0.018	0.000	0.063	0.053	0.022
	−1	0.015	0.021	−0.002	−0.040	0.001	0.015	0.009	−0.014	0.015	0.006	−0.011	−0.026
	0	0.001	−0.005	−0.018	−0.039	0.005	0.011	0.007	−0.010	−0.004	−0.016	−0.024	−0.028
Si I	−2	−0.444	−0.097	0.018	0.028	−0.190	−0.049	−0.006	0.002	−0.254	−0.049	0.024	0.026
	−1	−0.119	−0.009	0.029	0.024	−0.150	−0.051	−0.007	0.004	0.030	0.042	0.036	0.020
	0	−0.019	0.011	0.021	0.017	−0.069	−0.025	−0.001	0.007	0.050	0.036	0.022	0.009
Ti I	−2	−0.834	−0.197	−0.002	0.013	−0.626	−0.168	−0.024	−0.005	−0.208	−0.029	0.022	0.017
	−1	−0.243	−0.051	0.013	0.013	−0.286	−0.099	−0.024	−0.005	0.043	0.048	0.037	0.018
	0	−0.046	0.000	0.016	0.013	−0.102	−0.040	−0.008	0.003	0.056	0.040	0.024	0.010
Fe I	−2	−0.762	−0.227	−0.016	0.021	−0.429	−0.142	−0.029	−0.002	−0.333	−0.085	0.012	0.024
	−1	−0.249	−0.067	0.009	0.021	−0.281	−0.113	−0.033	−0.004	0.033	0.046	0.042	0.026
	0	−0.058	−0.006	0.015	0.017	−0.118	−0.052	−0.014	0.002	0.060	0.045	0.030	0.015

Table 28. 3D–1D abundance corrections for the spectral lines of neutral atoms at $\lambda = 850$ nm in the atmospheres of MSTO stars. Atmospheric parameters of the 3D hydrodynamical model used to compute abundace corrections are: $T_{\rm eff} = 5900$ K, $\log g = 4.0$

element	[M/H]	$\Delta_{\rm 3D-1D}$				$\Delta_{\rm 3D-<3D>}$				$\Delta_{\rm <3D>-1D}$			
		0 eV	2 eV	4 eV	6 eV	0 eV	2 eV	4 eV	6 eV	0 eV	2 eV	4 eV	6 eV
C I	−2	0.036	0.103	0.110	0.081	0.045	0.022	0.009	−0.007	−0.008	0.081	0.101	0.087
	−1	0.055	0.056	0.039	0.013	0.043	0.038	0.023	0.002	0.013	0.056	0.015	0.010
	0	0.017	0.013	0.005	−0.004	0.010	0.012	0.007	−0.006	0.006	0.000	−0.002	0.002
O I	−2	−0.117	0.058	0.096	0.074	−0.041	0.004	0.004	−0.010	−0.075	0.055	0.092	0.085
	−1	0.005	0.037	0.031	0.008	−0.004	0.019	0.016	−0.003	0.010	0.017	0.015	0.011
	0	0.010	0.010	0.003	−0.008	0.003	0.009	0.004	−0.011	0.008	0.001	−0.001	0.003
Si I	−2	−0.656	−0.211	−0.009	0.053	−0.240	−0.073	−0.016	−0.005	−0.416	−0.138	0.007	0.057
	−1	−0.198	−0.046	0.026	0.047	−0.206	−0.081	−0.021	−0.001	0.008	0.034	0.047	0.048
	0	−0.036	0.008	0.029	0.034	−0.094	−0.040	−0.012	−0.002	0.059	0.049	0.041	0.036
Ti I	−2	−1.126	−0.378	−0.043	0.041	−0.763	−0.276	−0.064	−0.017	−0.363	−0.102	0.021	0.058
	−1	−0.377	−0.118	−0.001	0.036	−0.403	−0.165	−0.056	−0.018	0.025	0.047	0.055	0.054
	0	−0.077	−0.011	0.021	0.031	−0.143	−0.067	−0.027	−0.011	0.066	0.056	0.048	0.042
Fe I	−2	−1.024	−0.401	−0.077	0.034	−0.510	−0.206	−0.059	−0.015	−0.514	−0.194	−0.018	0.049
	−1	−0.366	−0.134	−0.013	0.035	−0.374	−0.171	−0.064	−0.018	0.008	0.037	0.051	0.053
	0	−0.089	−0.020	0.017	0.031	−0.158	−0.078	−0.032	−0.011	0.069	0.058	0.049	0.042

Table 29. 3D–1D abundance corrections for the spectral lines of neutral atoms at $\lambda = 1600$ nm in the atmospheres of MSTO stars. Atmospheric parameters of the 3D hydrodynamical model used to compute abundace corrections are: $T_{\rm eff} = 5900$ K, $\log g = 4.0$

element	[M/H]	$\Delta_{\rm 3D-1D}$				$\Delta_{\rm 3D-<3D>}$				$\Delta_{\rm <3D>-1D}$			
		0 eV	2 eV	4 eV	6 eV	0 eV	2 eV	4 eV	6 eV	0 eV	2 eV	4 eV	6 eV
C I	−2	0.050	0.087	0.074	0.041	0.018	0.001	0.001	0.007	0.032	0.086	0.073	0.034
	−1	0.047	0.037	0.016	−0.004	0.022	0.017	0.013	0.013	0.025	0.019	0.002	−0.017
	0	0.006	0.001	−0.004	−0.004	−0.001	0.004	0.008	0.013	0.007	−0.004	−0.012	−0.017
O I	−2	−0.072	0.055	0.065	0.037	−0.049	−0.010	−0.001	0.006	−0.024	0.066	0.066	0.031
	−1	0.009	0.024	0.011	−0.006	0.024	0.005	0.010	0.011	0.019	0.019	0.002	−0.017
	0	0.001	−0.001	−0.005	−0.005	−0.007	0.002	0.008	0.012	0.008	−0.003	−0.012	−0.017
Si I	−2	−0.552	−0.153	−0.002	0.029	−0.230	−0.074	−0.024	−0.004	−0.322	−0.079	0.021	0.032
	−1	−0.155	−0.027	0.023	0.031	−0.188	−0.077	−0.025	−0.002	0.033	0.049	0.048	0.033
	0	−0.035	0.001	0.016	0.020	−0.096	−0.048	−0.020	−0.004	0.062	0.049	0.036	0.024
Ti I	−2	−0.983	−0.290	−0.029	0.017	−0.711	−0.237	−0.051	−0.005	−0.273	−0.053	0.022	0.022
	−1	−0.313	−0.085	0.003	0.023	−0.360	−0.142	−0.047	−0.008	0.047	0.057	0.050	0.031
	0	−0.072	−0.015	0.009	0.019	−0.140	−0.070	−0.031	−0.008	0.068	0.055	0.040	0.027
Fe I	−2	−0.902	−0.314	−0.051	0.017	−0.488	−0.189	−0.055	−0.012	−0.414	−0.126	0.004	0.029
	−1	−0.305	−0.098	−0.004	0.024	−0.340	−0.151	−0.058	-0.015	0.034	0.053	0.054	0.039
	0	−0.082	−0.022	0.006	0.018	−0.154	−0.081	−0.038	−0.013	0.072	0.059	0.045	0.031

Table 30. 3D–1D abundance corrections for the spectral lines of ionized atoms at $\lambda = 400$ nm in the atmospheres of MSTO stars. Atmospheric parameters of the 3D hydrodynamical model used to compute abundace corrections are: $T_{\rm eff} = 5900$ K, $\log g = 4.0$

element	[M/H]	$\Delta_{\rm 3D-1D}$				$\Delta_{\rm 3D-<3D>}$				$\Delta_{\rm <3D>-1D}$			
		0 eV	2 eV	4 eV	6 eV	0 eV	2 eV	4 eV	6 eV	0 eV	2 eV	4 eV	6 eV
Si II	−2	0.070	0.093	0.059	0.000	0.024	0.013	0.003	−0.021	0.046	0.080	0.056	0.021
	−1	0.043	0.025	−0.008	−0.049	0.033	0.025	0.010	−0.017	0.011	−0.001	−0.018	−0.032
	0	0.002	−0.009	−0.023	−0.045	0.016	0.015	0.007	−0.013	−0.014	−0.024	−0.030	−0.032
Ti II	−2	−0.066	0.058	0.058	0.011	−0.043	0.000	0.003	−0.014	−0.022	0.058	0.055	0.025
	−1	0.006	0.020	0.001	−0.034	−0.008	0.012	0.010	−0.010	0.014	0.008	−0.009	−0.025
	0	−0.003	−0.005	−0.016	−0.035	−0.001	0.009	0.007	−0.007	−0.001	−0.014	−0.023	−0.028
Fe II	−2	0.002	0.073	0.060	0.009	0.006	0.009	0.004	−0.015	−0.004	0.064	0.056	0.024
	−1	0.023	0.024	0.000	−0.037	0.010	0.018	0.011	−0.011	0.014	0.006	−0.011	−0.026
	0	0.001	−0.005	−0.017	−0.037	0.005	0.011	0.008	−0.008	−0.005	−0.016	−0.025	−0.029
Ba II	−2	−0.093	0.053	0.064	0.024	−0.055	−0.001	0.006	−0.004	−0.038	0.054	0.057	0.028
	−1	0.003	0.024	0.010	−0.019	−0.013	0.012	0.014	0.002	0.016	0.012	−0.004	−0.020
	0	−0.001	0.000	−0.007	−0.018	−0.003	0.009	0.012	0.006	0.002	−0.010	−0.019	−0.025
Eu II	−2	−0.074	0.058	0.062	0.020	−0.048	0.000	0.005	−0.007	−0.026	0.058	0.057	0.027
	−1	0.005	0.022	0.006	−0.025	−0.010	0.012	0.013	−0.002	0.015	0.010	−0.007	−0.023
	0	−0.002	−0.003	−0.011	−0.024	−0.002	0.009	0.011	0.003	0.000	−0.012	−0.022	−0.027

Table 31. 3D–1D abundance corrections for the spectral lines of ionized atoms at $\lambda = 850$ nm in the atmospheres of MSTO stars. Atmospheric parameters of the 3D hydrodynamical model used to compute abundace corrections are: $T_{\rm eff} = 5900$ K, $\log g = 4.0$.

element	[M/H]	$\Delta_{\rm 3D-1D}$				$\Delta_{\rm 3D-<3D>}$				$\Delta_{\rm <3D>-1D}$			
		0 eV	2 eV	4 eV	6 eV	0 eV	2 eV	4 eV	6 eV	0 eV	2 eV	4 eV	6 eV
Si II	−2	0.035	0.110	0.113	0.077	0.042	0.022	0.008	−0.011	−0.008	0.087	0.105	0.088
	−1	0.055	0.053	0.031	0.001	0.046	0.039	0.022	−0.004	0.009	0.013	0.009	0.005
	0	0.016	0.008	−0.002	−0.014	0.019	0.016	0.005	−0.013	−0.003	−0.008	−0.007	−0.001
Ti II	−2	−0.175	0.038	0.093	0.078	−0.065	−0.002	0.004	−0.008	−0.110	0.040	0.089	0.086
	−1	−0.011	0.032	0.032	0.011	−0.019	0.015	0.016	0.000	0.008	0.017	0.016	0.011
	0	0.004	0.008	0.003	−0.007	−0.007	0.005	0.004	−0.009	0.010	0.003	0.000	0.002
Fe II	−2	−0.071	0.068	0.101	0.079	0.013	0.015	0.007	−0.008	−0.084	0.053	0.093	0.087
	−1	0.018	0.042	0.034	0.010	0.010	0.026	0.019	0.000	0.008	0.016	0.014	0.010
	0	0.010	0.010	0.003	−0.008	0.003	0.010	0.005	−0.009	0.007	0.000	−0.002	0.001
Ba II	−2	−0.214	0.024	0.091	0.083	−0.081	−0.005	0.005	−0.003	−0.133	0.029	0.086	0.086
	−1	−0.019	0.032	0.036	0.019	−0.026	0.014	0.018	0.006	0.007	0.018	0.018	0.013
	0	0.004	0.011	0.008	0.002	−0.009	0.006	0.007	−0.001	0.013	0.005	0.001	0.003
Eu II	−2	−0.187	0.035	0.094	0.082	−0.072	−0.003	0.005	−0.005	−0.115	0.038	0.089	0.086
	−1	−0.014	0.032	0.034	0.015	−0.021	0.014	0.017	0.004	0.007	0.017	0.017	0.012
	0	0.003	0.009	0.005	−0.003	−0.008	0.005	0.005	−0.005	0.011	0.004	0.000	0.002

Table 32. 3D–1D abundance corrections for the spectral lines of ionized atoms at $\lambda = 1600$ nm in the atmospheres of MSTO stars. Atmospheric parameters of the 3D hydrodynamical model used to compute abundace corrections are: $T_{\rm eff} = 5900$ K, $\log g = 4.0$.

element	[M/H]	$\Delta_{\rm 3D-1D}$				$\Delta_{\rm 3D-<3D>}$				$\Delta_{\rm <3D>-1D}$			
		0 eV	2 eV	4 eV	6 eV	0 eV	2 eV	4 eV	6 eV	0 eV	2 eV	4 eV	6 eV
Si II	−2	0.050	0.092	0.075	0.038	0.017	0.003	0.003	0.007	0.033	0.089	0.072	0.031
	−1	0.045	0.032	0.009	−0.011	0.025	0.020	0.015	0.013	0.020	0.012	−0.006	−0.024
	0	0.005	−0.003	−0.008	−0.008	0.008	0.009	0.011	0.014	−0.003	−0.012	−0.019	−0.022
Ti II	−2	−0.121	0.042	0.065	0.041	−0.069	−0.015	−0.003	0.005	−0.053	0.057	0.067	0.035
	−1	−0.003	0.021	0.013	−0.004	−0.026	0.001	0.008	0.011	0.022	0.020	0.004	−0.015
	0	−0.004	−0.002	−0.005	−0.005	−0.015	−0.001	0.006	0.011	0.011	−0.001	−0.011	−0.016
Fe II	−2	−0.035	0.063	0.069	0.041	−0.005	−0.002	0.000	0.006	−0.030	0.066	0.069	0.035
	−1	0.019	0.028	0.013	−0.005	−0.003	0.009	0.011	0.012	0.022	0.018	0.002	−0.017
	0	0.001	−0.001	−0.005	−0.006	−0.006	0.003	0.008	0.012	0.008	−0.004	−0.013	−0.018
Ba II	−2	−0.154	0.033	0.066	0.046	−0.083	−0.018	−0.003	0.006	−0.072	0.051	0.069	0.040
	−1	−0.009	0.022	0.017	0.002	−0.032	0.000	0.008	0.012	0.023	0.023	0.009	−0.010
	0	−0.003	0.000	−0.002	−0.002	−0.017	−0.003	0.005	0.012	0.014	0.002	−0.007	−0.014
Eu II	−2	−0.132	0.040	0.066	0.044	−0.075	−0.017	−0.003	0.006	−0.057	0.057	0.069	0.038
	−1	−0.006	0.021	0.014	−0.002	−0.028	0.000	0.008	0.012	0.023	0.021	0.006	−0.013
	0	−0.004	−0.002	−0.004	−0.004	−0.016	−0.002	0.005	0.012	0.012	0.000	−0.010	−0.016